Bptf is essential for murine neocortical development

Gerardo Zapata

Thesis submitted to the Faculty of Graduate and Postdoctoral Studies
in partial fulfillment of the requirements for the
Master's degree in Biochemistry with specialization in Bioinformatics

Department of Biochemistry, Microbiology and Immunology
Faculty of Medicine
University of Ottawa

Abstract

Chromatin remodeling complexes modulate DNA accessibility permitting neuronal progenitor cells to proliferate and differentiate to form the mammalian neocortex. In the case of BPTF (Bromodomain PHD transcription Factor), the major subunit of a chromatin remodelling complex called NURF (Nucleosome Remodelling Factor), mutations leading to its haploinsufficiency have been linked to cause a recently annotated human neurodevelopmental disorder called NEDDFL (Neurodevelopmental disorder with dysmorphic facies and distal limb anomalies). Patients with this syndrome are mainly characterized with microcephaly and intellectual disability. We conditionally knockout (cKO) the *Bptf* gene during neocortical neurogenesis to analyze its role during embryonic and postnatal brain development. The *Bptf* cKO animals reveal significant forebrain hypoplasia. During cortical neurogenesis, the *Bptf* cKO mice show a reduction in intermediate neuronal progenitor (INP) cells, an increase in apoptosis as well as a prolonged cell cycle within proliferating progenitors. Similarly, the postmitotic pyramidal neurons of the *Bptf* cKO mice contained lower levels of Ctip2 and Foxp1. Lastly, our RNA-seq analysis delineated gene pathways deregulated by *Bptf* removal, which are involved in neurogenesis and neuronal differentiation. Our results indicate that *Bptf* is critical for murine telencephalon neurogenesis. The hypoplasia demonstrated in the mouse model can resemble the microcephaly displayed by the human NEDDFL patients, highlighting the relevance of chromatin remodelling complexes during intricate neural developmental processes.

Acknowledgements

Tonia, your undying support, love and encouragement strengthened my desire to strive for greater things in life and pushed me further to seek a higher level of education. The completion of this thesis is a result of our accumulated efforts.

Mamá, Papá y Ana María, todo lo que soy y todo lo que eh logrado es gracias a ustedes, esta tesis es tanto suya como mía. Sin su guía, apoyo y consejos, yo no hubiera sido capaz de haber empezado esta segunda etapa de mi vida.

Juan, siempre has sido un gran modelo a seguir. Asimilar tu buen humor me ha ayudado a disfrutar lo que eh logrado y, aunque de lejos, tu ejemplo me dio las fuerzas necesarias para seguir luchando en tiempos difíciles y poder finalizar mi maestría.

Dave, thank you for providing me with the opportunity to become part of the lab. I have learned a great deal, and in your lab, I have begun the next and exciting chapter of my life.

Raies and Keqin, I learned almost all the techniques and experiments used in this thesis from both of you. Thank you so much for your patience, understanding and great company.

Table of Contents

List of Abbreviations

ACF = ATP-utilising Chromatin assembly and remodeling Factor
ACF1 = ATP-utilizing Chromatin assembly and remodeling Factor 1
ACVS = Animal Care and Veterinary Services
Ascl1 = Achaete-Scute family BHLH transcription factor 1
ARID1A/B = AT-Rich Interaction Domain 1A/B
ASD = Autism Spectrum Disorder
ATRX = Alpha-Thalassemia/mental Retardation Syndrome, X-Linked
BAF = Brg1/Brm Associated Factor
Baz2b = Bromodomain Adjacent to Zinc finger domain 2B
bp = base pairs
BRF = BAZ2B containing Remodelling Factor
BPTF = Bromodomain PHD transcription factor
Brg1 = Brahma-Related Gene 1
Brm = Brahma
Cecr2 = Cat Eye syndrome Chromosome Region, candidate 2
CHD = Chromodomain Helicase DNA-binding
CNS = Central Nervous System
CR = Cajal-Retzius
CSS = Coffin-Siris Syndrome
Cux1/2 = Cut-like homeobox 1/2
CERF = CECR2-containing Remodeling Factor
CHARGE = Coloboma, Heart malformation, choanal Atresia, Retardation of Growth and/or development, genital anomalies, and Ear anomalies
Chd1 = Chromodomain Helicase DNA binding protein 1
ChIP = Chromatin Immunoprecipitation
CHRAC = Chromatin Accessibility Complex
cKO = conditional Knock-Out
Co-Ips = Co-Immunoprecipitations
CP = Cortical Plate
Ctcf = CCCTC-binding Factor
Ctip2 = COUP-TF-Interacting Protein 2
Daxx = Death domain Associated protein
DEGs = Differentially Expressed Genes
DIG-dUTPs = Digoxigenin -11-deoxyuridine triphosphate
DO = Disease Ontology
E8.5 (any number) = Embryonic day 8.5
EcKO = Emx1 Bptf conditional Knock-Out
EdU = 5-Ethynyl-2´-deoxyUridine
Emx2 = Empty spiracles homeobox 2
FALZ = Fetal Alz-50 clone1
Fezf2 = Fez family zinc Finger 2
Foxg1 = Forkhead box G1
Foxp1 = Forkhead box P1
GO = Gene Ontology
H3K4me3 (any number) = Histone 3 lysine 4 tri-methylation
HATs = Histone acetylases
HDAC = Histone Deacetylase
Het = Heterozygous
IDD = Intellectual Disability Disorders
IF = Immunofluorescence

INO80 = ATP-dependent human Ino80
IPCs = Intermediate neuronal Progenitor cells
IRES = Internal Ribosomal Entry Site
ISWI = Imitation SWI
IZ = Intermediate Zone
L2FC = Log 2 Fold Change
Lhx2 = LIM homeobox 2
LoF = Loss of Function
Myc = MYC Proto-Oncogene, BHLH Transcription Factor
MZ = Marginal Zone
NAP1 = Nucleosome Assembly Protein 1
NcKO = Nestin Bptf conditional Knock-Out
NDDs = Neurodevelopmental Disorders
NEDDFL = Neurodevelopmental Delay with Dysmorphic Facies and distal Limb anomalies
NeuroD1 (any number) = Neuronal Differentiation 1
Neurog1/2 = Neurogenin 1/2
NoRC = Nucleolar Remodeling Complex
NuRD = Nucleosome Remodelling and Deacetylase
NURF = nucleosome remodelling Factor
OMAFRA = Ontario Ministry of Agriculture and Rural Affairs
P2 (any number) = Post-natal day 2
Pax6 = Paired box 6
PBS = Phosphate Buffered Saline
PFA = Paraformaldehyde
pH3 = phosphor Histone 3
PTM = Post-Translationally Modified
RbAP46/48 = Retinoblastoma-Binding Protein P46
RGCs = Radial Glial Cells
RNAi = RNA interference
RSF = Remodeling and Spacing Factor
Satb2 = Special AT-rich sequence Binding protein 2
SEM = Standard Error of the Mean
SMARCB1 = SWI/SNF Related, Matrix associated, Actin dependent Regulator of Chromatin, subfamily B, member 1
SMARCA1 (any number) = SWI/SNF related, Matrix associated, Actin dependent Regulator of Chromatin, subfamily A, member 1
SNF2L/H = Sucrose Non-Fermenting 2-Like Protein 1 / homolog
SNP = Single Nucleotide Polymorphisms
SP = Sub-Plate
SRCAP = SNF2-Related CBP Activator Protein
SWI/SNF = Switch/sucrose Non-Fermentable
Tbr1/2 = T-box Brain Protein ½
TIP5 = Transcription termination factor I-Interacting Protein 5
TF = Transcription Factor
TSS = Transcriptional Start Site
UTR = Untranslated Region
VZ = Ventricular Zone
WES = Whole Exome Sequencing
WICH = WSTF-ISWI Chromatin remodeling factor
WSTF = Williams Syndrome Transcription Factor
WT = Wild-Type

List of Figures

List of Tables

1. Introduction

1.1. Cortical Neurogenesis

1.1.1. Progenitor pool of the neocortex

Human learning, behaviour, communication, reasoning, awareness and cognitive abilities emerge from the arrival of the neocortex (1). Therefore, it is critical to use a mouse model to research and understand the processes that lead to the development of such a vital region of the mature brain. Neurulation is the formation of the embryonic neural tube, the precursor of the adult brain and spinal cord (2). In the mouse, the anterior (or front end) of the neural tube can be naturally divided into three main regions: the prosencephalon (forming the precursor of the forebrain), the mesencephalon (midbrain) and the rhombencephalon (hindbrain and subsequent cerebellum) (3). Furthermore, by ~embryonic day 8.5 (E8.5) the prosencephalon proliferates quickly to form two separate regions: the telencephalon at the posterior end and, the diencephalon which will develop the future thalamus underneath the cortex (1). The telencephalon then divides into two separate regions: the pallial which forms the neocortex and, the sub-pallial which develops into the amygdala and basal ganglia (1).

The murine neocortex formation begins around E8.5 - 9.5, with neuroepithelial cells expressing critical transcription factors specific to the forebrain, in order to begin proliferation and to form the ventricular zone (VZ) (4). Within the dorsoventral prosencephalon, key transcription factors (TF) such as Emx2, Pax6 and Lhx2 begin their expression to specify the neocortical identity (1). At ~E10.5 (figure 1), the neuroepithelial cells of the VZ differentiate to Radial Glial cells (RGCs) to initiate the neurogenesis process (1). At this point, the RGCs begin to express the TF Pax6, a marker for RGCs to initiated proliferation (1). When RGCs divide

symmetrically (vertical plane of division along with the ventricle) they proliferate and produce two daughter RGCs. On the other hand, when the RGCs divide asymmetrically (horizontal/oblique plane of division), they generate one daughter RGC and, either a committed neuron or an intermediate neuronal progenitor cell (IPCs) (1). IPCs are a secondary set of progenitor cells which have lost some of the proliferative potential but, they still proliferate to produce committed neuronal subtypes. Once IPCs have begun their proliferations stage they are characterized by the expression of their specific differentiation TF, Tbr2 (1). Both, the RGCs and the IPCs are consequently known as the progenitor pool of the neocortex as they are in charge of proliferating and differentiating into the diverse cortical neurons. Once the progenitor pool has acquired its RGC and IPC identity, pro-neural genes are then expressed to induce their differentiation (5). Neurog1, Neurog2 and Ascl1 aid in the activation and control of their differentiation (5). Increased Neurog1/2 favours the differentiation of RGC and IPCs into an excitatory glutamatergic neuronal pathway, to form the layers of the cortex. Neuronal differentiation genes, NeuroD1, NeuroD2, NeuroD4 and NeuroD6, are direct downstream targets of Neurog1/2 which also serve to induce several downstream regulators of neuronal migration and differentiation (6).

As differentiation continues, the early cortex begins to take shape. By ~E12, the progenitor pool has finished creating the first layer of cells, the Cajal-Retzius (CR) cells which form the marginal zone (MZ) of early developmental cortex and layer I of the mature cortex. Foxg1, a TF expressed in RGCs and IPCs, signals the end of CR production and initiates the switch to the formation of early born layer VI neurons (1). Previous Foxg1 mouse knockout experiments have demonstrated the formation of a significantly hypoplastic forebrain, from which the progenitor pool failed to expand and create the cortical plate (CP) neurons (7). At this

timepoint (~E12) the progenitor pool has also created the sub-plate (SP), formed by neurons which disappear in adult mice (4). The SP serves as a dividing line between the CP and the subventricular zone (SVZ). The SVZ is now mostly compromised of IPCs and the VZ mostly formed by RGCs (4). Further in time, the SVZ will become the Intermediate Zone (IZ) (1). At ~ E12 the progenitor pool begins to differentiate and create the neurons that will move into the CP (4). In hand with Foxg1, Fezf2, has also been observed to be expressed in RGC during early-born neuronal formulation (8). Fezf2 serves as a contributing transcription factor to maintain progenitor-like features allowing for the RGCs and IPCs to form early born neurons, Layers V-VI (8). Neurogenesis peaks in expansion at ~E15.5, then slows down until P0 and maintains a very low but continuous increase until postnatal-day 17 (P17) (4).

1.1.2. Neurons of the cortical plate and their transcription factors

Neurogenesis is an extremely complex process in which the progenitor pool of the embryonic neocortex proliferates and differentiates to form the neurons that will form the CP. The murine cortical plate is then formed by different neurons organized in a specific manner: layers II/III, layer IV, layer V and layer VI. It is important to note however that the cortex forms in an inside out manner, meaning that the neurons will form bottom up. Early born neurons (comprised of layers V and VI) will be located at the bottom of the CP and the late born neurons (Layers II-IV) will migrate upwards past layers V and VI to the top of the cortical plate (5), in a sequential manner (Figure 1). First, layer VI is known as the multiform layer as it contains large and small pyramidal neurons as well as multiform neurons (9). These neurons send their projections to the thalamus and are mostly characterized by the expression of Tbr1 (1). It is important to consider however, that the expression of Fezf2 and Ctip2 is also observed in this layer, yet their expression is not as intense, nor do they mark all of the cells in this layer (1).

Neurons located in layer V are also known as the large pyramidal neurons, which can extend their axons all the way to the spinal cord and brain stem (8). These large neurons are mainly characterized by the expression of Ctip2 and Fezf2, which are both critical TFs for their formation (8). Ctip2 and Fezf2 murine KO experiments have demonstrated that without these proteins, the layer V neurons fail to extend their long axons and have deferred expression of other critical TF, respectively (8). Neurons located in layer IV are also widely known as thalamocortical neurons since they extend their axons to the thalamus region of the brain (10). Foxp1 is another critical neuronal differentiation transcription factor which can be used to identify layer IV neurons, yet it is also observed trickling down into layer V (11). Last, neurons in layers II/III are known as callosal projection neurons which are known to project their axons and form the corpus callosum, ensuring communication between both lobes of the cortex (12). The expression of key transcription factors Cux1 (cut-like homeobox 1) and Cux2 is specific to these layers (13). Special AT-rich sequence binding protein 2 (Satb2) is also a transcription factor used to identify these cells (1). Although, its expression is not as specific, and it can also be observed in layers IV and V. Furthermore, the aforementioned TFs are a way of distinguishing the different layers of the murine neocortex in a broad manner. It is also important to keep in mind that these TFs are also in a regulatory circuit to repress each others activity. In this way, Ctip2 will repress the activity of Tbr1 allowing the switch in production from layer VI to layer V. Consequently, Satb2 will then repress the activity of Ctip2, in order to lead the differentiation from layer V to layers II/III. All together, allowing for the sequential differentiation of neurons as they migrate upwards through the CP (1).

The complex interplay between transcription factors to determine the differentiation and proliferation of the progenitor pool requires careful timing and specific epigenetic regulation.

Similarly, the differentiation of neurons into their target cell fate continues as they migrate through the cortical plate to their final destination and, this also requires epigenetic control of temporal transcription factor expression. Chromatin remodeling then allows for the dynamic modulation of nucleosomes to expose the DNA, allow it to interact with diverse TFs and permit them to regulate cell-fate pathways in a precisely timed manner. Consequently, remodelers are essential for both the proliferating progenitor pool and the differentiating migrating neurons.

1.1.3. Gliogenesis and Microglia Origins

During neuron formation, at ~E17.5 a lineage of RGCs gradually decrease expression of Neurog1/2 and increase the expression of Ascl1 (5). This switch in expression marks the beginning of gliogenesis, in which the progenitor daughter cells now begin to differentiate into astrocytes and later on, postnatally, will differentiate into oligodendrocytes (14). The primary and broad function of astrocytes is to provide physical and chemical support to neurons, while the oligodendrocytes function mainly to provide the myelination sheath on the neuronal axons (1). Both of these cell types are also known as macroglia and are not to be confused with microglia which do not arise from neural progenitors. Microglia in the brain serve to maintain neuronal homeostasis, provide nourishment for neurons and promote synaptic development (15). In mice, the primitive embryonic yolk sac (not the neural tube) produces a separate set of progenitors which migrate to the brain by E9 (15). These progenitors are then responsible for the development of microglia observed in the adult brain (15). Furthermore, microglia can exist in the brain in three main states: ramified, intermediate and amoeboid (16). The ramified state is visible in the healthy mouse brain, it is considered to be active, and monitoring the brain environment. The amoeboid state is seen during brain inflammation, where the microglia takes on

a macrophage role to engage in phagocytosis of undesired cellular debris (16). This change of microglia state is in response to its environment and in occurrence of damage to the brain (16).

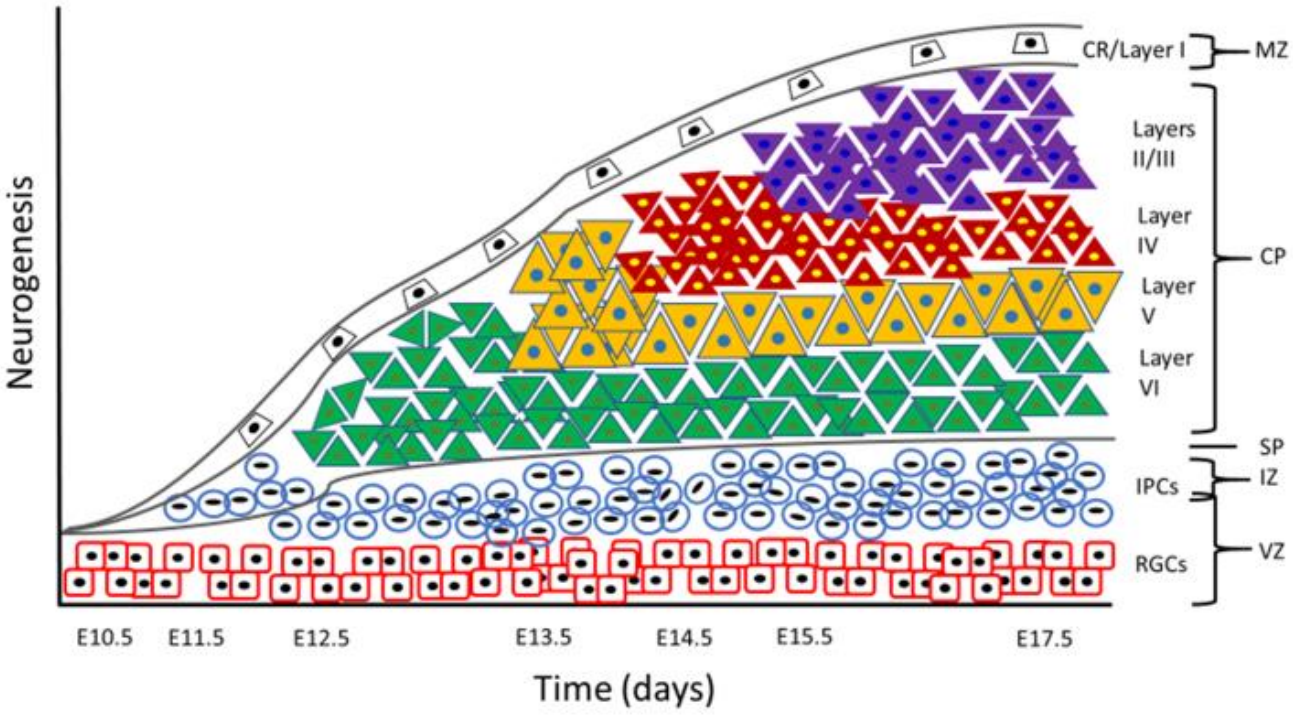

Figure 1 **Basic depiction of Neurogenesis. Depiction adapted from Adnani et al (1).**
Initially, as time goes on the RGCs produce the IPCs and by E12 they both have produced the CR cells which will form the MZ. Formation of neurons in a bottom up order, beginning at around E12.5. Red squares = RGCs, blue circles = IPCs, triangles = diverse neurons in the CP, white trapezoid = CR cells. Triangles: green = layer VI mostly expressing Tbr1, yellow = layer V expressing Ctip2, red = layer IV foxp1 positive neurons and purple = layer II/III are mainly Satb2 cells.

1.2. Neurodevelopmental disorders and chromatin remodelers

Central nervous system (CNS) development and neurogenesis are incredibly complex processes which involve a myriad of signaling proteins and TFs needed to be expressed at precise timepoints in different tissue types during development. The human cortex develops similar to the mouse, although symmetric and asymmetric division expand the cortex of the progenitor and

neuronal cells at a rate 15 times more prolonged in humans than in rodents (17). These massive proliferative events render the brain vulnerable to an increase in mistakes, allowing for diseases to occur (17). Either inherited or novel mutations arising during these processes can lead to the establishment of neurodevelopmental disorders (NDDs). Neurodevelopmental disorders cover the autism spectrum disorder (ASD) as well as a wide range of brain and intellectual disability disorders (IDD) which occur directly due to abnormal CNS development (18). Due to their nature, IDD are very diverse in their phenotype, ranging from learning complications to extreme diminished cognitive abilities (19). IDD have been attributed to be caused by ~750 mutated genes, out of which nearly 8% of them are chromatin-function and epigenetic machinery related (19, 20). All together, IDD are present in around 1-2% of the human population making them a serious social and health-care issue, as some cases have restrained levels of treatment as well as require life-long care (17, 18). Clinical trials for syndromes such as fragile X syndrome, Angelman and Rett syndromes, are now being considered as tangible options to try and revert some of the phenotypes displayed (18). Therefore, there is a need to understand the regulatory processes of chromatin remodelers during nervous system development, as well as to comprehend how when mutated they can lead to NDDs, in order to create novel therapeutics and improve the life quality of such patients.

1.3. Chromatin and nucleosome organization

The human genome is immensely complex. The entire human genome within a single cell is ~ 2.05 meters long and it weighs about 6.5 picograms (21). This means that each cell in our body must manage to fit, manipulate, and replicate the entirety of the genome within the miniscule ~10 μm diameter of the nucleus. Therefore, the organization and dynamic structuring of the genome are critical characteristics that must be fully understood. Chromatin remodelers are

those complexes in charge of modifying chromatin organization in order to expose or retract the DNA, allocate different types of histone proteins, and modify nucleosome spacing to expose critical regions of the genome (22). The focus of this thesis is to examine the role of Bptf, a subunit of the NURF chromatin remodeling complex, during the formation of the murine cortex.

Chromatin is the name given to the highly organized and grouped formation of multiple nucleosomes (23). A nucleosome is also known as the active unit of chromatin. It is a histone octamer complex compromised of two copies each H2A, H2B, H3 and H4 histone proteins and 146 bp (base pairs) of the DNA strand looped twice around each octamer to form the complete nucleosome (24). About 50 bp of linker DNA reside between each nucleosome, "linking" them together. Furthermore, the histone protein H1 can bind to the linker DNA and interact with the nucleosome, forming the chromatosome (25). The most accessible DNA is the 10 nM fiber that can be observed in a continuous formation of separate nucleosomes forming the beads-on-a-string orientation (25). Consequently, loosely packed nucleosomes are known as euchromatin and this "open" configuration is more associated with transcriptional activation. On the other hand, the nuclear machinery highly condenses chromatosomes to form heterochromatin, which is associated with transcriptional repression and chromosome condensation (22). Nonetheless, chromatin is dynamic and large parts of it are in constant alternation between these two states (euchromatin and heterochromatin), manipulated by remodelers to facilitate transcription, replication and DNA repair processes (Figure 2).

Nucleosomes are further post-translationally modified (PTM) by enzymes that phosphorylate, methylate, acetylate, ubiquitinate, or sumoylate the histone tails in order to signal the transcriptional machinery and, either repress or activate expression of target genes (22). First, histone acetylation is the addition of acetyl groups onto the lysine (K) residues of the varied

histone tails. Acetyl groups neutralize the charge of the histone tails, which loosens the attraction to the genomic strand, resulting in a less constricted nucleosome (26). More relaxed nucleosomes prevent the generation of heterochromatin and increase the rates of transcription at, or near acetylated regions. Also, acetylated histones can also become signals. For example, some bromodomain proteins interact with acetylated histones in order to promote transcription (26). In the nucleus, there are histone acetylases (HATs) and histone deacetylases (HDACs) which are enzymes in charge of adding and removing acetyl groups from the varied histone proteins, respectively (26). One example is the acetylation of H3 lysine 56 (H3K56), preventing the formation of heterochromatic regions. This increased DNA availability is suggested to be critical for DNA repair and synthesis (27).

Lysine methylation is another major histone PTM which exists in three states: mono-, di- or trimethylated. The methyl group (or groups) added to the histone proteins do not change the charge nor the interaction of the proteins with the DNA strand, rather they serve as signals (28). Proteins which 'read' these signals must contain specific domains to distinguish between the different states of methylation. These 'reader' proteins are then in charge of carrying the effect intended by these methylation marks (28). For example, the trimethylation of H3K4, H3K36 and H3K79 are all considered to be activating signals for expression, while H3K9, H3K27 and H3K40 are signals considered for repression and to maintain heterochromatin states (28). Histone methyltransferases are enzymes in charge of placing the methyl groups, also known are "writers" and, histone demethylases are those enzymes known as "erasers" which are in charge of removing these methylated groups (28). A key transcriptional modification is the tri-methylation of H3K4 (H3K4me3), which has been shown to be a critical transcriptional activator mark in multiple eukaryotic species (29).

In addition, there are also histone variants which are histone proteins similar to the canonical histones but are encoded by separate genes and carry slightly different set of amino acids (30). These variants can replace the core histones under certain circumstances and are also potentially subjected to the same PTM (30). Histone chaperons are the proteins in charge of the targeted histone deposition. There are a wide array of chaperons which are specific to different histone variants as well as to the different stages of the cell-cycle (30). For example, NAP1 is a chaperone in charge of placing histone protein H2A.Z, a variant of H2A which is also associated with promoter regions of the genome (22).

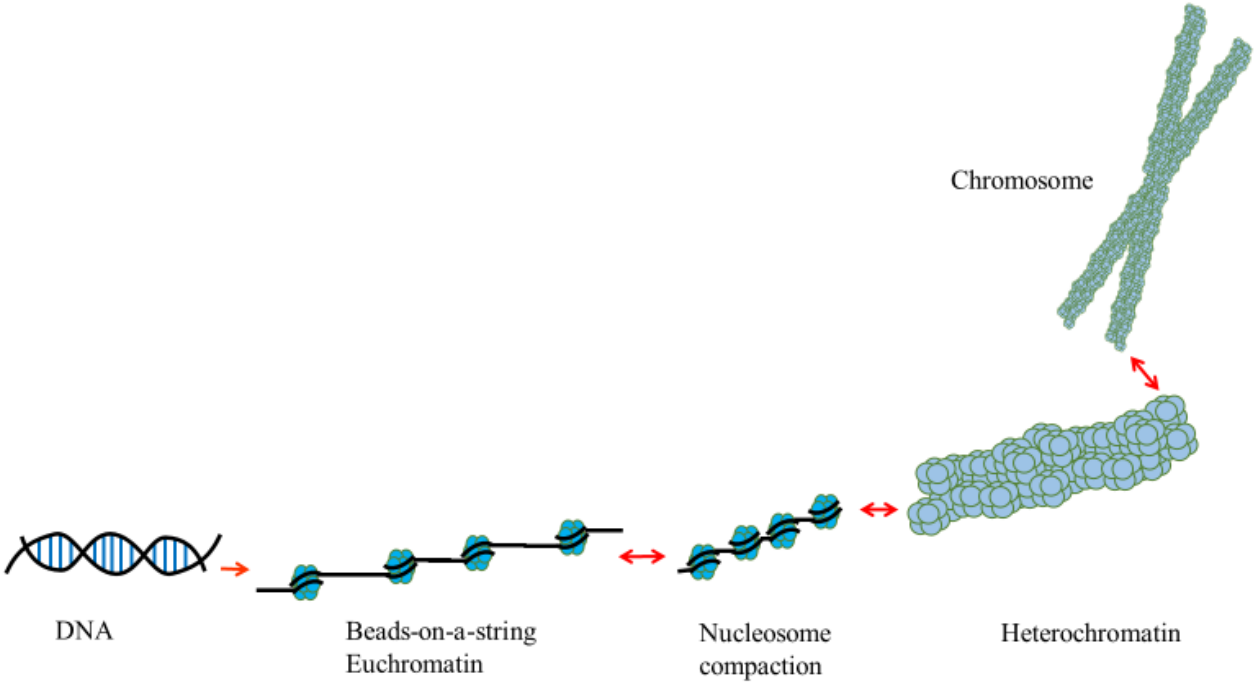

Figure 2 **DNA compaction into nucleosomes and diverse forms of chromatin.**
Simple schematic displaying the different states of the chromatin, adapted from Fyodorov et al. From left to right: double helix DNA strand, far apart nucleosomes forming the beads-on-a-string conformation, also known as euchromatin. Next, nucleosome compaction is a dynamic interstate between euchromatin and the highly condensed heterochromatin. Heterochromatin then condenses even more to form the chromosomes observed in anaphase during mitosis.

1.4. Chromatin remodelers, their mode of function and role in neurodevelopmental disorders

Chromatin remodeling, in contrast to histone PTMs, is an energy driven process and requires the consumption of ATP. The energy released by the hydrolysis of ATP is used by chromatin remodelers to release DNA from histones, switch histone subunits and/or to rearrange the spacing between nucleosomes (32). This active mobilization of the genomic strand allows for DNA repair, replication and the regulation of transcription to occur. In order for the remodeler complexes to actively manipulate chromatin organization, they are required to have DNA and/or histone binding protein subunits, as well as an ATPase subunit to actively displace nucleosomes or exchange histone proteins (32, 33). Consequently, chromatin remodelers are complexes that contain a single ATPase subunit plus a wide array of associated subunits (33). These distinct subunits can then interact with either histone subunits, their PTMs, DNA, or other transcription factors. Therefore, the combination of multiple ATPases with a large array of subunits leads to the formation of diverse chromatin remodelers which perform diverse functions depending on cell-type, timing or tissue specific requirements (33).

The ATPase subunits contained in all chromatin remodelers (Figure 3), belong to the SNF2 family of DNA helicases (34). Based on protein sequence similarities the human SNF2 family can be further subdivided into 4 main groups: SWI/SNF (switch/sucrose non-fermentable), ISWI (imitation SWI), CHD (chromodomain helicase DNA-binding), INO80 (SWI2/SNF2 related SWR) and an orphan single remodeling protein called ATRX (Alpha-Thalassemia/mental Retardation Syndrome, X-Linked) (33, 35).

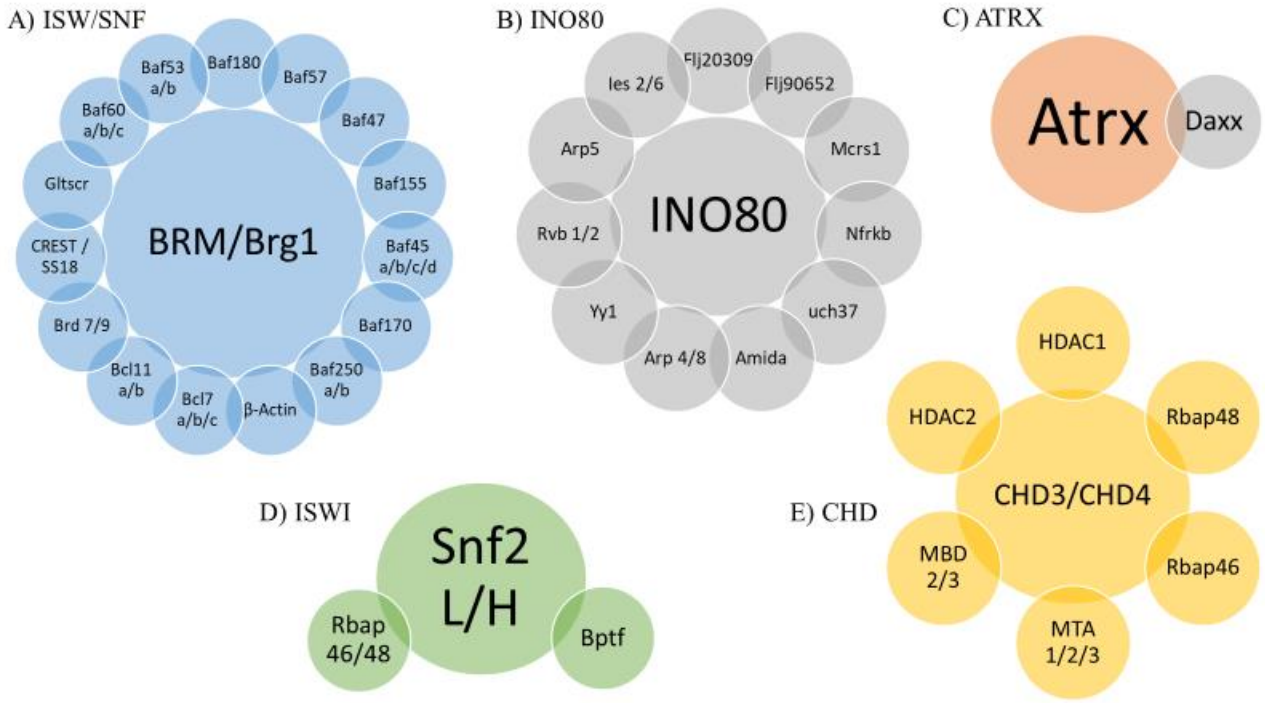

Figure 3 **Examples of the different families of chromatin remodeling complexes.**
Schematic depicting an example of chromatin remodeling complexes from each family of ATPase remodelers, adapted from Hota & Bruneau (33). A-E) internal major circle represent the ATPase subunit of each complex. A) The ISW/SNF BAF complex. B) The INO80 complex from the INO80 family. C) The ATRX protein with its heterodimer, DAXX. D) The NURF complex from the ISWI sub-family. E) The NuRD complex from the CHD sub-family

1.4.1. SWI/SNF

The founding member of the SNF2 family, SWI2/SNF2, is the catalytic component of the SWI/SNF complex and was identified in two different genetic screens in yeast. The first screen was performed to identify genes involved in mating type switching (SWI) and the second for genes critical for sucrose fermentation (SNF) (23). The mammalian SWI/SNF complex contains two different ATPase proteins, Brahma (Brm) and Brahma-related gene 1 (Brg1) (33). Brm or Brg1 alongside their associated subunits form the mammalian BAF complexes (32). These two ATPase proteins are mutually exclusive and BAF complexes will only contain one of them at a time (32). Regardless, BAF forms the largest remodeler complex found in mammals as it

contains the greatest repertoire of associated subunits, at least 15 different proteins for either Brm or Brg1 (33).

Functional yeast studies by Dechassa et al. (36), demonstrated that the SWI/SNF complex binds to the nucleosome, forms a DNA strand loop, and spins the histone octamer in order to displace the DNA around the octamer. By displacing nucleosomes and exposing the regulatory elements of the genomic strand, the complex enables transcriptional regulation of critical genes. Furthermore, previous research has demonstrated that the mammalian BAF complex has a role in heat-shock response, has cell-type specific tumor-supressing roles and more importantly, controls gene expression during development (33, 34). The BAF complex also contains Baf47, Baf155 and Baf170 proteins which maintain the integrity of the complex as a whole and, are essential for its remodeling activities (37). Baf155 and Baf170 have been knocked out in the mouse cortex. These experiments demonstrated the BAF complex to be critical for the deposition of repressive H3K27me3 and for the activating H3K4me3 mark due to its interactions with H3 methylases (38). The authors argue that the altered pro-neural gene expression program leads to the aberrant behaviour of cortical progenitor cells, preventing adequate embryonic forebrain development (38). This study demonstrated that the BAF complex is essential for mammalian development, nucleosome rearrangement and for the deposition of essential histone PTMs.

The BAF chromatin remodeling complex has been thoroughly linked with multiple neurodevelopmental disorders and can be used to provide a great deal of understanding of the significance of chromatin remodelers. *De novo* mutations in BAF subunits ARID1A, ARID1B, SMARCB1, BRM and BRG1 have been identified to cause Coffin-Siris Syndrome (CSS) (39). The mutations implicated in ARID1A and ARID1B were only occurring in one allele, demonstrating that haploinsufficiency of either of these genes is sufficient to cause CSS.

Furthermore, BRG1 has also been demonstrated to be involved in ASD (40). *Brg1* heterozygous mutant mice demonstrate exencephaly, while homozygous mutant mice die early in development (41). Similarly, human in-frame deletions and missense mutations in the BRM gene have been demonstrated to develop Nicolaides-Baraitser Syndrome, while single nucleotide polymorphisms (SNPs) affecting its expression levels in the cortex have also been associated with the development of schizophrenia (42, 43). Highlighting the importance of Brg1, Brm and the entire BAF complex in neural development and how their mutations lead to the development of several intellectual and neurodevelopmental disabilities.

1.4.2. CHD

The human CHD family contains 9 documented CHD ATPase proteins which are divided into three groups: CHDI, II and III (44). The CHDI sub-category is directly involved in nucleosome spacing to regulate chromatin organization is essential for transcription. Chd1, which is part of the CHDI group, interacts with Nap1 to catalyze the addition and ejection of nucleosomes, regulating their spacing (44, 45). On the other hand, the CHDII sub-category is known for gene repressive roles. Chd3 and Chd4 have been shown to interact with histone deacetylases such as Hdac1 and Hdac2 in order to remove acetyl PTM from histone proteins, tightening the DNA around the octamer (23, 32). Murine knockdown experiments have demonstrated that Chd1 and Chd4 function co-operatively to regulate the development of zygote endodermal layers by controlling key target genes involved in cell-lineage specification (130, 131). Furthermore, Chd3, Chd4 and Chd5 ATPase subunits of the NuRD (nucleosome remodelling and deacetylase) complex were independently knocked out in the mouse, demonstrating that each subunit has a specific role during the differentiation process of the cortex (46). Where Chd4 is necessary for progenitor pool proliferation, Chd5 ensures adequate neuronal

migration to the cortical plate and, Chd3 is involved in neuronal cell-type specification (46). Further supporting the role of chromatin remodelers manipulating nucleosome spacing and histone modifications in order to control gene expression involved in cortical cell-fate pathways.

ASD is an extremely complex disease with the involvement of multiple genes and numerous diverging phenotypes. CHD8 mutations have been associated with ASD and actually display a distinct subtype of the disease, with distinct macrocephalic features (47, 48). Separately, 10 unrelated cases of human fetuses were diagnosed with CHARGE syndrome, all of which had truncating mutations in the CHD7 gene (49).

1.4.3. INO80

The INO80 family was initially identified by a genetic screen experiment performed in *S. cerevisiae*, noting the role of this complex in maintaining expression of inositol-regulated genes (23). In mammals, the family consists of three main sub-categorical complexes: INO80, a SNF2-related CBP activator protein (SRCAP) and TIP60/P400 (32). RNA interference (RNAi) was used to inhibit *INO80* in human HeLa cells, which demonstrated drastic expression changes primarily on cell-cycle regulation, arguing that the INO80 complex has a significant role in gene regulation and cell cycle progression (50, 51). Also, this complex modulates chromatin accessibility of key TF required for murine embryonic stem cell (ESC) self-renewal (52). Separately, the SRCAP complex has been demonstrated to evict H2A histone subunits and replace them with the H2A.Z variant (32, 51). Lastly, the P400 complex acetylates H4 variants to increase accessibility of the DNA, critical for damage response process (44).

INO80 encodes for the ATPase subunit of the INO80 complex, which has been identified as a novel candidate gene to cause microcephaly and intellectual disability (ID) (53). Furthermore, the YY1APA1 is another component of the INO80 complex. Exome sequencing

demonstrated that some patients with Grange syndrome (vascular and intellectual disability disease) contained heterozygous (Het) nonsense and homozygous frameshift variants of the *YY1APA1* gene (54). Separately, SRCAP complex mutations have been suggested to cause Floating harbour syndrome, an intellectual disability condition characterized by short stature, language deficits and distinct facial features (55).

1.4.4. ATRX

The ATRX remodeler has high sequence similarity to the SNF2 family but it is either not regularly considered as part of the larger family of remodelers or is only mentioned in the literature as an orphan member (56). ATRX was first discovered as the cause of the ATR-X syndrome (α-Thalassemia mental retardation X-linked), an intellectual disability disorder mainly present in males characterized by the presence of α-thalassemia, genital abnormalities and distinct facial features (57). Atrx interacts with, and is mostly found in association with, a histone chaperone called Daxx (58). The mammalian Atrx together with Daxx have been demonstrated to distribute the histone variant H3.3 specifically at telomeric locations (59, 60). Furthermore, Atrx co-localizes at heterochromatic regions at early stages of the mouse embryo (56). Lastly, Atrx has also been observed to be critical for the maintenance of G-rich tandem repeats (TRs). When ATRX is mutated in human patients, the expression of certain genes near these G-rich TRs becomes disparate (57, 58). Further demonstrating that ATRX is needed for histone deposition and is essential for adequate gene expression.

1.4.5. ISWI

The protein of interest regarding this thesis belongs to the remaining sub-category of the SWI/SNF superfamily, the ISWI complexes. SNF2H (SMARCA5) and SNF2L (SMARCA1) are the ATPase catalytic subunits of the ISWI protein family (35). The *Drosophila* ISWI protein is

the homolog to both human SNF2H and SNF2L ATPases (127). Both proteins are approximately 85% identical and both are expressed throughout the entire CNS of the developing mouse (61). It is suggested however, that in the murine brain, Snf2h is more commonly expressed in the proliferating progenitor cells, while Snf2l is more dominant later on, in differentiated neurons (61). There is a total of seven regulatory subunits to which the ATPase proteins can bind to: Acf1 (Baz1a), Wstf (Baz1b), Tip5 (Baz2a), Bptf, Cecr2, Rsf1 and Baz2b (62). Each of these subunits when bound to the ISWI subunit (either Snf2l or Snf2h) as well as other independent supporting proteins form unique complexes: ACF, WICH, NoRC, NURF, CERF, RSF and BRF, respectively (63). There are also two extended ISWI complexes: CHRAC and the SNF2H/cohesin complex (64, 65). It has been suggested that both Snf2h and Snf2l are interchangeable and can interact with all of the aforementioned regulatory proteins (66). Meaning that there is a total of seven regulatory subunits but, with the two possible ATPases, there is a total of 14 complexes that can form within the ISWI family of remodelers. The ISWI ATPase proteins contain HAND-SANT-SLIDE domains which promote the displacement of nucleosomes (67, 68). These complexes do not eject nor replace histone proteins, only slide the nucleosomes and expose the genomic strand (23, 68).

Whole exome sequencing (WES) from various sources have identified novel variants in SMARCA1 (SNF2L) which led to the identification of a patient identified with Rett syndrome (69). Furthermore, a separate patient with microcephaly and IDD was also identified to carry a SMARCA1 hemizygous mutation (35, 70).

NURF, the ISWI complex pertaining to this thesis, was first purified from *D. melanogaster*, it contains 4 subunits: NURF301, NURF140 (equivalent of Snf2l) NURF55, and NURF38 (129). In mammals, the NURF complex is compromised of four subunits: ISWI

ATPase (Snf2l), two closely related small subunits called Rbap46 and Rbap48 and the large Bptf (Bromodomain PHD transcription factor) protein, which maintains the integrity of the complex (71). Previous studies in yeast, have demonstrated that the NURF complex works to displace the nucleosomes, 10 bp at a time, to a thermodynamically favourable position and expose relevant genetic regulatory elements (72, 73).

In vitro studies using human HeLa cells have demonstrated that NURF associated with the variant H2A.Z, rather than to the canonical H2A protein (74). Ctcf binding sites are typically surrounded by nucleosomes enriched with histone variant H2A.Z, which are exposed by NURF (75). Furthermore, it is suggested NURF exposes binding sites for Ctcf and Cohesin in order to maintain distal accessible regions to ensure promoter and enhancer interactions (76). From separate groups, it has been demonstrated that SNF2H and, at a lesser extent SNF2L, modulate nucleosome spacing to expose the DNA strand on Ctcf specific binding sties, strongly suggesting NURF performs key nucleosomal modulation on Ctcf-regulated gene pathways (63, 77). Ctcf is a key transcription factor known to regulate gene expression by maintaining distal chromatin interactions as well as, prevent the formation of heterochromatic regions (78). NURF is the remodeling complex formed by the regulatory subunit Bptf (the protein of interest to this thesis), further information regarding its role within the complex and during murine development is described in section 1.5.

1.4.5.1. ISWI mouse models

Previous research has conditionally inactivated Snf2l by the removal of the ATPase domain in the mouse model. These mice displayed an increase in cortical size caused by altered Foxg1 expression which resulted in an increase in the proliferation of the cortical progenitor pool (79). Furthermore, Snf2h has also been conditionally ablated specifically in the cortex of C57Bl/6

mice. In contrast, these mice presented with a significantly reduced neocortex (80). The authors argue that the reduction of Foxg1 and Tbr2 expression in the progenitor pool leads to decreased IPC proliferation and neuronal differentiation, producing fewer late-born neurons (80). These two studies demonstrate opposing results specific to the cortex of the mouse which could suggest the involvement of different remodeling complexes. To address the role of individual complexes, this thesis characterized mice inactivated for Bptf, to identify the specific function of NURF during brain development.

1.5. Bromodomain PHD transcription factor (BPTF)

Bptf was first discovered in *D. melanogaster* and, noted to be the largest subunit of the NURF complex at ~301 kDa, hence it was named NURF301 (81). It was also noted that the remodeling activity of the NURF complex does not occur if either the ATPase subunit NURF140 (Snf2l) is not present or if NURF301 (Bptf) is removed (81). Without NURF301 the remaining subunits were not able to form interactions with one another, suggesting NURF301 serves as a backbone for complex assembly (81). Lastly, it was also demonstrated using flies that NURF301 serves to interact with transcription factors such as GAGA (81).

More relevant to this thesis, the human and mouse Bptf proteins contain the exact same domains and are fairly the same size: 2,920 and 2,921 kDa, respectively (73). There are two major domains on the N-terminus: a DDT domain and a PHD domain (Figure 4). The C-terminus contains another PHD domain side-by-side with a bromodomain (73). DDT domains are presumed to contain DNA-binding properties (82). The secondary PHD domain on the C-terminus of the Bptf protein has been demonstrated to form pockets specific to H3K4me3 marks, with decreasing affinity as the number of methyl groups decreases (83). Last, bromodomains

have been demonstrated to uniquely recognize acetylated-lysine histone proteins (84). BPTF has also been isolated in human cells and noted to include a smaller isoform of 110 amino acids known as Fetal alz-50 clone1 (FAC1/FALZ) originating from the N-terminus region (85). FAC1 recognizes and binds to specific sequences located in the promoter region of neuronal development related genes; when bound, FAC1 serves to repress their activity (86). Altogether, the domains of Bptf suggest that it can transport the NURF complex and bind to the DNA strand by recognizing several epigenetic histone modifications. This will then allow for the ISWI ATPase subunit (Snf2l) to interact with the nucleosomes near acetylated or H3K4me3 histones.

The BPTF protein has been thoroughly analyzed in flies and, it begins to gain importance as more human and mouse studies demonstrate its role in development, cancer, intellectual disability disorders, and lineage-specific differentiation. First, in flies, NURF301, through transcription activation, regulates heat-shock genes and is essential for larval blood cell development (87). Second, Bptf is essential for mouse embryonic development; without both copies of the gene, mouse embryos die post-implantation between E7.5 – E8.5 (88). Of note, heterozygote mice did not demonstrate embryonic lethality like the full $Bptf^{-/-}$ mutant mice (88). The Bptf protein was shown to be essential for the development of the murine visceral endoderm, regulating proliferation mainly through transcription control of the Smad pathway (88). Studies using mouse embryonic fibroblasts, demonstrated that Bptf is required for their proliferation and transition from G1 to S-phase of the cell cycle, through its interaction with the c-MYC TF (89). Similarly, Bptf is essential for the maintenance of T-cell homeostasis and the development of Treg cells in mice (90). Furthermore, Bptf was demonstrated to be critical for the proliferation and differentiation of mammary stem cells, through the regulation of genetic pathways essential for their cell-fate development (91). Bptf has also been demonstrated to regulate key transcription

factors essential for the self-renewal and differentiation capabilities of hematopoietic stem cells (92). Lastly, it was demonstrated that Bptf maintains expression control of melanocyte markers and allows for the terminal differentiation of mouse melanocytes stem cells to melanin expressing melanocytes (93). The overexpression of Bptf in melanoma tumors was also linked with increased tumor progression and increased metastasis in mouse xenografts (94). Overall, these studies demonstrate the requirement for a fully functioning BPTF protein.

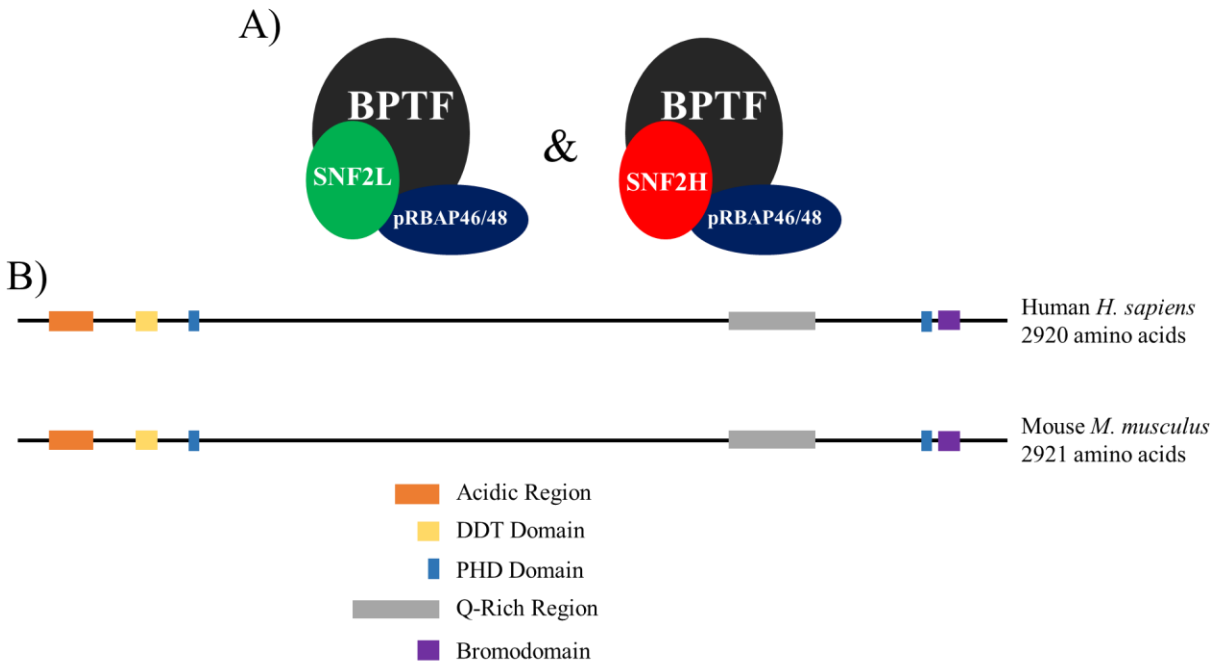

Figure 4 **The Bptf protein of the NURF complex.**
A) Schematic representing the mammalian Bptf, forming the NURF complex with either the Snf2l or the Snf2h ISWI ATPase subunit. B) Schematic adapted from Alkhatib & Landry (73) demonstrating the comparison between the human BPTF protein and the mouse Bptf (N-terminus on the left and C-terminus on the right), with their respective active domains and protein size (aa).

1.6. Neurodevelopmental disorder with dysmorphic facies and distal limb anomalies

A novel human neurodevelopmental syndrome caused by mutations in the BPTF gene was recently described (95). To date, 11 human patients have been identified with loss-of-function (LoF) or missense mutations in a single BPTF allele (Figure 5). Seven of the eleven patients had frameshift and nonsense mutations, while two patients had CNV deletions of the BPTF gene. Two additional patients had missense mutations that were argued to be detrimental to protein structure (95, 96). All these unrelated patients are considered haploinsufficient for BPTF protein and argued to be responsible for the neurodevelopmental disorder with dysmorphic facies and distal limb anomalies (NEDDFL). This novel syndrome, firstly identified in 2017, is mainly characterized by the developmental delay (DD)/intellectual disability (ID) present in 11/11 patients, speech delay in 11/11, dysmorphic facial and limbic features in 10/11, motor delay present in 9/11, as well as microcephaly identified in 8/11 patients. Only one of the patients above is an adult (35 year-old male). He was initially reported to have Silver-Russel syndrome, but a recent secondary observation described his condition to be the novel NEDDFL syndrome, based on facial and limb features as well as a 4.9 kb deletion in intron 25 in one BPTF allele (96). The remaining ten cases are male and female children not older than 12 years of age, none of which are homozygous BPTF mutants (95, 96). Similar to the adult patient, it is possible that other patients were miscategorized. Further testing and identification of this novel syndrome should increase the understanding and help illuminate unknown distinct features of the disease. Overall, it is argued that the haploinsufficiency of BPTF leads to an increase in neuronal cell death which could be the reason for the microcephaly observed in the patients and the neurodevelopmental abnormalities (95, 96).

Figure 5 **Patients with the novel Neurodevelopmental disorder with dysmorphic facies and distal limb anomalies (NEDDFL).**

Patients from Stankiewicz et al (95) and Midro et al (96).

Subject 1. Male patient, 7.9 (years.months) old. Frameshift mutation on exon 13. Severe developmental delay, positive for microcephaly and positive for speech delay.

Subject 2. Male patient, 13 years old. Splicing and Frameshift mutation on exon 12. moderate ASD, positive for microcephaly and positive for speech delay.

Subject 3. Male patient, 11 years old. Missense mutation on exon 14. Severe developmental delay, negative for microcephaly and positive for speech delay.

Subject 4. Male adult patient, 35 years old. 4.9 kb deletion in intron 25. Positive for intellectual, and speech delay and microcephaly. (E-I) Also, displaying the dysmorphic fingers and toes.

Subject 5. Female patient, 11 years old. Missense mutation in exon 29. Mild developmental delay, positive for microcephaly and speech delay.

Subject 6. Male patient, 7.11 years old. Frameshift mutation in exon 2. Moderate aggression and distractedness, positive for microcephaly and speech delay.

Subject 7. Female patient, 12 years of age. Frameshift mutation in exon 8. Displaying Mild developmental delay and positive for both microcephaly and speech delay

1.7. Hypothesis & thesis aims

Murine Bptf is capable of forming NURF complexes with both Snf2l and Snf2h (66). Snf2l conditional knockouts (cKO) have an increase cortical size while Snf2h cKO mice have a reduced cortex (79, 80). Furthermore, most of the NEDDFL human patients display microcephalic features, suggesting BPTF plays an important role in progenitor proliferation and neocortical expansion alongside either of the ISWI ATPase proteins. Therefore, it is hypothesized that BPTF is essential for normal neocortical development to occur and without it, the mouse models will recapitulate the phenotypes displayed by the human NEDDFL patients. To address this hypothesis, we propose the following aims:

1. Identify any alterations within the brain of *Bptf* cKO animals at multiple timepoints during brain development.
2. Through molecular analyses, such as RNAseq, identify the altered gene expression programs and locate possible *Bptf* target genes

2. Materials & Methods

2.1.Transgenic mice

2.1.1. Animal Husbandry

Animals were housed in the Animal Care and Veterinary Services (ACVS) facility of the University of Ottawa. The facilities meet the regulation of the Ontario Ministry of Agriculture and Rural Affairs (OMAFRA) under the Animals for Research Act and the Canadian Council of Animal Care standards. The mice were maintained under normal light and dark cycles in stimulating and stress-free cages, with continuously available food and water. All experiments were then performed according to the guidelines set by the University of Ottawa's Animal Care ethics committee, maintaining the standards set by the Canadian Council on Animal Care.

2.1.2. Mouse lines

2.1.2.1. *Bptf* loxp lines

The *Bptf* homozygous flox (*Bptf* $^{f/f}$) animals were donated by Dr. Camila dos Santos from the Cold Spring Harbor Laboratory (91) which, were originally generated by Landry et al. (88). These animals contain loxp sites surrounding exon 2 of the *Bptf* gene. When the Cre enzyme removes exon 2, the mRNA transcripts become out of frame and behave as LoF alleles. The *Bptf* $^{f/f}$ mice were maintained on a C57B/6 background.

2.1.2.2. Cre driver lines

Two separate Cre recombinase expressing, C57B/6 mouse lines were used to conditionally remove exon 2 of the *Bptf* gene: *Nestin* Cre and *Emx1* Cre. *Nestin* gene expression starts at E7.5 and it is expressed in the entire CNS of the mouse embryo by E14.5 (97). The Cre transgene including a CNS-specific enhancer, was introduced in the 5’ region in between the

promoter and the transcriptional start site (TSS) of the *Nestin* gene (97, 98). *Bptf* $^{f/f}$ females were bred with *Bptf* $^{f/+}$ :: *Nestin* Cre $^{+/-}$ male mice to produce cKO *Bptf* $^{f/f}$ :: *Nestin* Cre $^{+/-}$ (NcKOs) mice and, Hets *Bptf* $^{f/+}$ :: *Nestin* Cre $^{+/-}$ animals. *Emx1* expression is first noted at E10.5 and, by E12.5 it is expressed in almost every progenitor and neuron of the pallia (99). The IRES (internal ribosome entry site) and Cre coding locus were introduced between the last exon and the 3'-UTR (untranslated region), thus ensuring Cre expression without altering *Emx1* levels (99). *Bptf* $^{f/f}$ females were bred with *Bptf* $^{f/+}$ :: *Emx1* Cre $^{+/-}$ male mice, to produce cKO *Bptf* $^{f/f}$ :: *Emx1* Cre $^{+/-}$ (EcKOs) mice and, Hets *Bptf* $^{f/+}$ :: *Emx1* Cre $^{+/-}$ animals.

2.1.3. Genotyping

A small (< 5 mm) tail clip was added to lysis buffer containing 0.95 N NaOH and 7.6 mM EDTA at a pH of 8. The solution was then placed in a PCR thermocycler (Eppendorf Mastercycler EP Gradient 96 well thermal cycler) at 90° C for 60 minutes. Once finished, neutralization buffer (0.97 M Tris-HCl pH 8.1) was added to the lysed solution and left to homogenize and settle for 45 minutes. This was repeated for all mice, each PCR tube containing a small tail clip from each mouse. 1.4 µL of each crude homogenized sample, containing genomic DNA was used to perform a PCR reaction using primers specific for the floxed *Bptf* alleles, the Cre allele and sex was determined using primers for the SRY gene (Appendix Table 7). The PCR mixture for each sample, described in Table 1, was added into a thermocycler in order to amplify the template of interest, under the following conditions: 94°C for 2 min, 39 PCR cycles (94°C for 30 sec, 60°C for 30 sec, 72°C for 45 sec) and a final cycle at 72°C for 10 min. Subsequently, an aliquot of each PCR reaction was electrophoresed in a 1.5% agarose gel (containing ethidium bromide) at 80 V for 45 minutes. Amplified PCR products were visualized

by incorporating ethidium, bromide (amount) into the agarose gel followed by imaging on a ChemiDoc-It Imager (UVP).

Table 1 **PCR reaction mix.**
Table depicting the amount added and the final concentration of solutions to formulate a single PCR reaction.

Solution	Volume	Final Concentration
Crude lysed sample	1.4 µL	
10X PCR Buffer	2.5 µL	1X
2.5mM dNTPs	2.5 µL	0.25 mM
50mM $MgCl_2$	0.75 µL	1.5 mM
10uM Forward primer	0.5 µL	0.2 mM
10uM Reverse primer	0.5 µL	0.2 mM
Taq Polymerase	0.25 µL	
dd H_2O	16.4 µL	
Total per reaction	25 µL	

2.1.4. Timed Breeding

In order to obtain embryonic and post-natal pups of a desired age, timed breedings were performed. Male mice *Bptf* $^{f/+}$ :: $Cre^{+/-}$ (as described in 2.1.2) were normally kept separate from female *Bptf* $^{f/f}$ mice and were only placed together, into a single cage, for ~12 hours once a week (same day, every week). The day in which the mice were separated from the same cage was considered as embryonic day 0.5 (E0.5), adding the half day due to uncertainty as to the exact time of conception. The following day was considered as E1.5 and the days were then counted

sequentially. Female pregnant mice were sacrificed (CO2 gas chamber), and embryos collected at either E13.5 or E15.5, or alternatively, pregnant dams were allowed to give birth prior to collection of pups (P0, P2 or P7) for analysis, as needed.

2.2. Tissue dissection for nucleic acid or protein extraction

Before dissection, mice were euthanized by CO_2 asphyxiation and weighed in order to keep track of the WT and EcKO growth at P0 and P2. The mean weight of each cohort was quantified and tested for significance by a parametric, unpaired t-test, also providing the standard error of the mean (SEM). Consequently, cortical tissue was used for two experimental pathways following dissection: either for the extraction of nucleic acids and proteins or, for histochemistry experiments that required tissue fixation and cryopreservation, cryosectioning and staining. For nucleic acid or protein extraction the dissected brain or cortical tissue was added into a Cryotube (Sarstedt, catalog# 72.380.992) and placed into liquid nitrogen for instantaneous freezing. Tissue samples were subsequently stored in -80° C for preservation until use (as described in section 2.4). Tissue designated for histochemistry was prepared differently between extremely young mice (E15.5 – P5) and older (P10 and older) animals. Mice that were above the age of P10 were euthanized followed by cardiac perfusion using 4% PFA ([Sigma], in autoclaved 1X PBS) in order to remove the blood from the brain tissue and facilitate neurovasculature fixation. Perfusion was followed by brain tissue dissection and 4% PFA fixation overnight (4° C). Mice which were below the age of P10 were not perfused, and the brain tissue was simply added to 4% PFA overnight for fixation (4° C).

2.3. Analysis of cortical tissue

2.3.1. Cryo-sectioning of fixed tissue

Following fixation, tissue was placed in a 30% sucrose solution (in autoclaved 1X PBS and 0.03% sodium azide) at 4 °C until the brain tissue fully absorbed the 30% sucrose. The tissue was then placed in a 1:1 solution of 30% sucrose and optimal cutting temperature compound (OCT from VWR) overnight at 4 °C. The next day, the tissue with its sucrose:OCT solution was placed in an embedding mold (VWR) and, the entire mold was then placed floating on liquid nitrogen for flash freezing. The frozen tissue (stored at -80° C) was later sectioned using a Leica CM1850 cryostat and the sections picked up using SuperFrost slides (Thermo Fisher Scientific). Brains were cut at 12 μm thickness in a coronal or sagittal orientation and left to dry at room temperature (RT) for 1 hour followed by storage at -80 °C.

2.3.2. Nissl staining

Histochemical Nissl staining was performed as follows; sectioned slides were rehydrated by sequentially submerging them in 95% ethanol (diluted in water, for 10 minutes), 70% ethanol (1 minute), 50% ethanol (1 minute), and ddH2O (5 minutes x 2). Rehydrated slides were stained using a 0.25% cresyl violet (Thermo Fisher Scientific) solution (15 minutes) and then washed in ddH2O (4 minutes x 2). The slides were then dehydrated in 50% ethanol (2 minutes), 70% ethanol with 0.5% acetic acid (5 seconds), 95% ethanol (2 minutes), followed by xylene substitute (5 minutes, Sigma, catalog# A5597-1GAL). The slides were then allowed to dry for less than 1 minute followed by addition of Permount solution (Thermo Fisher Scientific) to mount the coverslips (Thermo Fisher Scientific). The stained sections were then imaged and arranged based on coronal or sagittal orientation, matching sections as much as possible to the same anatomical landmarks of the brain for accurate comparison between control and treatment

groups. Positive signal was imaged under a M2 brightfield microscope (Carl Zeiss Axio Imager M2).

2.3.3. Immunofluorescent staining

Slides containing cortical sections were first left to warm up (from -80° C) at RT for 1 hour, washed with 1X PBS and subjected to antigen retrieval. For antigen retrieval, sodium citrate solution (pH 6) was heated until boiling, for approximately 2 minutes at high power in the microwave. The slides were then placed in the warm citrate solution and reheated for another 10 minutes at low power. After antigen retrieval, all slides were washed with 1X PBS (x3) and blocked with blocking buffer (10% horse serum in 1X PBS with 0.4% Triton X-100) for 30 minutes at RT. Following blocking, slides were incubated with a specific primary antibody (diluted in blocking buffer) overnight at 4 °C (primary antibodies and dilutions used are listed in Appendix Table 8). The next day, slides were washed with 1X PBS (x3) and incubated for 1 hour with secondary antibody specific to the species of the primary antibody (in 1X PBS with 0.4% Triton X-100). After the secondary antibody incubation, all slides were washed with 1X PBS (x2) and incubated with Hoechst dye for 15 minutes. Finally, the slides were washed with 1X PBS to clean the sections for mounting with coverslips using Dako faramount aqueous mounting medium (Dako) and ordinary nail polish to seal the coverslip with the slide. The entire list of primary and secondary antibodies used, their dilution and, the company of origin is provided in Appendix Table 8.

2.3.4. EdU pulse labelling

To label embryonic S-phase cells, pregnant mothers were injected subcutaneously near the bottom of the abdomen, avoiding the embryonic sacs, and close to either of the legs with 10 mg/ml EdU (Santa Cruz). The amount of EdU injected was 10 µl per g of the female's total

weight. EdU injections were performed for three separate types of experimental analysis: to quantify cells in S-phase (1-hour pulse); to assess cell cycle exit (24-hour pulse) and for neuronal birthdating (injected at E13.5 and harvested at P2). The S-phase experiment involved EdU injection at E15.5 followed by forebrain dissection 1 hour later. For cell cycle exit studies, EdU injection occurred at E14.5 followed by pregnant female sacrifice 24-hours later (CO_2 asphyxiation). The E15.5 embryos were extracted, and forebrain tissue isolated followed by fixation as described in section 2.2 and 2.3.3. For the birthdating experiment, EdU was injected at E13.5 and the pups were collected at P2. Once the brain tissue (either E15.5 or P2) was fixed and sectioned, the EdU click chemistry step was performed following the primary antibody incubation and before the secondary antibody incubation step (described in section 2.3.3), as follows. First, the sections which were left overnight following primary antibody incubation, were washed with 1X PBS for 10 minutes (x3), followed by the EdU chemistry solution incubated for 1 hour at RT. This solution contained 2 mM CuSO4, 10 μM fluorescent azide (Cy-5-Azide, Sigma catalog # 777323-1MG) and 50 mM ascorbic acid. Followed incubation, the slides were then washed again with 1X PBS (5 min x3) in preparation for the secondary antibody incubation step

2.3.5. *In-situ* Hybridization

The *in-situ* hybridization procedure was performed by Keqin Yan[1], as described by Jensen and Wallace (100). Briefly, a pBluescript KS vector (Addgene) was ligated with a PCR product containing *Bptf* exon 2 originating from forebrain-specific WT cDNA, using newly designed primers (Appendix Table 7). Following transformation and digestions (EcoRI [Thermo Fisher

[1] Staining of brain sections for the *in-situ* hybridization experiment was performed by Senior Lab. Technician, Keqin Yan M.Sc (Dr. Picketts' lab).

Scientific, catalog# FD0275] making sense probe for negative control and BamHI [New England Biolabs, catalog# R0136S] to make antisense probe), a 671bp DIG-11-UTP labeled antisense RNA probe complementary to exon 2 of the *Bptf* transcript was synthesized from the transformed vector using the DIG RNA labeling kit (Roche #11175025910). RNA synthesis using the mix described in Table 2 was performed in a thermocycler (Eppendorf Mastercycler EP Gradient 96 well thermal cycler). The final product was then diluted in hybridization buffer (1X Salt, 50% deionized formamide, 10% dextran sulfate, rRNA [1mg/mL], 1X Denhardt's, ddH_2O) at 1:1000 dilution followed by hybridization onto E15.5 EcKO, WT and Het 12 µm brain coronal sections and left to incubate overnight at 65°C. The next day, sections were washed (1X PBS), blocked (20% horse/sheep serum in 1X PBST) and hybridized overnight with anti-DIG antibody (Roche #11093274910). After washing (1X PBS), the colour chemical reaction was performed in a staining buffer containing NBT and BCIP (Alkaline Phosphatase chromogen, Roche #11681451001) in a 37°C, void of light, water bath overnight. The reaction was stopped the following day and sections were cleaned in 1X PBS and mounted in PBS/glycerol at a 1:1 ratio. Positive signal was imaged under a M2 brightfield microscope (Carl Zeiss Axio Imager M2).

Table 2 **DIG RNA synthesis reaction mix.**
Table depicting the amount added and the final concentration of solutions to formulate a single RNA synthesis reaction.

Solution	volume	Final Concentration
DNA (transformed vector)	12.5 µL	1 µg
10X Buffer	2.5 µL	1X
RNase out Inhibitor (20 U/µL)	1 µL	.8 U/µL
10X DIG mix (Rocher)	2.5	1 X
Hplc H_2O	5.5 µL	
Total per reaction	25 µL	

2.3.6. Quantification of stained tissue

The immunofluorescent (IF) stained sections were used to acquire images at 20X magnification (using a Carl Zeiss Axio Imager M1 microscope) to visualize and to count the proportion of marker positive (+ve) stained cells. Software used for image processing was AxioVision SE64 Rel. 4.9.1 and the quantification of cells was performed using the Adobe Photoshop CC 2015 software. From the coronal cortical images acquired, a small rectangle of the cortex was isolated, as a representation of the state of the entire cortex. This rectangle was 133 µm (250 pixels) wide and as long as the entire cortex. All the rectangles used for counting were isolated in this manner, unless otherwise specified. The mean cell number (any marker positive cell) was acquired from a minimum of three sections from at least three biological replicates. In order to statistically quantify the proportional means of the marker positive cells, comparing the three groups (WT, Het and EcKO), a one-way parametric ANOVA was used comparing the means of each treatment group. The bar graphical representations illustrate the mean +/- the SEM and the significance thresholds demonstrated with "*", as specified within each quantification

2.4. Nucleic acid isolation from frozen tissue

2.4.1. RNA isolation

The flash frozen tissue described in section 2.2 was maintained frozen at -80° C until its use, in order to prevent RNA degradation. Once out of the freezer, the tissue was immediately placed in TRIzol reagent (Thermo Fisher Scientific) which, was used to prepare RNA following the manufacturer's instructions. Briefly, the tissue was homogenized and centrifuged with chloroform at 12,000 g for 15 minutes. The top aqueous layer containing the RNA was then extracted, from which the RNA was then precipitated using isopropanol and centrifuged again. The pelleted RNA was then washed with 75% ethanol and solubilized in HPLC grade water.

RNA quality was checked by running a small amount of RNA (0.5 µg) in a 1% agarose gel at 180 V for 8 minutes. The gel was imaged using the ChemiDoc-It Imager (UVP). The quality of 28S, 18S and 5S ribosome was evaluated by examining the clarity of all bands on the gel. RNA quality was further validated using the Nanodrop 1000 (Thermo Fisher Scientific) to measure the 280/260 nm and 260/230 nm ratio, ensuring a ratio close to ~2 was obtained for both measurements.

2.4.2. cDNA preparation

Prior to cDNA preparation, the sample was treated with DNase I (2Units / µL) to remove contaminating genomic DNA using the RNA-free DNA Removal Kit (Invitrogen) according to the manufacturer's instructions. Briefly, 1 µL of rDNase I (2Units / µL) was introduced into a solution containing 1 µg of RNA used as input. rDNase I was left to incubate at 37° C for about half an hour, it was consequently inactivated with DNase inactivation reagent (0.1 of total volume), followed by centrifugation and RNA extraction from the top aqueous layer. Second, cDNA was generated using RevertAid Reverse Transcriptase (Thermo Fisher Scientific) and random hexamers (Thermo Fisher Scientific #SO142) as per the published RevertAid Reverse Transcriptase protocol for first strand cDNA synthesis. In brief, 0.2 µg of random hexamers were added to the 1 µg of RNA and left to anneal at 65° C for 5 min. Subsequently, 1X reaction buffer, 0.5 µL RNase inhibitor, 2 µL dNTPs (10mM each) and 1 µL RevertAid Reverse Transcriptase were added into the mixture and left to complete the reaction for 10 minutes at 25° C followed by 60 min at 45° C. Incubation of the reaction mixture was performed on an Eppendorf Master Cycler Ep Gradient Thermocycler. The final product was preserved at -20° C and aliquoted in diverse dilutions based on future need.

2.4.2.1. RT-PCR

To perform the RT-PCR experiment, a simple PCR reaction mixture was followed, as described in section 2.1.3, using 1 µl of the cDNA described in 2.4.2, in a 1:10 dilution in HPLC water. For this particular experiment, primers specific to exons 1 and 3 of the Bptf cDNA were used, as well as primers for the β-actin transcript, for control (Appendix Table 7). Following the PCR reaction, the product was run in a 1.5% agarose gel (containing ethidium bromide) at 85 V for 40 minutes. The gel was placed under a ChemiDoc-It Imager (UVP) to visualize bands, and to image the gel.

2.4.2.2. RT-qPCR

The RNA was isolated as described in 2.4.1 and cDNA was synthesized as mentioned in 2.4.2, and subsequently diluted 1:10 with HPLC water. Next, the qPCR reactions were set as described in (Table 3). Each qPCR reaction was performed in technical triplicates and with target primers to transcript of interests (Appendix Table 7). The samples were then loaded into a 96-well qPCR plate (Brooks life sciences, catalog# 4ti-0750) and, run on the Agilent Stratagene Mx3000P System. The qPCR amplification cycles were: 1 cycle at 95°C for 2 mins, 40 cycles (95°C for 5 sec, 55°C for 20 sec, 72°C for 20 sec), and 1 cycle 72°C for 5 min. Amplification plots and dissociation curves were then examined on the MxPro software (Mx3000P v3.20 Build 340, Schema 74), in order to ensure that the PCR reaction was only producing a single template, without any other non-specific targets being amplified. The relative transcript abundance of each target gene was compared to the mouse 18S transcript, the $\log_2$ fold change (L2FC) was acquired using the ΔCT method and the significance quantification was verified with a one-way ANOVA comparing the means of each treatment group (WT, Het and EcKO). When only comparing the

mean fold change and SEM of two samples, WT and EcKO mice (Appendix Figures 44 – 45), a parametric, unpaired t-test was performed to test for significant change, $\alpha < 0.05$.

Table 3 **qPCR reaction mix.**
Table depicting the amount added and the final concentration of solutions to formulate a single qPCR reaction.

Solution	volume	Final Concentration
cDNA 1:10	2 µL	
2X SensiFast SYBR (Bioline LoROX kit)	10 µL	1X
10 µM Forward Primer	0.8 µL	2.5 µM
10 µM Reverse Primer	0.8 µL	2.5 µM
Hplc H_2O	6.4 µL	
Total per reaction	20 µL	

2.4.3. RNA-sequencing data processing and analysis

The PureLink RNA Mini Kit (Thermo Fisher Scientific) was used for RNA purification following the manufacturer's instructions, after the RNA isolation step described in 2.4.1, in order to ensure highest RNA quality from all samples. 4 WT and 4 EcKO P0 forebrain specific RNA samples were sent for sequencing to GenomeQuébec (Montréal). The average concentration of the RNA sent for sequencing was ~44.5 ng/µL with a standard deviation of +/- 3.9, with a total of 250 ng of RNA per each sample sent for processing. GenomeQuébec prepared stranded mRNA libraries using NEBNext dual adapters (NEBNext multiplex oligos for Illumina [Dual index primers set 1]) providing an average library size of 342 bp. Subsequently, they used the Illumina NovaSeq 6000 to provide pair-end sequences of 100 bp long, with and high quality

Phred score of 36 and, an average of 78,045,781 sequenced reads provided per sample. FastQC (101) and trimmomatic (102) were used on all .fastq files to ensure the highest quality reads were used for downstream analysis. Reads were mapped to the GRCm38 mouse genome using Hisat2 (103), the mapped reads were then used to perform the IGV sashimi plot analysis, followed by exon specific quantification using ExCluster (128). For the differential expression analysis, Kallisto (104) was used to pseudoalign the reads to the GRCm38 mouse transcriptome and simultaneously quantify the reads mapped to each gene. Differential expression analysis as well as the corresponding data quality checks (PCA, Standard deviation analysis and heatmap of segregation) were performed in R using the DESeq2 (105) package, identifying differentially expressed genes (DEGs) with a L2FC of +/- 0.5 and using a significance threshold s-val < 0.005 (Appendix Tables 9 – 10). The s-val significance threshold is an analogous system to the q-value (adjusted p-val), argued to be better at distinguishing false positives (106). Following the differential expression analysis, we performed Gene Ontology analysis of the DEGs, separating upregulated and downregulated transcripts, using g:profiler (107). Furthermore, another R package was used, called DOSE (108), to perform the disease ontology of the DEGs, separating the down from the upregulated genes as well. The DOSE R package identifies human related diseases from human genes. Considering we are using the mouse as a model, the transcripts of interest were then converted to their corresponding human ortholog genes, that set of human ortholog genes was the list of genes used as the input for the DOSE package. Therefore, DOSE identified the disease related genes, from our list of human orthologs acquired from the mouse DEGs

3. Results

3.1 *Bptf* conditional Knockouts – *Nestin* Cre

3.1.1 Mouse Viability

Smarca5$^{f/-}$ conditional knockout (*Smarca5* cKOs) mice, using *Nestin* to drive Cre expression has previously yielded viable pups at normal Mendelian ratios (80). Considering the interaction between Snf2h and Bptf (66), we bred *Bptf*$^{f/f}$ mice to the *Nestin*-Cre driver mice for the initial characterisation of *Bptf* cKO animals to serve as a murine model of the NEDDFL syndrome. *Bptf*$^{f/f}$ mice contain loxp sites flanking exon 2 of the *Bptf* gene (88). Following Cre excision, *Bptf* transcripts are out of frame and behave as LoF null alleles (88). *Nestin* gene expression starts at E7.5 and it is fully expressed in the entire CNS of the mouse embryo by E14.5 (97). The Cre transgene, including a CNS-specific enhancer, was introduced in the 5' region of the *Nestin* gene, in between the promoter and the transcriptional start site (TSS) (97, 98). Presumably, by generating *Bptf*$^{f/f}$ :: *Nestin* Cre$^{+/-}$ mice (here on, NcKO), we have eradicated the functional Bptf protein in the entire CNS of the developing mouse (Figure 6). When analysing P0 litters produced from *Bptf* $^{f/f}$ females and *Bptf* $^{f/+}$ :: *Nestin*Cre $^{+/-}$ males (as described in section 2.1.2), we noticed the NcKO mice were either born dead or died shortly after birth (Figure 7). The observed ratios of the post-natal mice (6 litters) do not correspond to the expected Mendelian ratios (25% Heterozygote, 25% NcKO, and 50% Wild-type), displaying a higher Heterozygote percentage (Het, 53.8%) as well as a lower NcKO (7.7%) and Wild-type ratio (WT, 38.5%). Most likely, the altered Het and WT ratios arise as result of a low sample size (Table 4).

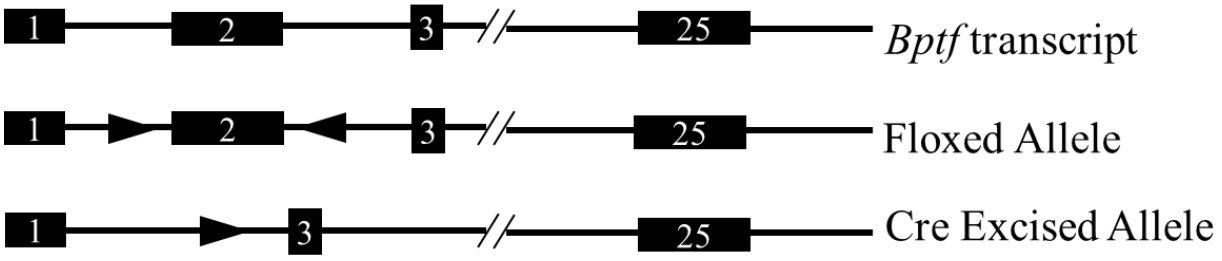

Figure 6 ***Bptf* unaltered, floxed and excised allele.**
Schematic displaying the location of the loxp sites within the floxed *Bptf* allele and the expected outcome of the exon 2 excision, compared to the normal *Bptf* transcript. – adapted from Landry et al. (88).

Figure 7 **Wild-Type, heterozygote and NcKO littermates at P0**.
Highlighting death at birth only observed in the NcKO animals. One litter representative of the observed litters annotated in Table 2.

Table 4 **Counts of all observed post-natal *Nestin*-Cre pups.**
Table displaying the expected and actual mendelian ratios as well as the observed survival of each corresponding genotype. Parental genotypes: female *Bptf* $^{f/f}$ x male *Bptf* $^{f/+}$ :: *Nestin*-Cre $^{+/-}$.

Postnatal – P0

Genotype	# of animals	Expected Mendelian ratio	Actual
NcKO	2	25 %	7.7 %
Het	14	25 %	53.8 %
Wild-Type	10	50 %	38.5 %
Total	26		
Litters	6		

Given that the NcKO animals were dying at birth, it was decided to examine the state of embryonic animals. From five litters, we observed 22.2% NcKO, 33.3% Het and 44.4% WT embryos when isolated at E13.5 and E18.5, which was closer to the expected Mendelian ratios (Table 5). To gain some understanding of the early post-partum death, we decided to analyze brain morphology of the NcKO animals. In this way, fetal E18.5 brains from two pregnant dams were collected, sectioned and stained with Nissl (Figure 8). Although the differences were not quantified, it appeared the brain of the NcKO mice is considerably reduced in size. Solely from visual analysis, the cortex seems smaller, the structure of the hippocampus looks altered, the midbrain thinner and, the cerebellum is not forming the structural lobes as its wild-type littermate. Based on the lack of viable pups, it was decided that using the *Emx1*-Cre driver line to generate *Bptf* cKO mice, in which Cre expression is restricted to the developing forebrain, as a more suitable model. This model may result in live born pups, allowing us to holistically analyze the role of *Bptf* during neurogenesis.

Table 5 **Counts of all observed prenatal *Nestin*-Cre pups.**
Table displaying the expected and actual mendelian ratios as well as the observed survival of each corresponding genotype. Parental genotypes: female *Bptf* $^{f/f}$ x male *Bptf* $^{f/+}$ :: *Nestin*-Cre $^{+/-}$.

Prenatal – E13.5 & E18.5

Genotype	# of animals	Expected Mendelian ratio	Actual	Survival
NcKO	10	25 %	22.2 %	All alive
Het	15	25 %	33.3 %	All alive
Wild-Type	20	50 %	44.4 %	All alive
Total	45			
Litters	5			

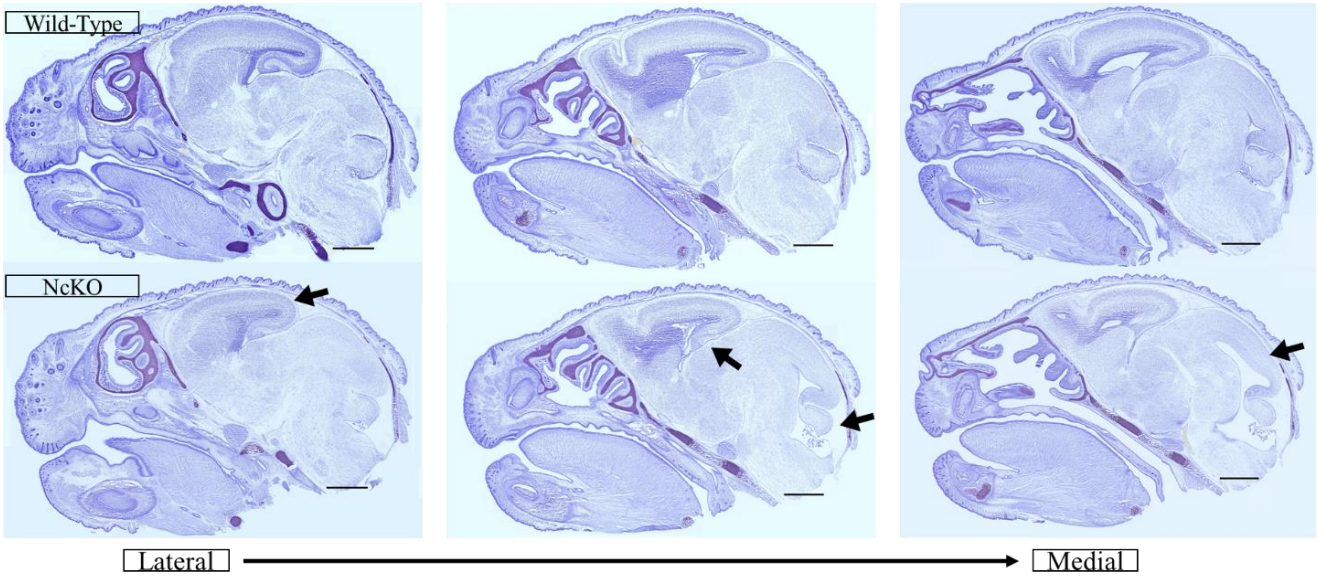

Figure 8 **Brain anatomy of WT and NcKO E18.5 littermates.**
Representative nissl stained sagittal sections (n = 1) of animals observed. Wild-type compared against *Bptf* NcKO E18.5 animals moving from lateral to medial sections. Arrows pointing to the most noticeable size differences between NcKO and WT littermate (scale bar = 1mm).

3.2 *Bptf* conditional Knockouts – *Emx1* Cre

3.2.1 Mouse viability

To examine the consequences of excising *Bptf* from the developing neocortex, we utilized an *Emx1*-Cre driver line. *Emx1* is a transcription factor expressed in the progenitor cells and the postmitotic neurons of the developing murine telencephalon (99). Its expression is first noted at E10.5 and, by E12.5 almost every progenitor and neuron of the pallia expresses *Emx1* (99). The IRES (internal ribosome entry site) and Cre coding locus were introduced between the last exon and the 3'-UTR (untranslated region), thus ensuring Cre expression without altering *Emx1* levels (99). In this way, $Bptf^{f/f}$ :: *Emx1*-Cre mice (here on, EcKO) were created to examine the function of *Bptf* in the developing murine forebrain. Overall, we collected a total of 305 mice, 141 were WT (46.2 %), 82 Het (26.8 %) and 82 EcKO (26.8 %) which is consistent with the expected Mendelian ratios of 50%, 25% and 25%, respectively. Forty-five EcKO mice were also sexed, which suggested no difference in birth rates between males (42.3%) and females (57.7%), around a 50/50 ratio (Table 6). Lastly, to examine the survival of the EcKO animals, 6 pups from the same litter [2 EcKO (one male and one female) and 4 WTs (2 males and 2 females)] were allowed to develop, weaned accordingly, and then sacrificed at 9 months of age. Both EcKO mice survived with their WT littermates until they were sacrificed (Figure 9). Given that the *Bptf* EcKO mice were born in normal Mendelian ratios and showed normal survival we concluded that they would be a appropriate model to analyze the requirement for *Bptf* in the developing neocortex. Hereon, EcKO mice were compared to their Het and WT littermates in all ensuing experiments of this thesis.

Table 6 **Total *Bptf::Emx1*-Cre mice used.**
All pups are the result of, female *Bptf* $^{f/f}$ x male *Bptf* $^{f/+}$ :: *Emx1*-Cre $^{+/-}$. Table displaying the actual and the expected mendelian ratios, the survival of such mice, and the PCR-determined (SRY gene) sexual identity of 45 EcKO pups.

All *Bptf::Emx1*-Cre animals

Genotype	# of animals	Expected Mendelian ratio	Actual	Survival	45 sexed EcKO mice	
					Male ♂	Female ♀
EcKO	82	25 %	26.8 %	All alive	19 – 42.3%	26 – 57.7%
Het	82	25 %	26.8%	All alive		
Wild-Type	141	50 %	46.2 %	All alive		
Total	305					
Litters	38					

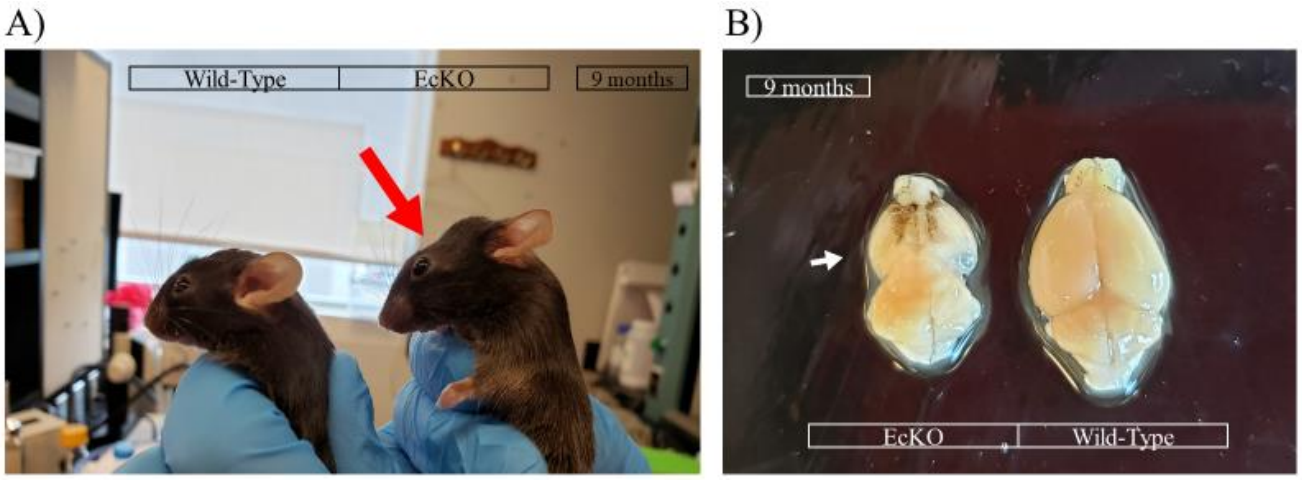

Figure 9 **Survival of adult EcKO mice.**
A) Adult comparison of 9-month old WT and EcKO littermates. Red arrow highlights microcephalic feature only observed in the EcKO. B) Dissected brains of mice in A). White arrow pointing to the dramatic cortical hypoplasia observed in the EcKO brain.

Initial basic physiological comparison demonstrated that the EcKO model, at birth (P0), had a mean body weight of 1.36 g +/- 0.05 (n = 10) that was not statistically different from WT mice (1.37g +/- 0.03; n = 10; p-val = 0.87; unpaired t-test). However, the brains did show a significant decrease in weight (WT: 0.09g +/- 0.0015; EcKO: 0.079g +/- 0.0037; n = 10; p-val = 0.0051; unpaired t-test) that resulted in a difference in the brain/body weight ratio (WT: 0.068 +/- 0.0018; EcKO: 0.057 +/- 0.0033; p-val = 0.0085; unpaired t-test[Figure 10]). However, from the continued evaluation of the EcKO and WT weights, it is evident that the EcKO animals were not gaining weight in the same rate as the WT counterparts. By P2, EcKO weighted 1.39 g +/- 0.026, while the WT counterparts weighted 1.66 g +/- 0.037 (n = 7; p-val < 0.0001; unpaired t-test; Figure 10D). By P10, (Figure 11) a microcephalic phenotype becomes evident, which is visualized by the reduced *Bptf* EcKO cortex observed from dissected P12 brains (Figure 12). Cortical hypoplasia is noticeable beginning at E15.5 (Figure 13) but it is clearly evident by P2 (Figure 14). However, the most dramatic cortical comparison is displayed by the adult mice (9-mo old), where it is evident the cortex of the EcKO mice is extremely reduced in comparison (Figure 15). Of interest, the normal hippocampal structure is not clearly seen in early post-natal mice nor in the adult EcKO brain.

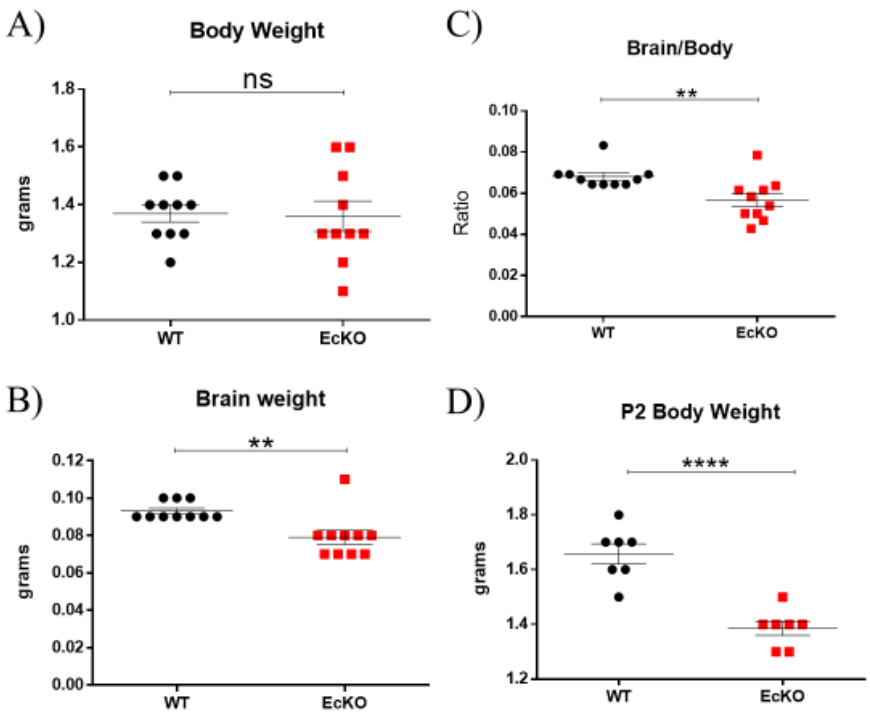

Figure 10 **Brain of EcKO mice is smaller since birth.**
A-C) P0 WT and EcKO littermate comparisons. A) Body weight (grams, n = 10, p-val = 0.8702). B) Brain weight (grams, n = 10, p-val = 0.0051). C) Brain/Body weight ratios (n = 10, p-val = 0.0085). D) Body weight comparison of WT and EcKO pups at P2 (n = 7, p-val <0.0001). ns = no significant change, **** = p-val < 0.0001, ** = p-val < 0.01, * = p-val < 0.05, unpaired t-test on all.

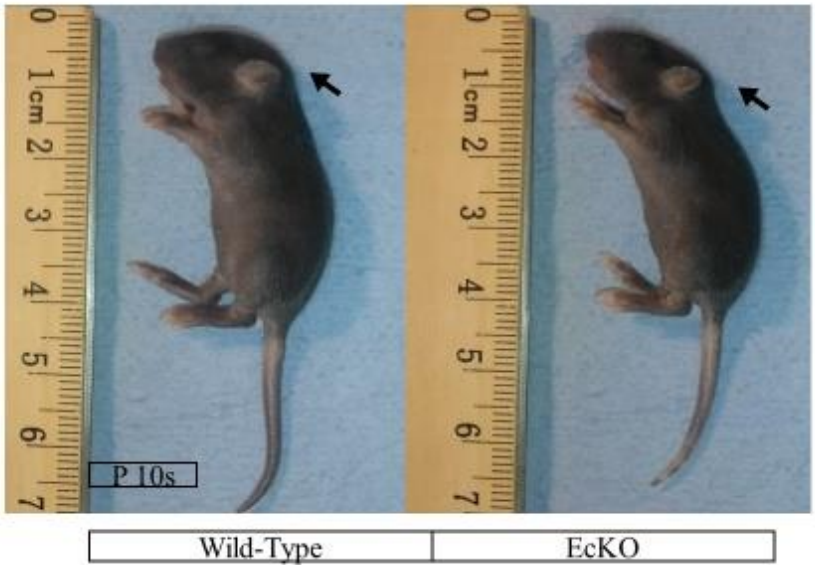

Figure 11 **EcKO mice display microcephalic features by P10.**
Full body comparison of Wild-Type and EcKO animals at P10, representative image of animals observed. Black arrows highlighting slanted head of EcKO vs round head of the WT littermate.

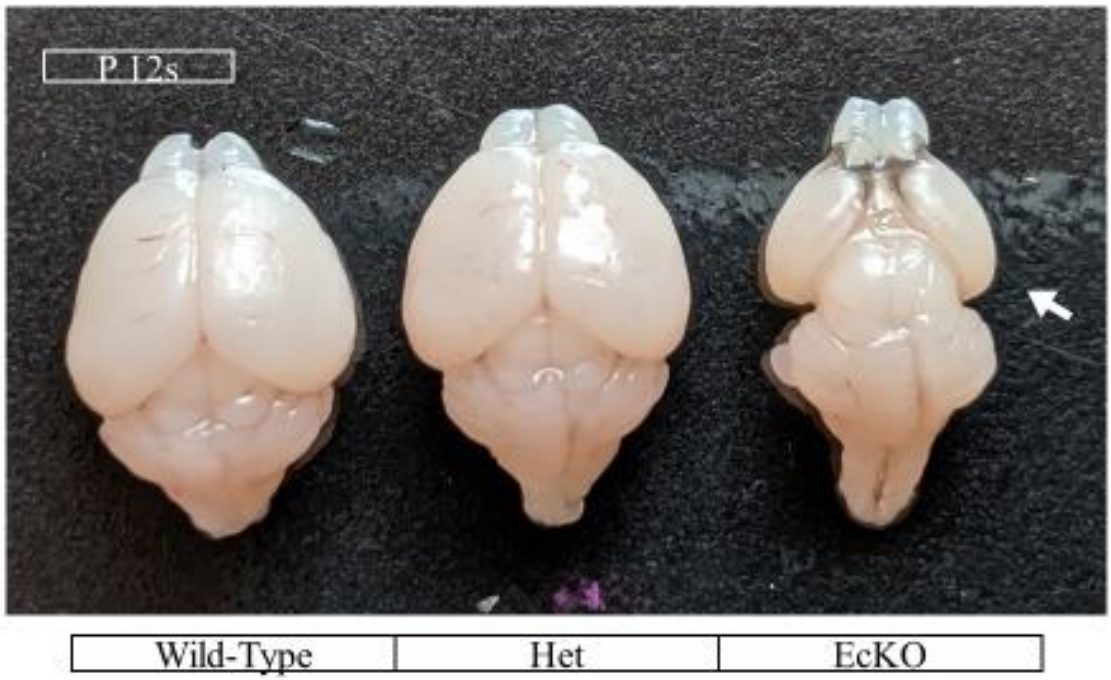

Figure 12 **Bptf removal leads to a smaller neocortex.**
Dissected full brains from P12 animals, representative image of phenotype observed across all mice analyzed. Noting (white arrow) the highly reduced neocortex of EcKO animals, not observed in WT or Het littermates.

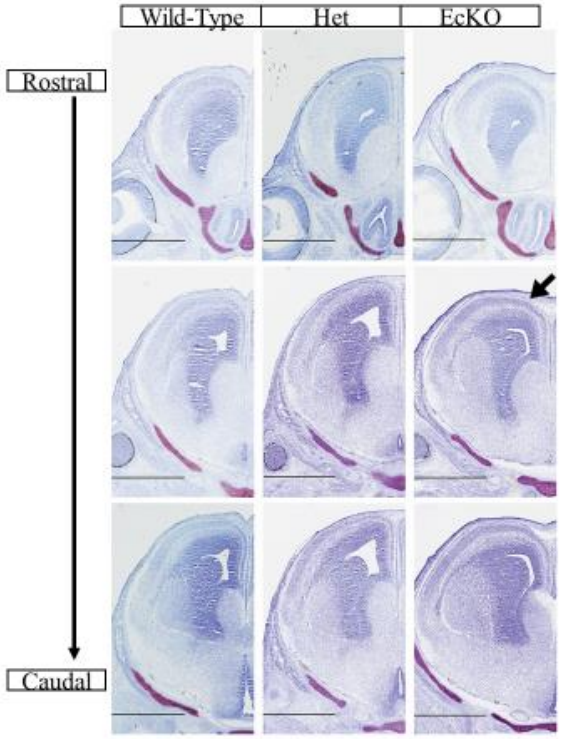

Figure 13 **Cortical reduction at E15.5.**
Nissl stained E15.5 coronal head sections, representative images of animals observed (scale bar = 1mm). Wild-type aligned with Het and EcKO sections (n = 1) moving from rostral (top) to caudal (bottom). Arrow pointing to the most noticeable EcKO cortical reduction when compared to WT and Het animals

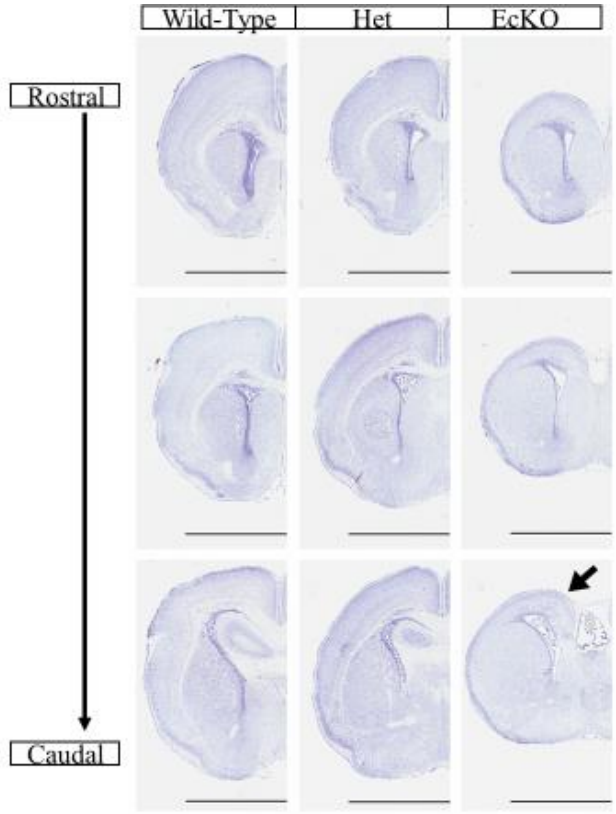

Figure 14 **Evident cortical reduction at P2.**
Nissl stained P2 coronal brain sections, representative images of animals observed (scale bar = 2mm). WT aligned with Het and EcKO sections (n = 1), moving from rostral (top) to caudal (bottom). Black arrow pointing to the most noticeable cortical size difference of EcKO when compared to WT and Het.

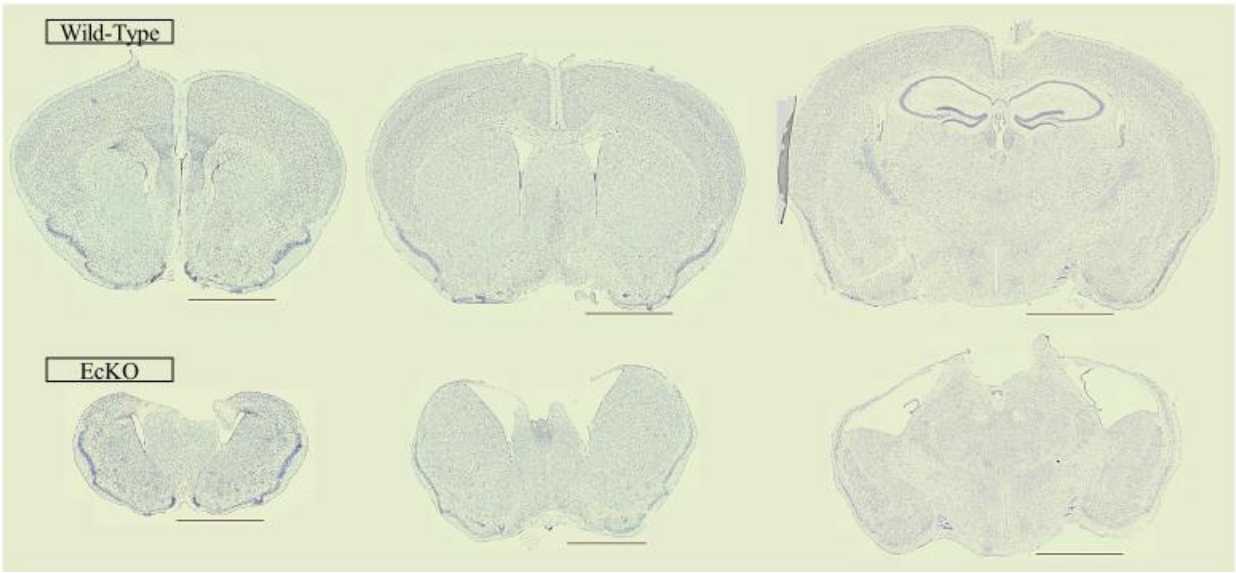

Figure 15 **Dramatic cortical near disappearance at 9 months of age.**
Nissl stained 9-month old coronal brain sections (scale bar = 2mm). Wild-Type aligned with EcKO brains (n = 1) moving from rostral (left) to caudal sections (right).

3.2.2 *Bptf* Excision

To confirm that we were observing extensive excision of exon 2 of the *Bptf* gene in the EcKO mice, we performed western blot and RT-PCR experiments. First, multiple commercial antibodies against Bptf were tested on whole protein lysates as well as in nuclear extracts specifically from cortical tissue. Unfortunately, the antibodies (Appendix Table 8) used did not recognize a protein of the correct size in WT extracts, nor were there any differences observed between WT or EcKO samples, indicating that the antibodies were non-specific and could not be used (data not shown). Next, we isolated RNA from WT, Het and EcKO dissected cortices at E15.5 and reverse transcribed cDNA to test for excision of exon 2 by RT-PCR. The *Bptf*$^{f/f}$ mice produced by Landry et al. (88) contain loxp sites flanking exon 2, resulting in an 823 bp Cre-excised section of the *Bptf* transcript. First, we designed primers complementary to exons 1 and 3 (Figure 16B), that would give rise to an expected amplified product of 929 bp in WT mice and 106 bp in EcKO mice. The electrophoresis of the cDNA PCR products demonstrated that WT samples had a single amplified product of slightly less than 1,000 bp while the EcKO samples had a band of around 100 bp and did not show any trace of the 929 bp band. As expected, the Het PCR products contained both bands (Figure 16A). Second, we designed a probe complementary to exon 2 of the *Bptf* transcript, for an *in-situ* hybridization experiment. The RNA probes were synthesized to contain DIG-dUTPs which, were then used to stain with an αDIG-AP enzyme to catalyze the colour reaction. We then probed for *Bptf* exon 2 in WT, Het and EcKO (n = 1) brain sections at E15.5. All slides were stained together to limit any differences that can be incurred from the staining procedure so that alterations in expression could be compared[2]. Both the WT and Het sections demonstrate expression of *Bptf's* exon 2 in the cortex as well as in the midbrain,

[2] Staining of brain sections for the *in-situ* hybridization experiment was performed by Senior Lab. Technician, Keqin Yan M.Sc. (Dr. Picketts' lab).

demonstrating similar staining throughout the brain (Figure 17). In contrast, there seems to be very low staining of the EcKO cortex compared to WT or Het cortex while staining of the EcKO midbrain region was comparable to the control samples.

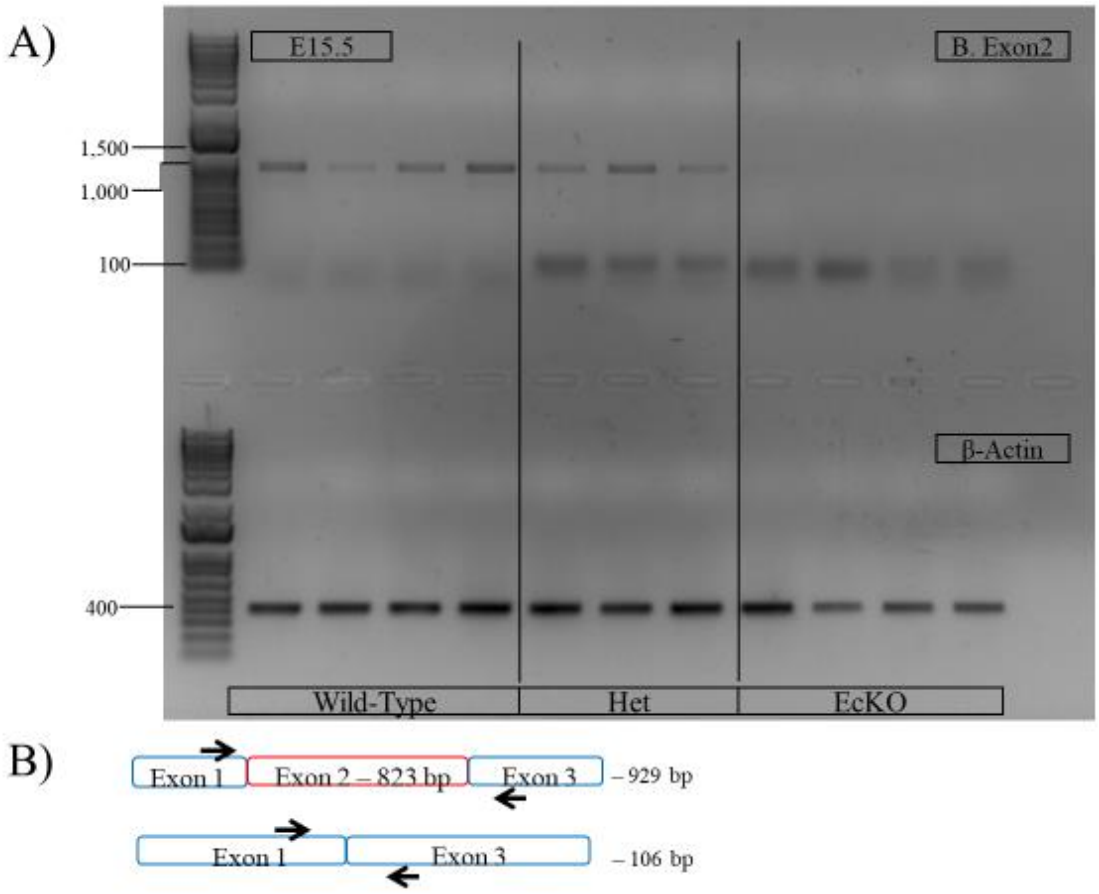

Figure 16 **Excision of *Bptf* exon 2.**
A) RT-PCR experiment, using E15.5 forebrain specific tissue from WT, Het and EcKO embryos. Top section of gel shows the *Bptf* exon 2 bands, while the bottom section shows the *β-actin* loading control, corresponding to each sample. The top section of the gel shows the two expected bands: 929 bp and 106 bp (shown in B). B) schematic of the primer location used to flank exon 2, binding to the end of exon 1 and the beginning of exon 3 of the *Bptf* transcript. Highlighting on the right the fragment size (bp) of each expected band.

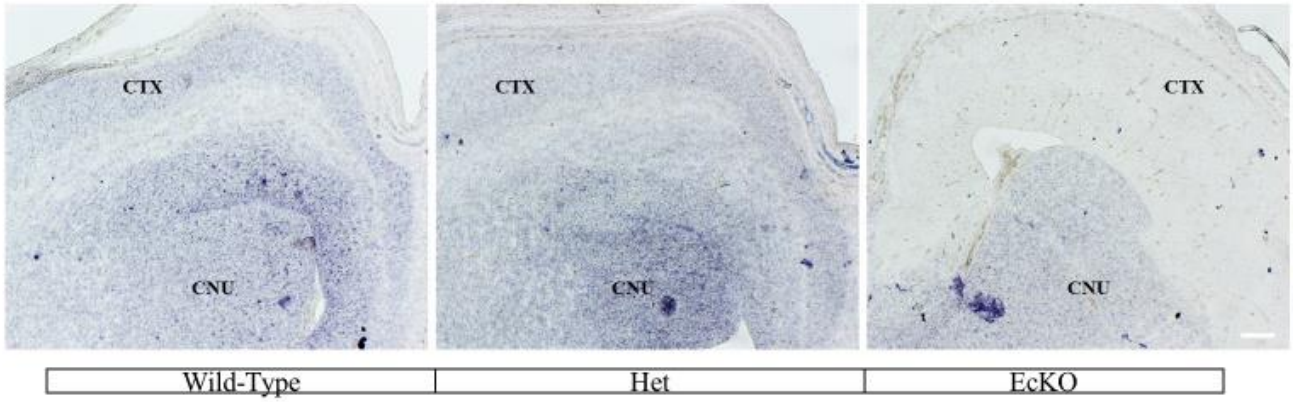

Figure 17 **Exon 2 is not present in EcKO cortex**.
In-situ hybridization experiment on brain coronal sections of WT, Het and EcKO E15.5 embryos (n = 1). Probe is complementary to exon 2 of the *Bptf* transcript. Highlighting the reduction in staining specifically in the cortex but not in the midbrain of the EcKO sections as well as, when compared to the cortex of the WT and Het. CTX = cortex, CNU = cerebral nuclei (also known as midbrain), scale bar = 100 µm.

As a complementary approach, exon-specific RNA-seq reads of the *Bptf* transcript from EcKO forebrain samples (at P0) were normalized to the full transcript and quantified against the corresponding WT exon read counts (128). Figure 18 shows that the EcKO samples contain half the number of exon 2 reads (log2FC = -1), while the remainder of the exons are not significantly reduced (FDR ~ 0.002). Sashimi plots (Figure 19) corroborated the decrease in reads mapped to exon 2 and, demonstrates that mapped reads from the EcKO samples skipped exon 2. This skipping of exon two is not observed in the WT samples. All together, the RT-PCR, the *in-situ* hybridization experiment and the exon-specific quantified RNA-seq reads corroborate the expected Cre-mediated excision of exon 2 (of the *Bptf* gene) specifically in the forebrain of the EcKO mice and Het littermates.

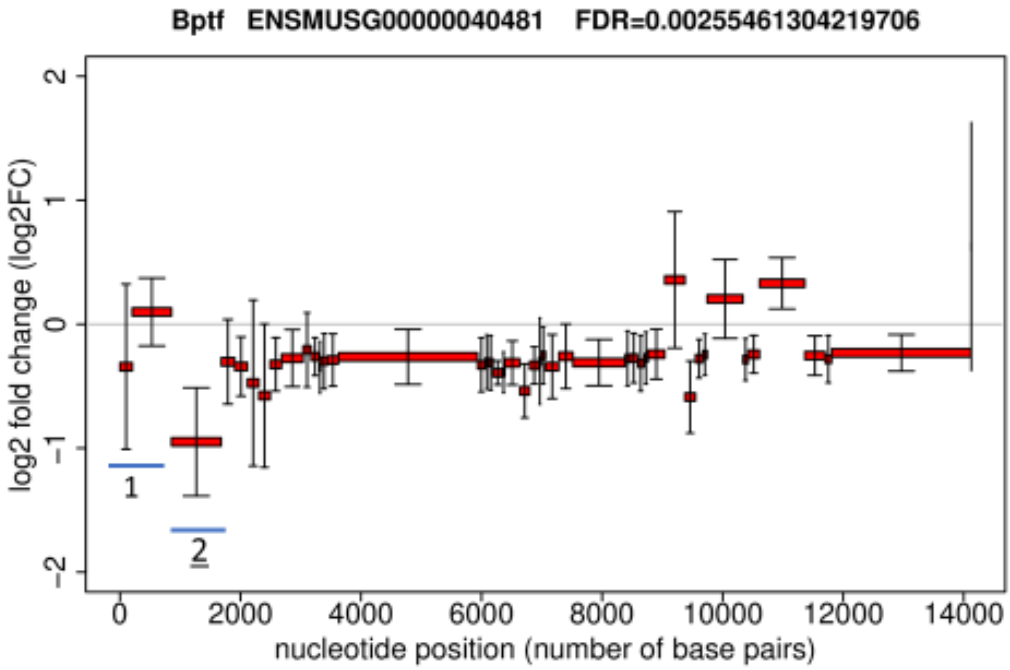

Figure 18 **Significant reduction of *Bptf* exon 2.**
ExCluster software generated image, demonstrating a $\log_2$ fold = -1 reduction (FDR = 0.0025) of exon 2 in the *Bptf* transcript, when compared to that of the WT. 5'-UTRs and exon 1 of a full transcript are binned by the software into two groups to ensure no read overlap with other possible genes. Therefore, blue line 1 → underlines exon 1 and the 5' UTR of the *Bptf* transcript, blue line 2 → underlines exon 2.

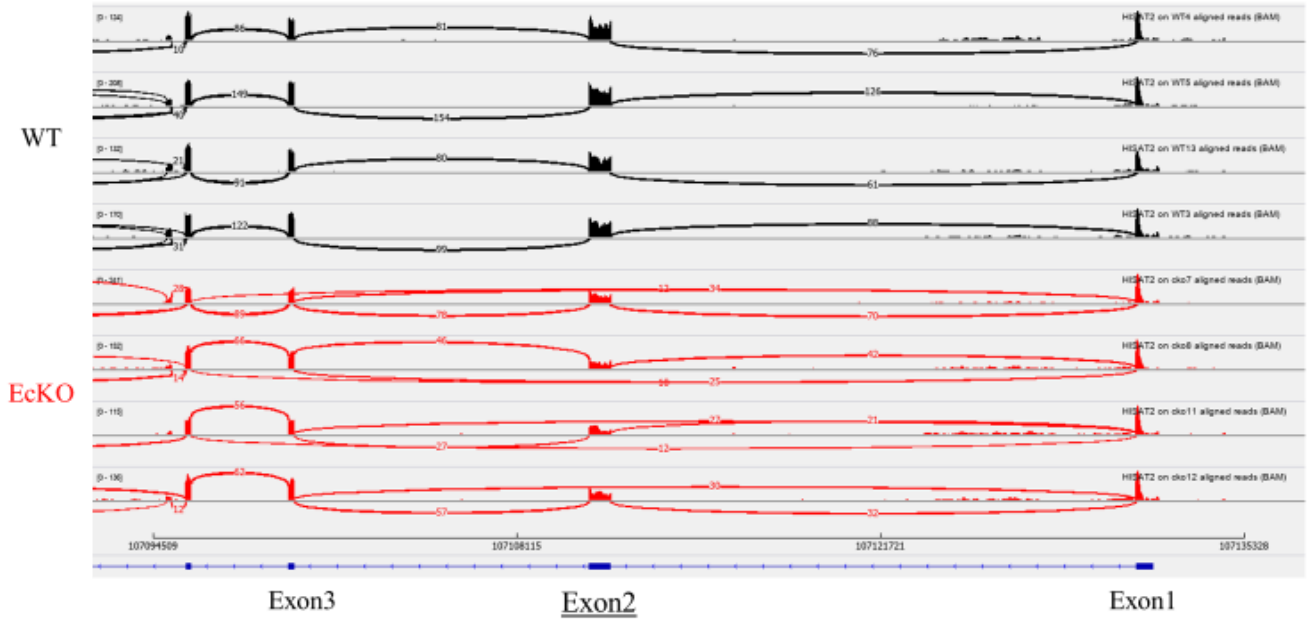

Figure 19 **Exon 2 is skipped in half of the EcKO *Bptf* transcripts.**
Sashimi plot of mapped WT and EcKO (n = 4) RNA-seq reads, from P0 forebrain tissue. Image highlighting the *Bptf* region from exon 1-4 (right to left), the reads mapped to each exon and, reads mapped in two exons are displayed by a bridge line. Demonstrating EcKO reads map to exons 1 and 3 (or 4), which are not observed in the WT reads. Supporting Cre's excision of exon 2.

3.2.3 Decreased cortical intermediate neuronal progenitor cells in EcKO embryos

The reduction in cortical size of the *Bptf* EcKO mice suggests a specific role for Bptf in neocortical progenitor pool proliferation and/or differentiation. To examine the nature of the specific cortical defect we performed various immunofluorescent (IF) staining procedures to analyse the state of progenitor cells in the EcKO cortex. First, pregnant females were injected with a thymidine analog, EdU, in order to label cells which are entering S-phase at the time of injection. We injected the pregnant dams when the pups were at E15.5 and the pups were then collected 1-hour following injection. Pax6 is a key TF used as a marker for neuronal progenitors, RGCs which have started neuronal production. With an αPax6 antibody and detection against EdU, we quantified the proportion of proliferating RGCs, relative to the total number of cells stained with Hoechst (DNA dye). Figure 20 demonstrates that there is no change in the proportion of RGCs (WT: 31.59%; Het: 33.51%: EcKO: 32.41%), Pax6 + / Hoechst + (H+) between WT, Het and EcKO sections (p-val = 0.394; n = 3; one-way ANOVA). Furthermore, there is no significant change in the proportion of replicating cells (WT: 15.55%; Het: 15.25%; EcKO: 13.38%; EdU + / H +; p-val = 0.106), nor in the proportions of co-labelled cells (WT: 30.48%; Het: 24.79%; EcKO: 28.15%; Pax6+ & EdU+ / Pax6+; p-val = 0.575).

Tbr2 is another key TF used as a marker of IPCs in active proliferation during neurogenesis. We stained for IPCs with an αTbr2 antibody also at E15.5 and followed the same EdU injection/detection protocol as above. Figure 21 shows a significant decrease in the proportion of IPCs (Tbr2 + / H+) when comparing that of the EcKO cortex (21.5%) to the Hets (28.7%) and to the WTs (25.9%; p-val = 0.0059; n = 3; one-way ANOVA). There was no decrease in the proportions of replicating cells (WT: 15.55%; Het: 15.25%; EcKO: 13.38%;

EdU+ / H+; p-val = 0.106) nor in the proportions of co-labelled cells, Tbr2+ & EdU+ / Tbr2+ (WT: 12.54%; Het: 9.23%; EcKO: 13.44%; p-val = 0.190).

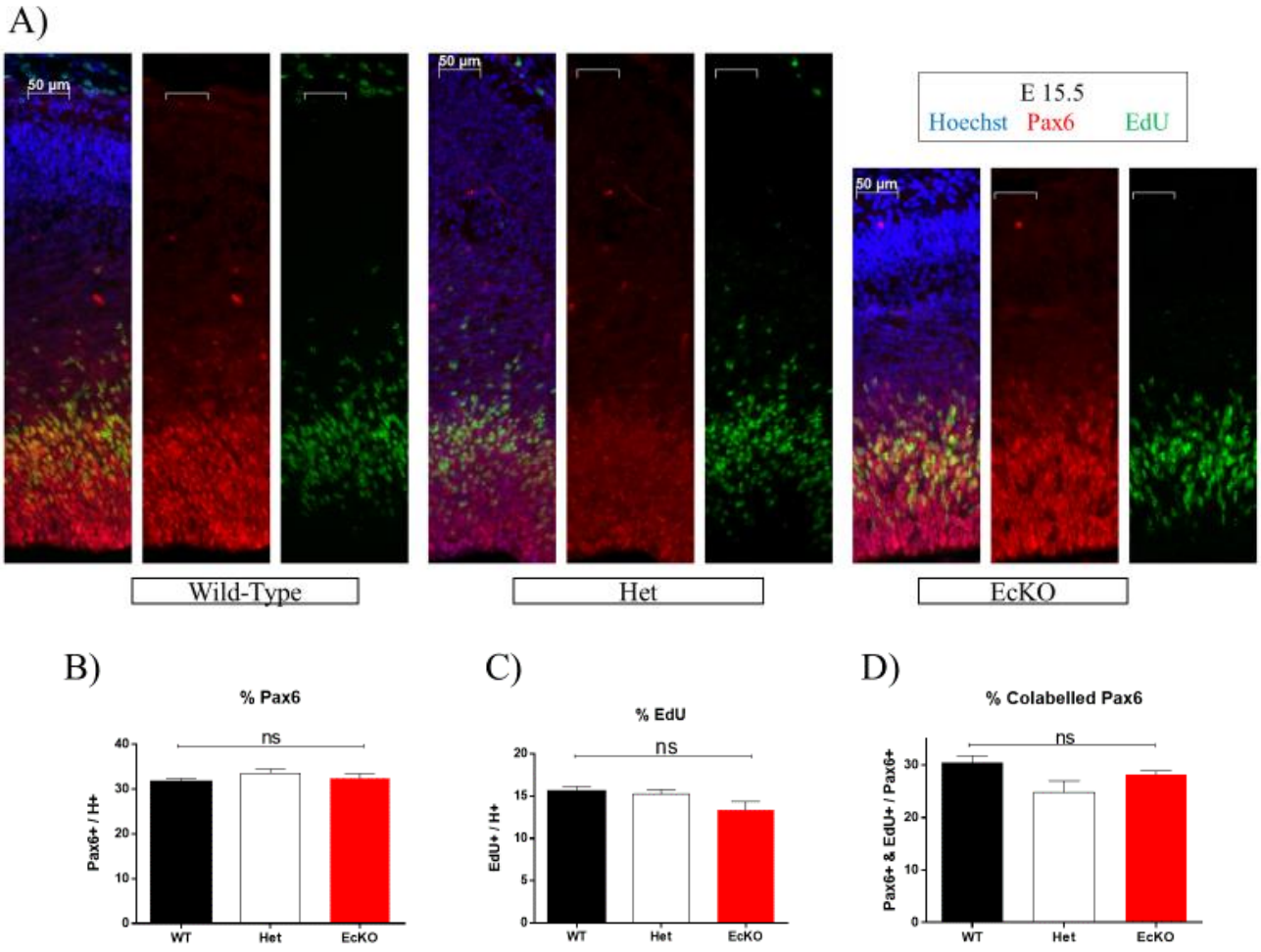

Figure 20 **Unchanged proportions of Radial Glial cells.**
A) Representative images of IF stained cortical sections of E15.5 WT, Het and EcKO samples (scale = 50 µm) stained for EdU (green), Pax6 (red) and Hoechst (blue). B) Quantification of Pax6 + / Hoechst + cells comparing WT, Het and EcKO (p-val = 0.394). C) Quantification of EdU + / Hoechst + cells comparing WT, Het and EcKO (p-val = 0.106). D) Quantification of Pax6 + & EdU+ / Pax6 + cells comparing WT, Het and EcKO (p-val = 0.0575). B-D) Significance testing was performed using one-way ANOVA, comparing the means of each treatment group (n = 3).

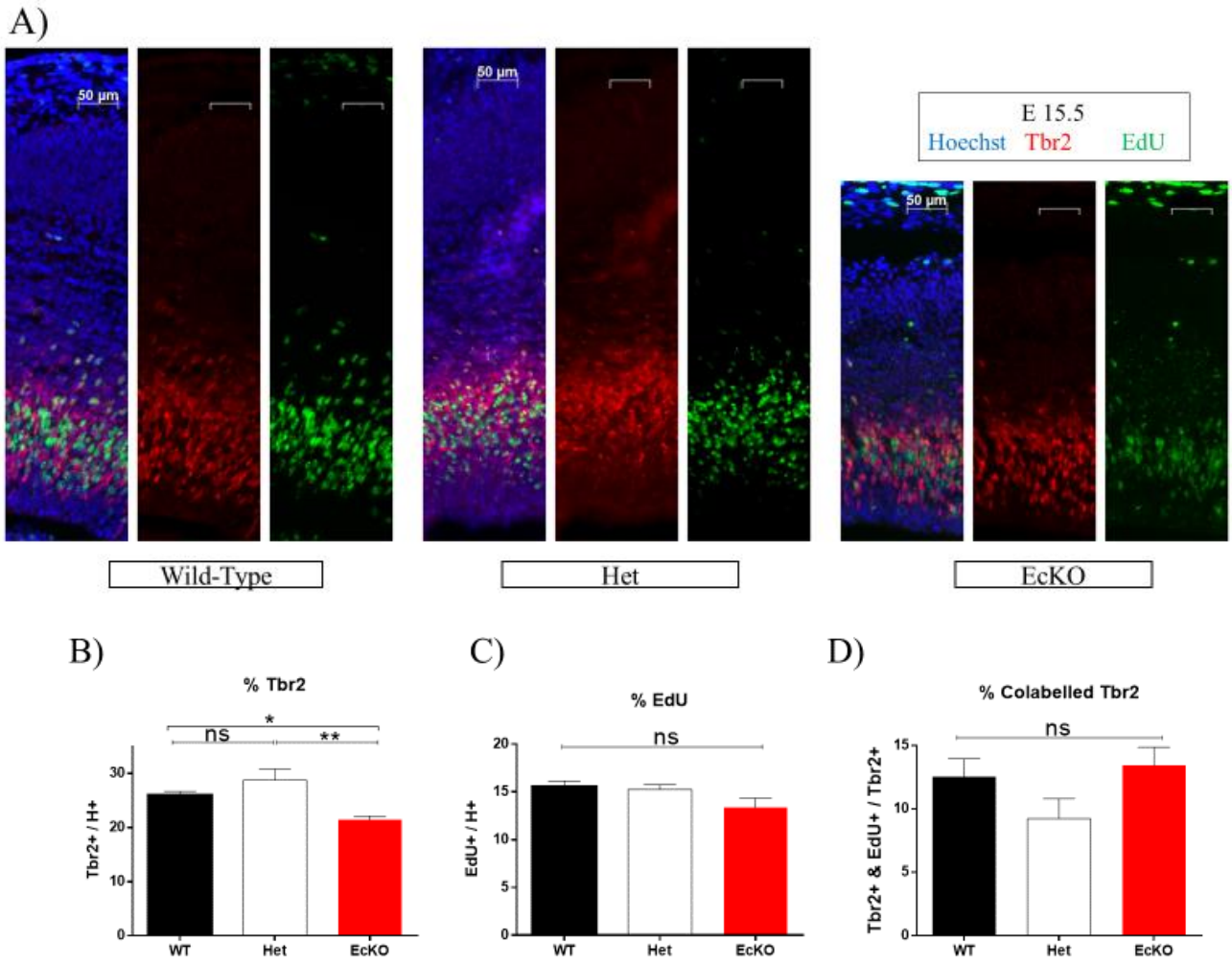

Figure 21 **Lowered proportions of Intermediate neuronal Progenitor Cells.**
A) Representative images of IF stained cortical sections of E15.5 WT, Het and EcKO samples (scale = 50 µm), EdU (green), Tbr2 (red) and Hoechst (blue). B) Quantification of Tbr2 + / Hoechst + cells comparing WT, Het and EcKO (p-val = 0.0059). C) Quantification of EdU + / Hoechst + cells comparing WT, Het and EcKO (p-val = 0.106). D) Quantification of co-labelled, Tbr2 + & EdU+ / Tbr2 + cells comparing WT, Het and EcKO (p-val = 0.190). B-D) Significance testing was performed using one-way ANOVA, comparing the means of each treatment group (n = 3, **** = p-val < 0.0001, *** = p-val < 0.001, ** = p-val < 0.01, * = p-val < 0.05).

Next, we wanted to analyse the proportion of progenitor cells that entered mitosis. We stained for phospho-histone H3 (pH3), a marker of M-phase mitotic cells (109), also at E15.5. From Figure 22, it is clear there was no proportional change in the percentage of pH3 stained cells in the apical region (ventricular zone) of the cortex (WT: 11.5; Het: 10.93; EcKO: 9.54; p-val = 0.101; n = 3; one-way ANOVA), nor in the basal region (sub-ventricular zone) when comparing WT, Het and EcKO (WT: 4.43; Het: 3.73; EcKO: 3.5; p-val = 0.356; n = 3; one-way ANOVA). Both progenitor cells, IPCs and RGCs, demonstrated similar proportions of cells in S-phase and in M-phase.

In order to determine if the progenitor cell population had decreased proliferation capabilities, we compared the fraction of progenitor cells that complete the cell cycle after a 24-hr period. We performed an EdU/Ki67 double labeling assay in which we injected EdU to a pregnant female at E14.5 and collected the pups for sectioning, 24-hrs later. In this experiment, the EdU-pulse labelled cells which entered S-phase 24-hours prior to harvesting and, the αKi67 antibody (observed in G1, S, G2, M and not in G0) stained cycling cells. Therefore, the proportion of double positive (EdU + & Ki67 + / EdU +) cells represent those which remained in cell cycle, while the fraction of cells positive only for EdU (EdU + & Ki67 - / EdU +) represent postmitotic cells. We quantified a decreased fraction of cells out of the cell cycle; WT and Het mean fraction of 79.8% and 79.3% (respectively) while EcKO had a mean fraction equal to 69% of post-mitotic neurons (p-val = 0.0151; n = 3; one-way ANOVA; Figure 23).

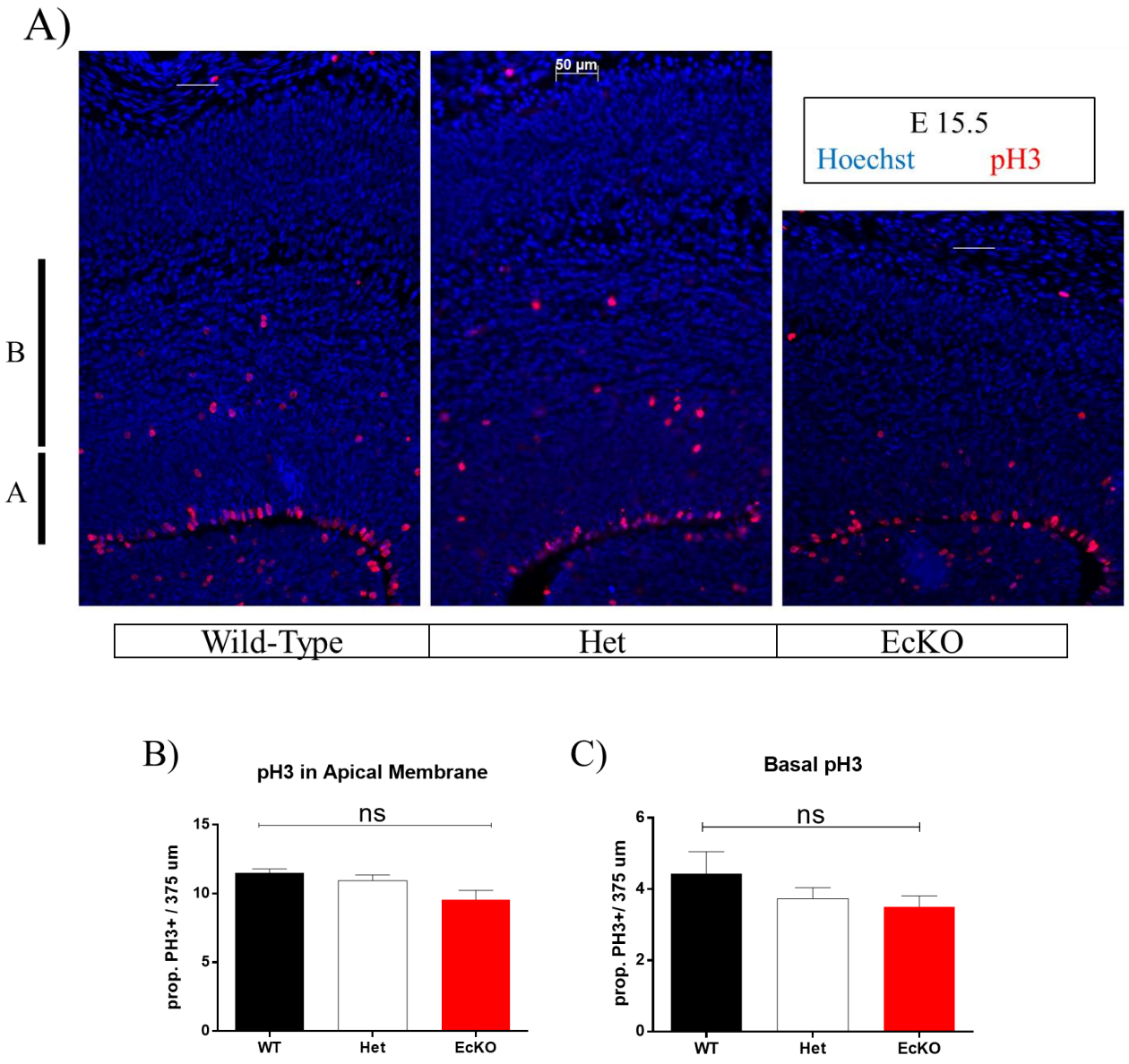

Figure 22 **No change in M-phase proliferating cells.**
A) Representative images of cortical sections of E15.5 WT, Het and EcKO samples (scale = 50 µm) IF stained for pH3 (red) and Hoechst (blue). A = Apical region, segment from the apical membrane of the cortex upwards until the end of the ventricular zone (RGCs); B = Basal region, from the end of VZ to the end of the SVZ (IPCs). These regions represent the manner in which the cortical sections were segregated for quantification. B) Quantification of pH3 positive neurons, in a rectangle 375 µm long and wide enough to cover the apical region. A rectangle of the same size was used on all samples. Demonstrating no significant change when comparing WT, Het and EcKO (n = 3, p-val = 0.101, one-way ANOVA, comparing the means of each treatment group). B) Quantification of pH3 positive neurons in a rectangle 375 um long and, covering from the end of the 'A' upwards to the start of the CP. Not the same length since EcKO cortex is smaller, but same width. Demonstrating no significant change when comparing WT, Het and EcKO (n = 3, p-val = 0.356, one-way ANOVA, comparing the means of each treatment group).

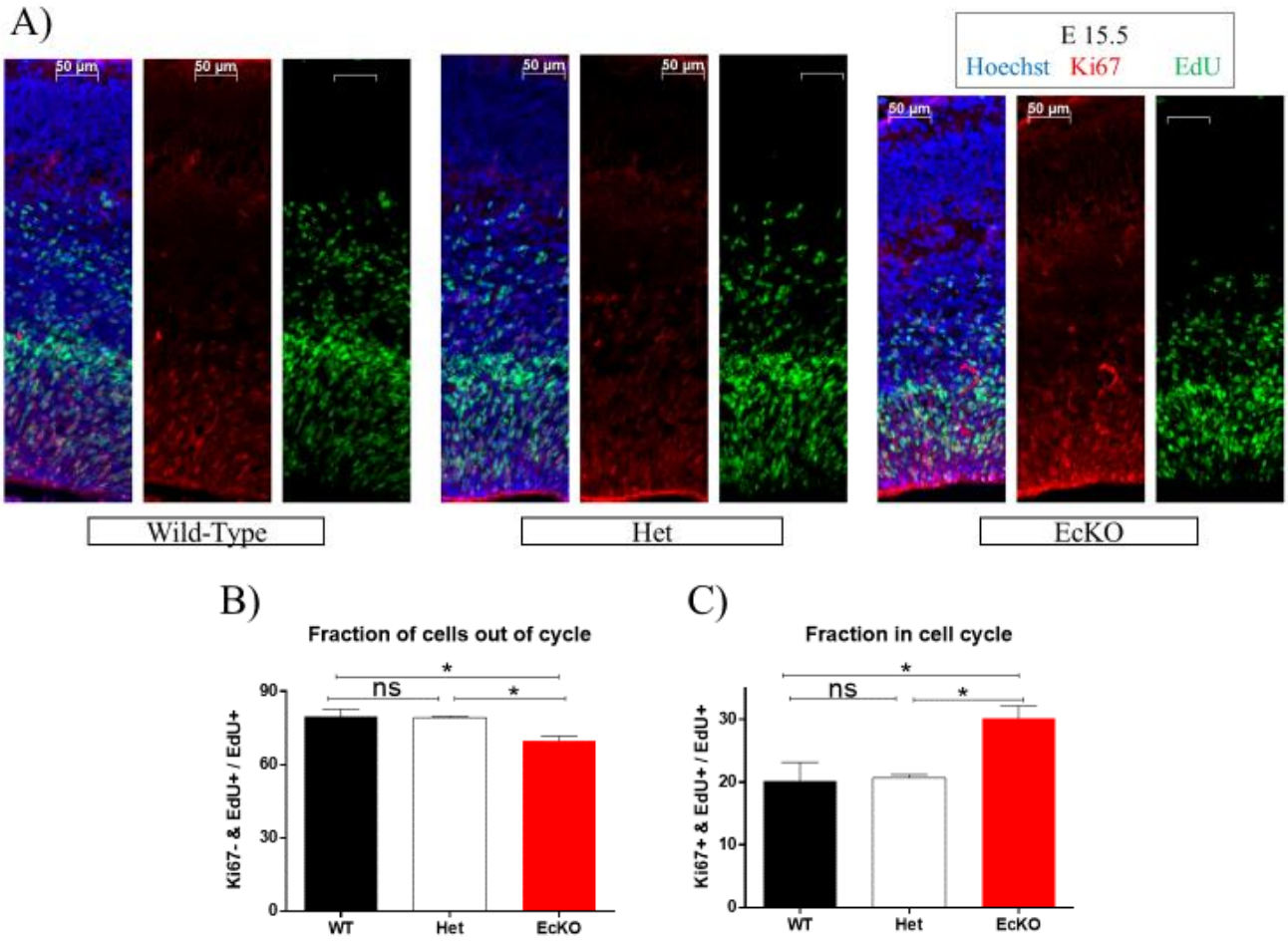

Figure 23 **Increased fraction of cells remaining in cell-cycle.**
A) Representative images of cortical sections of E15.5 WT, Het and EcKO samples (scale = 50 µm) IF stained for Ki67 (red), EdU (green) and Hoechst (blue). Pregnant females were injected with EdU 24hrs prior to pup dissection, followed by staining with αKi67 antibody (marker for cells within cell cycle) B) Quantification of cells which exited cell cycle within the 24hr period, (Ki67- & EdU+) / EdU+ (n = 3, p-val= 0.0151, one-way ANOVA). C) Quantification of cells which remained in cell cycle since EdU pulse, (Ki67+ & EdU+) / EdU+ (n = 3, p-val = 0.0151, one-way ANOVA, **** = p-val < 0.0001, *** = p-val < 0.001, ** = p-val < 0.01, * = p-val < 0.05).

3.2.4 Dramatic decrease of Layer V neurons in post-natal EcKO neocortex

The significant cortical hypoplasia and the lowered proportion of IPCs prompted us to perform layer marker studies to analyse the state of the post-natal neocortex within EcKO mice. We stained for early-born (αTbr1 and αCtip2) and late-born (αFoxp1 and αSatb2) neurons, on P2 brain coronal sections (Figures 24 – 25). It is important to note that there was a significant decrease in the total number of Hoechst + cells in the mutants (WT: 873.5 +/- 38.35 cells; Het: 953 +/- 9.35; EcKO: 653 +/-26.46; n = 4; p-val < 0.0001; one-way ANOVA). Second, there was no significant change in the proportion of Satb2 positively stained neurons that localize mainly in layers II/III (WT: 48.48%; Het: 50.54%; EcKO: 53.43; p-val = 0.373; n = 3; one-way ANOVA), nor in the proportion of Tbr1 positive neurons localized to layer VI (WT: 24.25%; Het: 25.12%; EcKO: 19.25%; p-val = 0.0597; n = 3; one-way ANOVA).

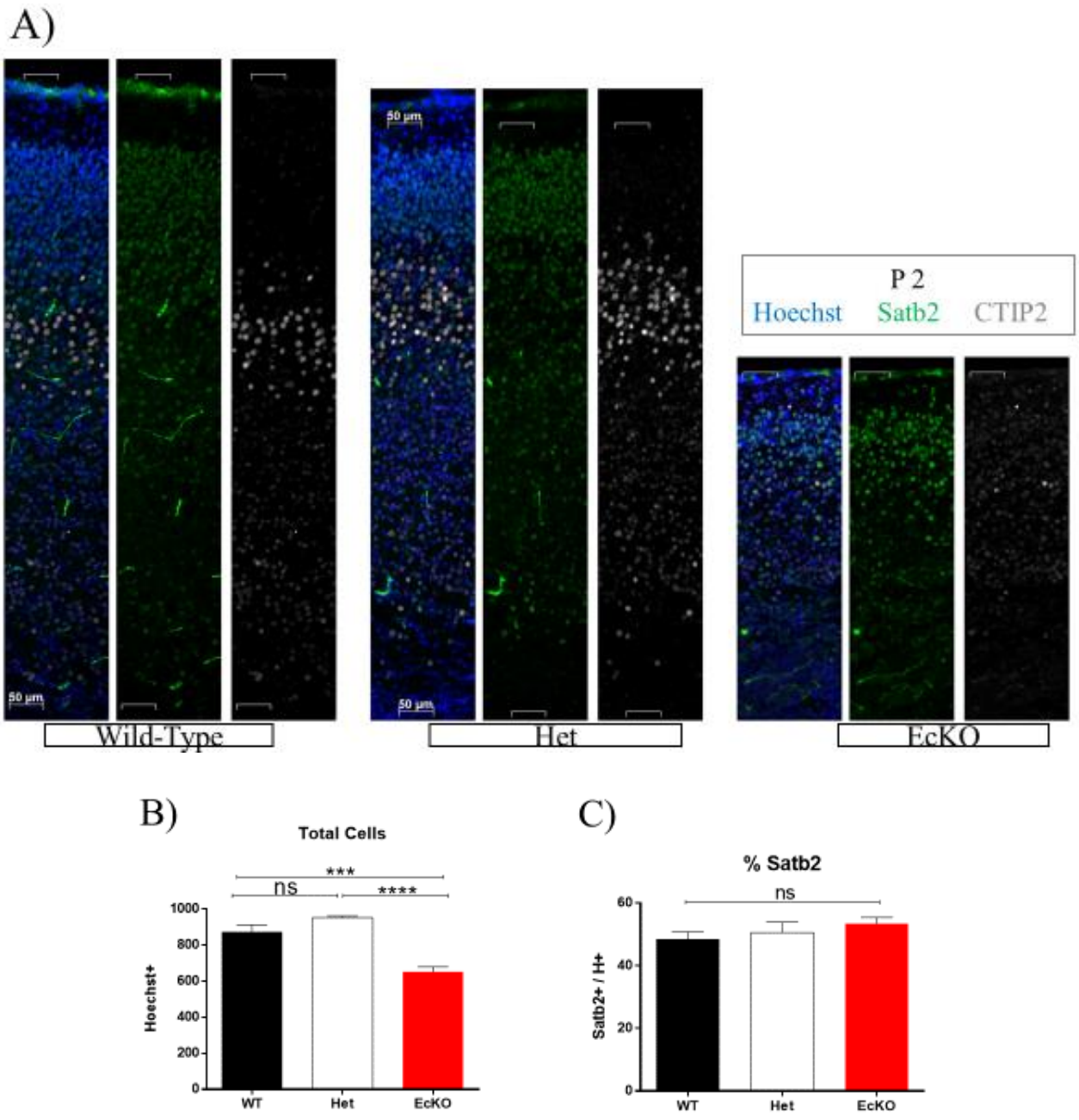

Figure 24 **Bptf deletion leads to a decreased number of cortical neurons.**
A) Representative images of cortical sections of P2 WT, Het and EcKO samples (scale = 50 µm), IF stained with Satb2 (green), Ctip2 (grey) and Hoechst (blue). B) Quantification of the average number of Hoechst + stained cells, WT = 873.5, Het = 953 and EcKO = 653, noticing the significant decrease of cells in the EcKO cortex (n = 3, p-val < 0.0001, one-way ANOVA**** = p-val < 0.0001, *** = p-val < 0.001, ** = p-val < 0.01, * = p-val < 0.05). C) Quantification of the proportions of Satb2+ / Hoechst +, noticing no significant change (n = 3, p-val = 0.373, one-way ANOVA).

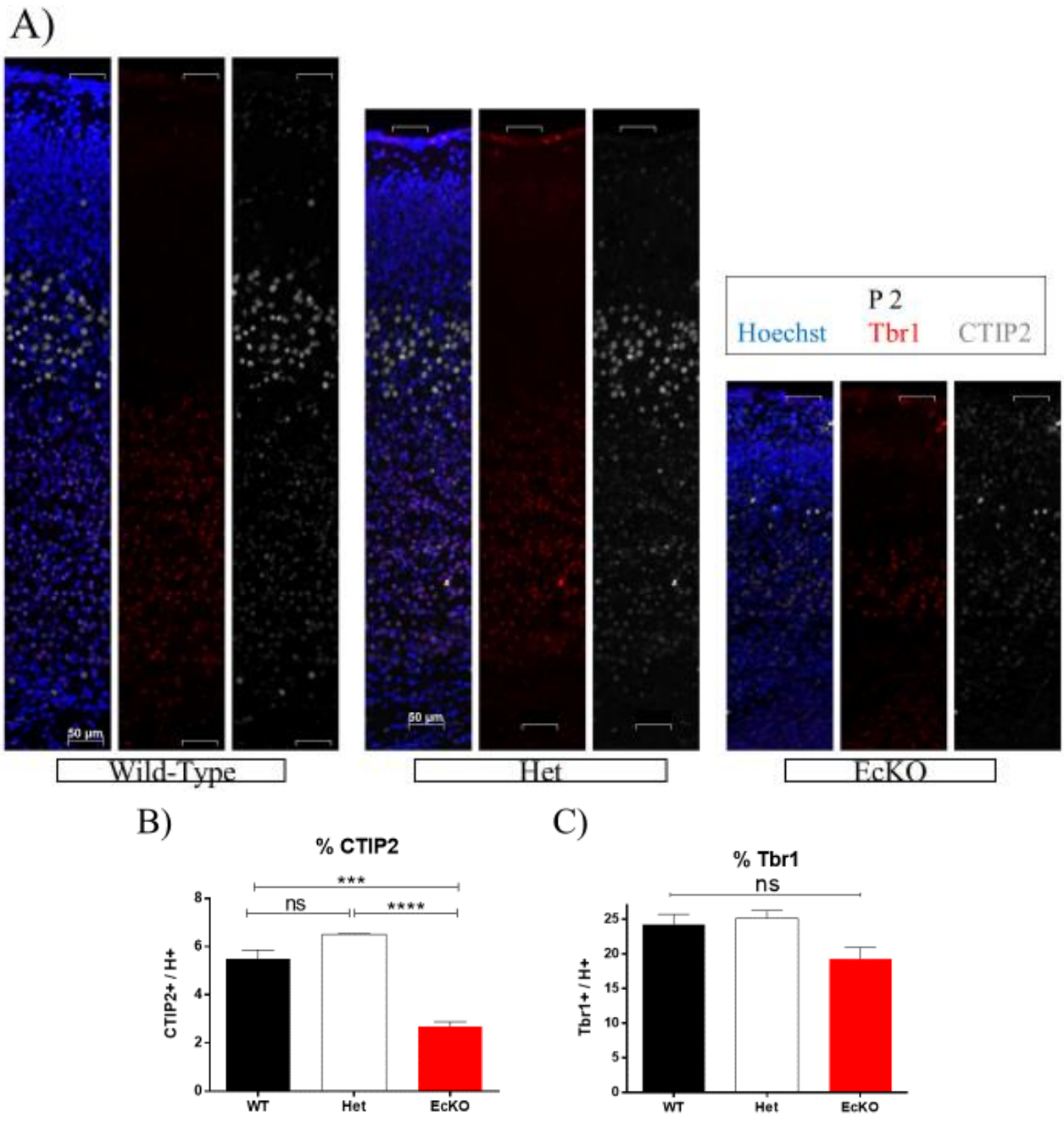

Figure 25 **Bptf deletion leads to a decreased number of Layer V neurons.**
A) Representative images of cortical sections of P2 WT, Het and EcKO samples (scale = 50 µm), IF stained with Tbr1(red), Ctip2 (grey) and Hoechst (blue). B) Quantification of the proportions of Ctip2 + / Hoechst + stained cells, noticing a significant decrease in EcKO (n = 3, p-val < 0.0001, one-way ANOVA, **** = p-val < 0.0001, *** = p-val < 0.001, ** = p-val < 0.01, * = p-val < 0.05). C) Quantification of the proportions of Tbr1 + / Hoechst +, noticing no significant change (n = 3, p-val = 0.0597, one-way ANOVA).

Opposingly, there was a significant near to 10% decrease in the proportion of layers IV-V Foxp1 positively stained cells (WT: 24%; Het: 25.83%; EcKO: 16.66%; n = 3; p-val = 0.0173; one-way ANOVA; Figure 26) as well as, a significant 50% decrease of layer V, Ctip2 positive neurons (WT: 5.5%; Het: 6.5%; EcKO: 2.7%; n = 3; p-val < 0.0001; one-way ANOVA). Last, we performed a birth-dating experiment to analyze the changes occurring to layer IV and V neurons. EdU was injected into pregnant females at E13.5 (approximate formation date for Layer V neurons) and the pups were collected at P2. The brains of the pups were dissected, cryo-sectioned and labelled for Ctip2 and EdU. Figure 27 demonstrates a greater than 50% reduction in the proportion of EcKO Ctip2 positive cells (WT: 5.3%; Het: 7.2%; EcKO = 1.5%; p-val = 0.004; n = 3; one-way ANOVA). Similarly, there was almost a 50% reduction in the proportion of EdU stained cells (WT: 13.72%; Het: 13.69; EcKO: 7.3%; p-val = 0.0051; n = 3; one-way ANOVA). Yet, there was no significant change in the number of co-labelled layer V neurons, Ctip2 + and Edu + / Ctip2 +, (p-val = 0.075; one-way ANOVA), most likely due to the separate decreased proportion of both EdU+ cells and Ctip2+ neurons.

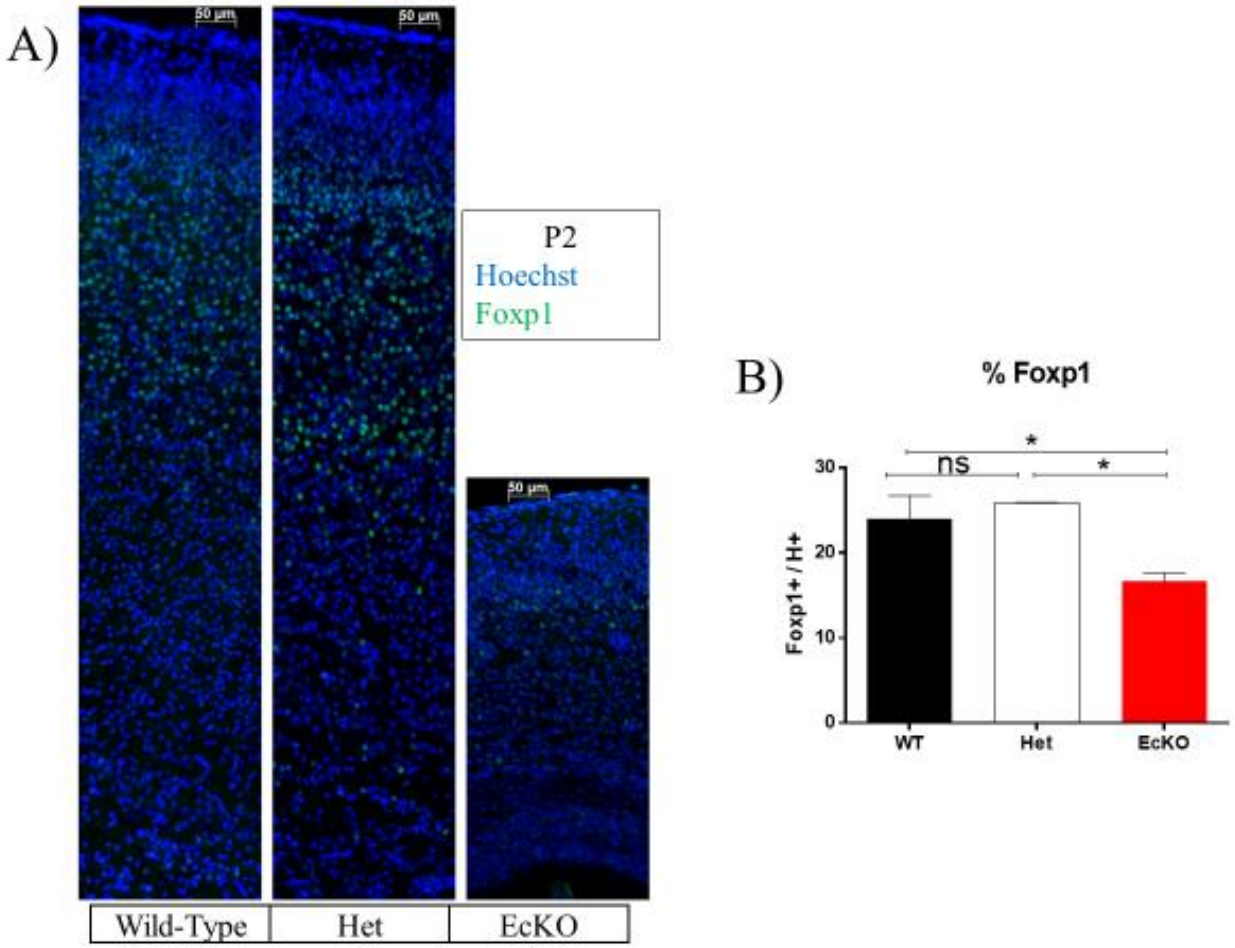

Figure 26 **Bptf deletion leads to a decrease in Foxp1 positively stained cells.**
A) Representative images of cortical sections of P2 WT, Het and EcKO samples (scale = 50 µm), IF stained with Foxp1(green) and Hoechst (blue). B) Quantification of the proportions of Foxp1 + / H+ stained cells, noticing a significant decrease within the EcKO cortex (n = 3, p-val < 0.0173, one-way ANOVA, **** = p-val < 0.0001, *** = p-val < 0.001, ** = p-val < 0.01, * = p-val < 0.05).

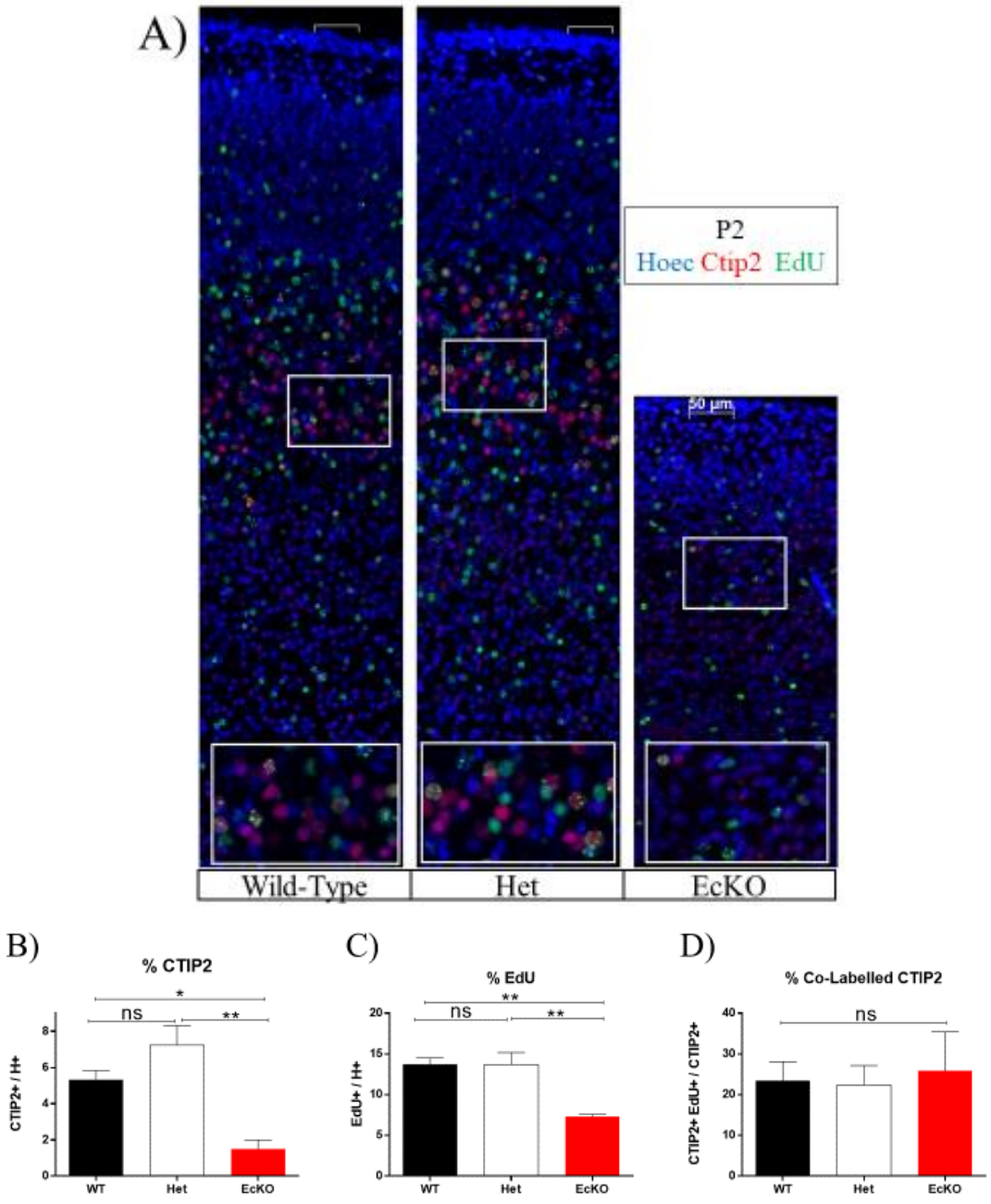

Figure 27 **Bptf deletion leads to a decrease survival of neurons born at E13.5.**
A) Representative images of cortical sections of P2 WT, Het and EcKO samples (scale = 50 µm), IF stained with Ctip2(red), EdU(green) and Hoechst (blue). For this birth-dating experiment, EdU was injected into pregnant dams, when embryos were E13.5, the pups were then collected at P2, their brains dissected and stained. B) Quantification of the proportions of Ctip2 + / Hoechst + stained cells, noticing a significant decrease within the EcKO (n = 3, p-val = 0.004, one-way ANOVA) C) Quantification of proportional EdU + cells, noting a significant decrease in EcKO cortical sections (n =3, p-val = 0.0051, one-way ANOVA). D) Quantification of proportional co-labelled cells, EdU + & Ctip2 + / Ctip2 +, noting no significant change (n = 3, p-val = 0.075, one-way ANOVA, **** = p-val < 0.0001, *** = p-val < 0.001, ** = p-val < 0.01, * = p-val < 0.05).

3.2.5 Transcriptional deregulation in the *Bptf* EcKO cortex

Next, we used RNA-sequencing (RNA-seq) to identify deregulated genes to provide insight into potential mechanisms causing the phenotype in our *Bptf* cKO mice. RNA isolated from forebrain specific tissue of P0 WT and EcKO littermates (n = 4) was sent to Genome Quebec (Montreal) for sequencing. The samples were sequenced on the Illumina NovaSeq 6000 platform, acquiring an average of 78,045,781 reads from WT and EcKO samples, all with a high quality Phred score of 36. To ensure that the mapped and quantified data was segregating based on expression, we compared the datasets using principal component analysis and a heat map of the count matrix (Figure 28). Both the PCA plot and the heat map demonstrated that there was adequate clustering of datasets based on similarities of expression, the EcKO samples are more similar to one another than to the WT samples and vice-versa. Furthermore, in order to perform the differential expression analysis, we used an R package called DESeq2 (105). DESeq2 measures variation of the quantified data, based on the mean and standard deviation for all genes, across all samples. Accurately quantified data will demonstrate low standard deviation for those genes with a high gene count and inversely, genes with a low count will have a higher standard deviation. The data used for this thesis exhibited low count genes with a high standard deviation, as expected of accurately quantified data (Figure 29). We went ahead and performed the differential expression analysis. Our volcano plot (Figure 30) demonstrates in red those differentially expressed genes (DEGs) which surpass a $\log_2$ fold change (L2FC) of +/- 0.5 (meaning 50% more or less when compared to WT) and, have surpassed a significance level of s-value < 0.005 (lfsr, an analogous and more robust method than FDR (106). In this way, we identified 308 upregulated and 349 downregulated genes.

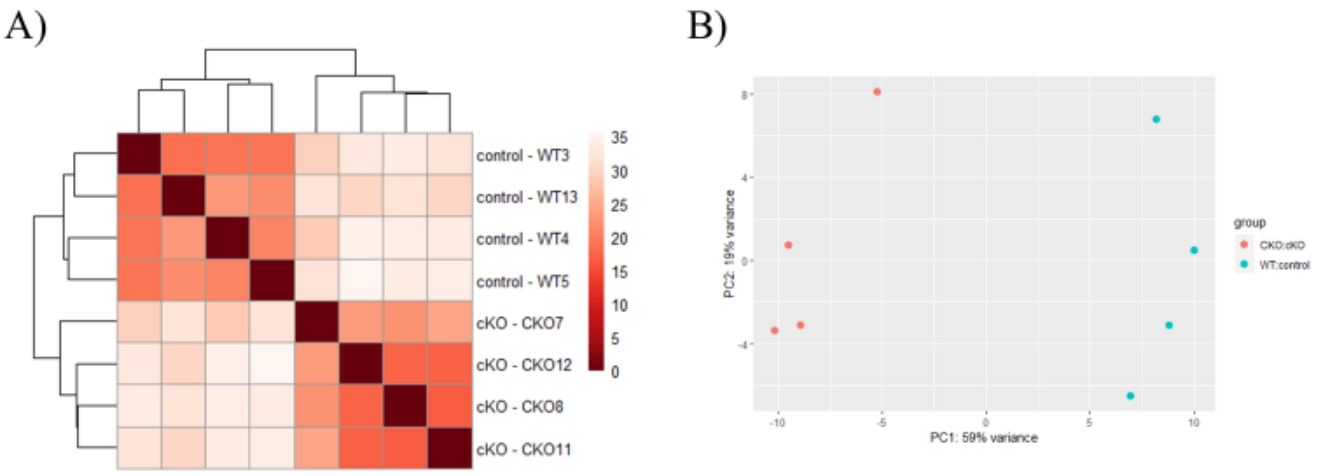

Figure 28 **Accurate sample segregation based on expression data.**
A) Heatmap displaying strong correlation between *Bptf* cKO samples and between WT samples but, not between treatment groups, as expected. B) PCA plot, demonstrating lower variance within treatment groups and accurate segregation of treatment samples based on expression values. A & B) Figures extrapolated from DESeq2, R package on mapped data.

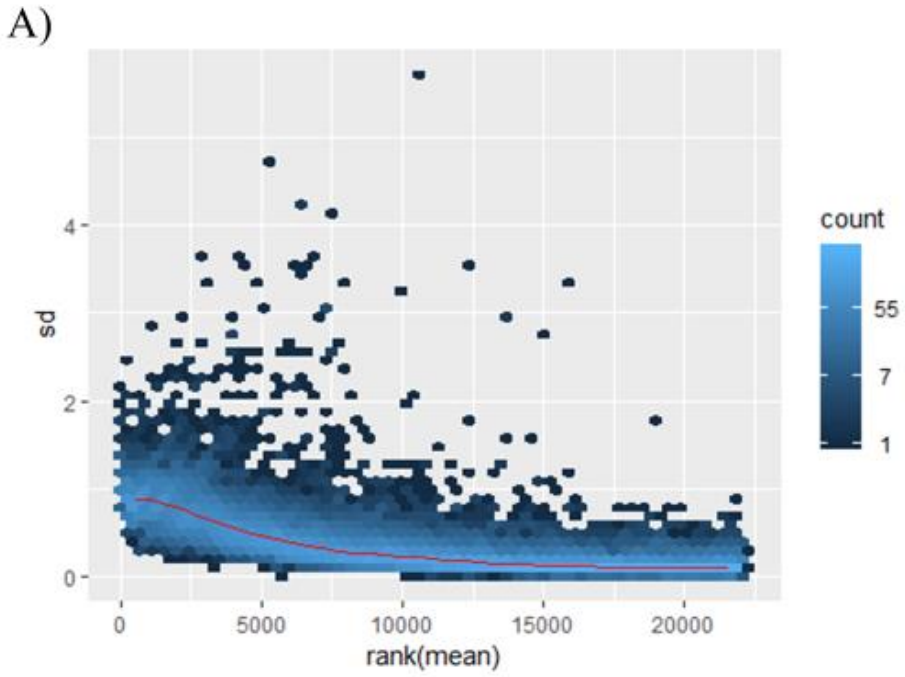

Figure 29 **Standard deviation of all gene counts of EcKO and WT reads.**
A) Highlights the expected standard deviation of gene count metadata, where lower count genes have a greater standard deviation from their corresponding mean, than higher count genes. Figure extrapolated from DESeq2, R package on mapped data.

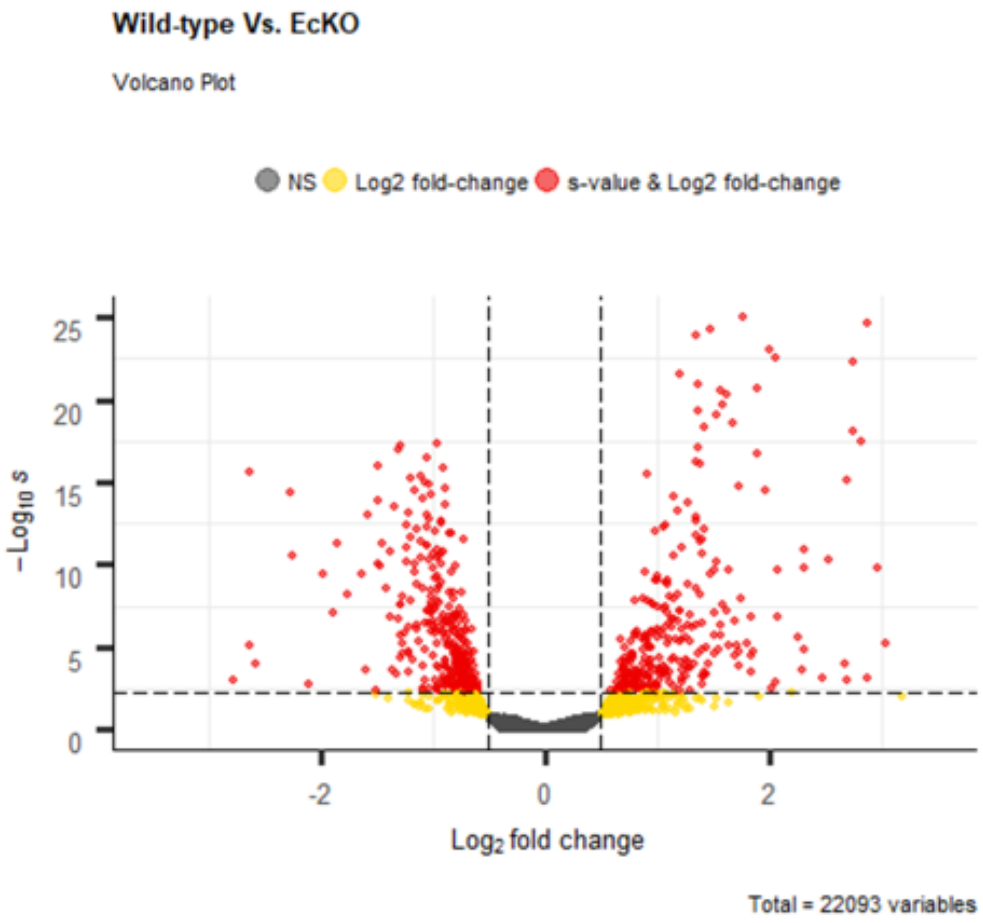

Figure 30 **Volcano plot of the differentially expressed transcripts, comparing EcKO to Wild-type P0 samples.** There is a total of 22,093 transcripts. Yellow = transcripts that surpass the +/- 0.5 log_2 fold threshold, but do not meet significance levels and are not considered to be significantly deregulated. Red = transcripts that surpass the +/- 0.5 log_2 fold threshold and also meet the significance level s-val < 0.005. Those genes with a fold change above +0.5 are upregulated and those below -0.5 are considered to be downregulated. Grey = those transcripts that do not meet any of the criteria and are also not considered differentially expressed.

To determine if our deregulated genes corresponded to specific functional pathways we performed biological process gene ontology (GO) on the DEGs, analyzing upregulated and downregulated genes separately (107). The downregulated DEGs were mostly involved in synaptic signaling, nervous system development, neurogenesis and neuronal differentiation (Figure 31). We extrapolated transcripts that were present in all of the aforementioned GO terms as well as, selected those which are known critical TFs for nervous system development and neurogenesis. For example, Fezf2 and Satb2 are critical TF for neuronal differentiation which are also used as cortical layer markers (described in section 1.1). NeuroD6 is a TF downstream of the proneural gene Neurog2 (6), Nr4a2 is a receptor involved in neuronal development (110) and Emx1 and Sox2 are essential TFs for neural cell fate determination (1). On the other hand, the upregulated DEGs were involved in immune system response, regulation of the inflammatory response as well as, transcriptional control (Figure 32). From these groupings, we identified a set of interesting transcripts: Iba1/Aif1 which is a known marker for microglia, Sall1 an essential TF for microglial function (111) and Arx which is a known TF essential for neuronal progenitor pool proliferation (112). Neurog2 and Tbr2 were also noticed to be upregulated, which are also essential TF for normal cortical development, as described in introduction section 1.1.

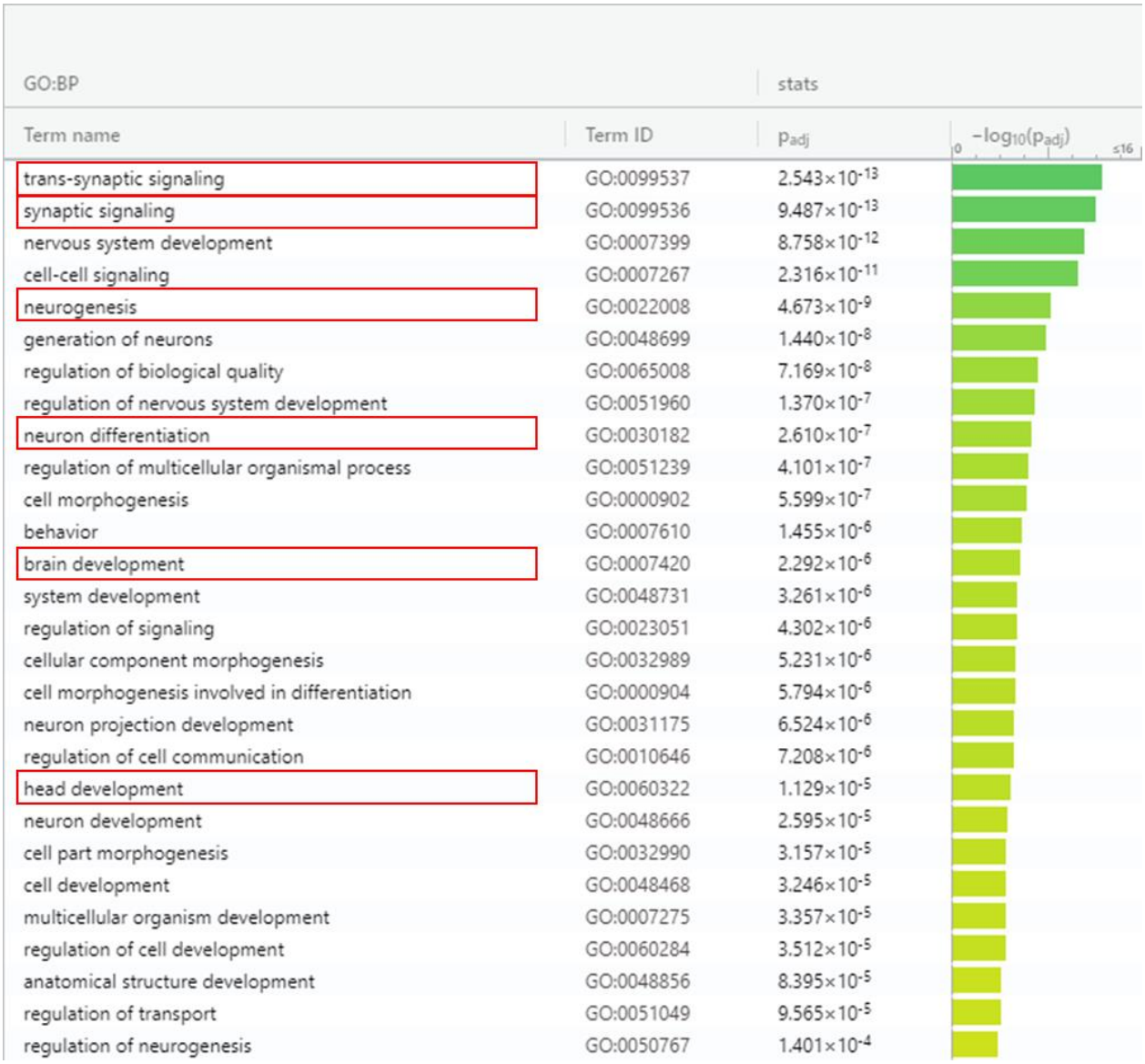

GO:BP		stats	
Term name	Term ID	p_{adj}	$-\log_{10}(p_{adj})$ 0 ≤16
trans-synaptic signaling	GO:0099537	2.543×10^{-13}	
synaptic signaling	GO:0099536	9.487×10^{-13}	
nervous system development	GO:0007399	8.758×10^{-12}	
cell-cell signaling	GO:0007267	2.316×10^{-11}	
neurogenesis	GO:0022008	4.673×10^{-9}	
generation of neurons	GO:0048699	1.440×10^{-8}	
regulation of biological quality	GO:0065008	7.169×10^{-8}	
regulation of nervous system development	GO:0051960	1.370×10^{-7}	
neuron differentiation	GO:0030182	2.610×10^{-7}	
regulation of multicellular organismal process	GO:0051239	4.101×10^{-7}	
cell morphogenesis	GO:0000902	5.599×10^{-7}	
behavior	GO:0007610	1.455×10^{-6}	
brain development	GO:0007420	2.292×10^{-6}	
system development	GO:0048731	3.261×10^{-6}	
regulation of signaling	GO:0023051	4.302×10^{-6}	
cellular component morphogenesis	GO:0032989	5.231×10^{-6}	
cell morphogenesis involved in differentiation	GO:0000904	5.794×10^{-6}	
neuron projection development	GO:0031175	6.524×10^{-6}	
regulation of cell communication	GO:0010646	7.208×10^{-6}	
head development	GO:0060322	1.129×10^{-5}	
neuron development	GO:0048666	2.595×10^{-5}	
cell part morphogenesis	GO:0032990	3.157×10^{-5}	
cell development	GO:0048468	3.246×10^{-5}	
multicellular organism development	GO:0007275	3.357×10^{-5}	
regulation of cell development	GO:0060284	3.512×10^{-5}	
anatomical structure development	GO:0048856	8.395×10^{-5}	
regulation of transport	GO:0051049	9.565×10^{-5}	
regulation of neurogenesis	GO:0050767	1.401×10^{-4}	

Figure 31 **Gene ontology of the biological process of downregulated genes from Figure 30.**
Image depicting gene ontology terms mostly associated with the downregulated gene list. Of note, those terms highlighted within red boxes are major group terms related with neurogenesis, neuronal differentiation and synaptic signaling. Colour palette highlighting most significant (blue) with lowest p-adj value to the less significant (yellow) with higher p-adj values.

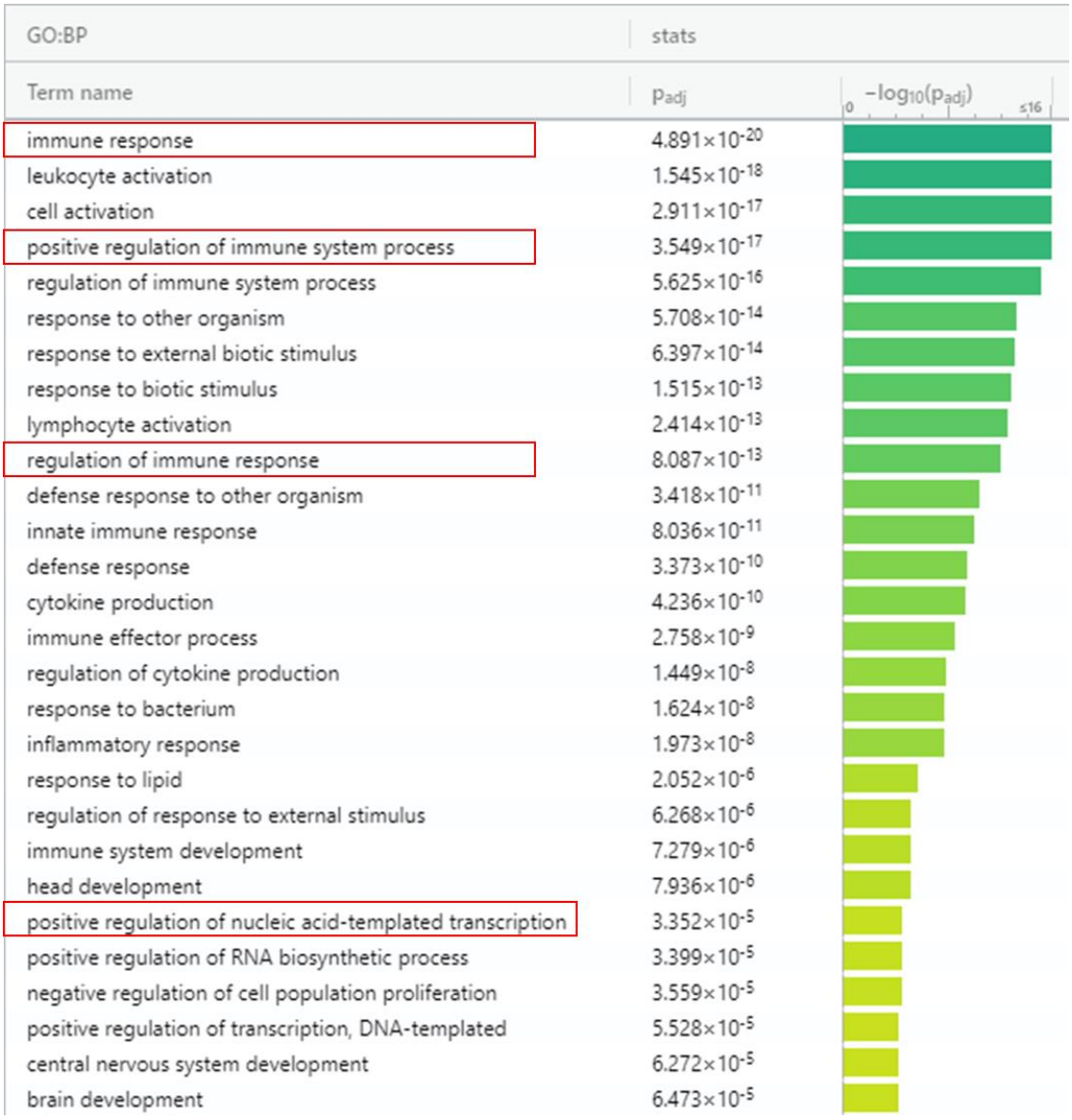

Figure 32 **Gene ontology of the biological process of upregulated genes from Figure 30.**
Image depicting gene ontology terms mostly associated with the upregulated DEGs. Of note, those terms highlighted within red boxes are major group terms related with the immune system, leukocyte activation and immune response. Colour palette highlighting most significant (blue) with lowest p-adj value to the less significant (yellow) with higher p-adj values.

Upon RT-qPCR analysis of RNA isolated from WT, Het and EcKO P0 forebrain samples, we confirmed that *Fezf2* (-2.26 L2FC; p-val = 0.0002), *NeuroD6* (-1.76 L2FC; p-val = 0.0047), *Satb2* (-1.54 L2FC; p-val = 0.0046) and *Nr4a2* (-1.82 L2FC, p-val = 0.005) were significantly downregulated in the mutant samples (Figure 33; n = 6, one-way ANOVA). Since Bptf interacts with the ISWI proteins Snf2h and Snf2l, we also tested whether loss of Bptf had any effect on the expression of *Smarca5* and *Smarca1*, respectively. We observed no significant change between WT, Het and EcKO forebrain P0 samples (Figure 34, n = 6, one-way ANOVA), either for *Snf2h* expression (WT L2FC = 1.1*10-7; Het L2FC = 0.4; EcKO L2FC = -0.63; p-val = 0.18) nor for *Snf2l* gene expression (WT L2FC = $-8.8*10^{-7}$; Het L2FC = 0.677; EcKO L2FC = -0.58; p-val = 0.15). We also performed RT-qPCR to validate the upregulated genes, however no significant changes between WT, Het and EcKO samples were observed (Figure 35A, n = 6, p-val > 0.05, one-way ANOVA). Nonetheless, we stained P2 brain sections using an αIba1/Aif1 antibody, a marker for both ramified and activated microglia, to validate the increase of Iba1. In this experiment we observed a significant proportional increase from 0.95 to 3.7% (n = 3, p-val < 0.0001, one-way ANOVA) of microglia displayed in the EcKO murine forebrain, Figure 36. This increase in Iba1+ microglia corroborates the significant increase of immune response related DEGs, which were not validated by RT-qPCR.

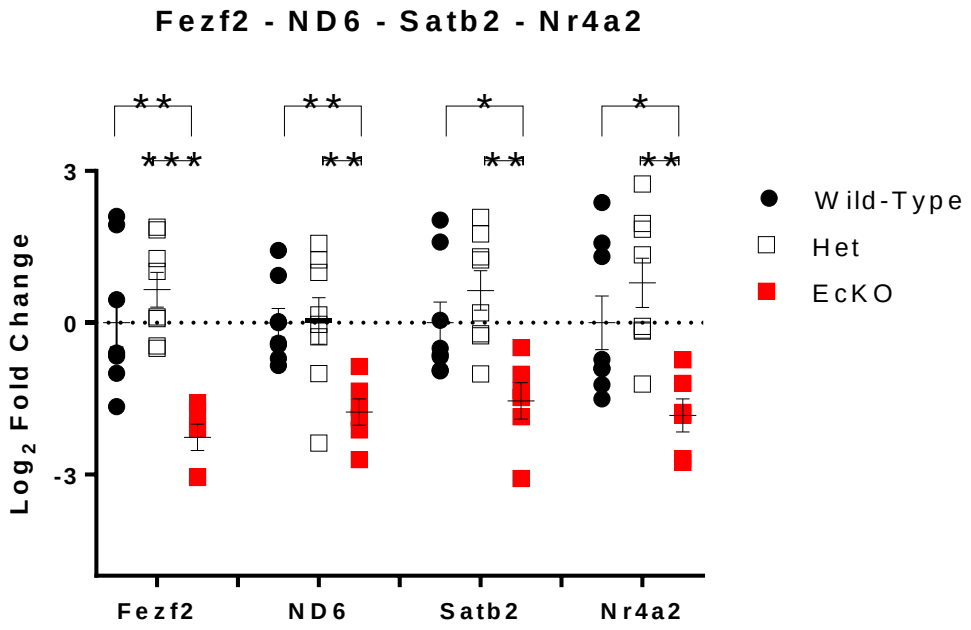

Figure 33 **Validation of downregulated transcripts involved in neurogenesis and neuronal differentiation.** RT-qPCR quantifications from WT, Het and EcKO P0 forebrain specific cDNA. Graph demonstrates the $\log_2$ fold downregulation of *Fezf2* (-2.26 L2FC, p-val = 0.0002), *NeuroD6* (-1.76 L2FC, p-val = 0.0047), *Satb2* (-1.54 L2FC, p-val = 0.0046) and *Nr4a2* (-1.82 L2FC, p-val = 0.005) transcripts, only observed to be deregulated in the EcKO and not in the Het or WT cDNA samples. (n = 6, one-way ANOVA, **** = p-val < 0.0001, *** = p-val < 0.001, ** = p-val < 0.01, * = p-val < 0.05).

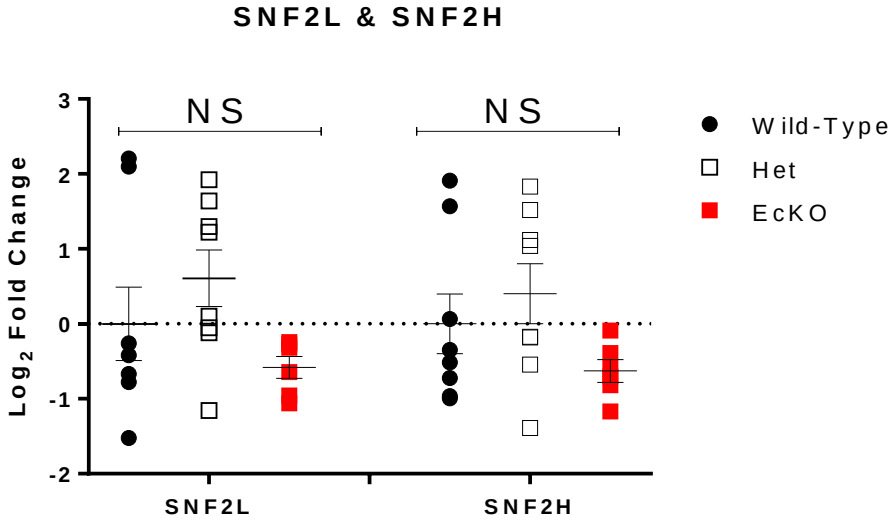

Figure 34 **Unchanged transcript expression of NURF ATPase interacting subunits.** RT-qPCR quantifications from WT, Het and EcKO P0 forebrain specific cDNA. Graph demonstrates the $\log_2$ fold change of *Smarca1* and *Smarca5*, demonstrating no significant change between samples. (n = 6, p-val > 0.05, one-way ANOVA).

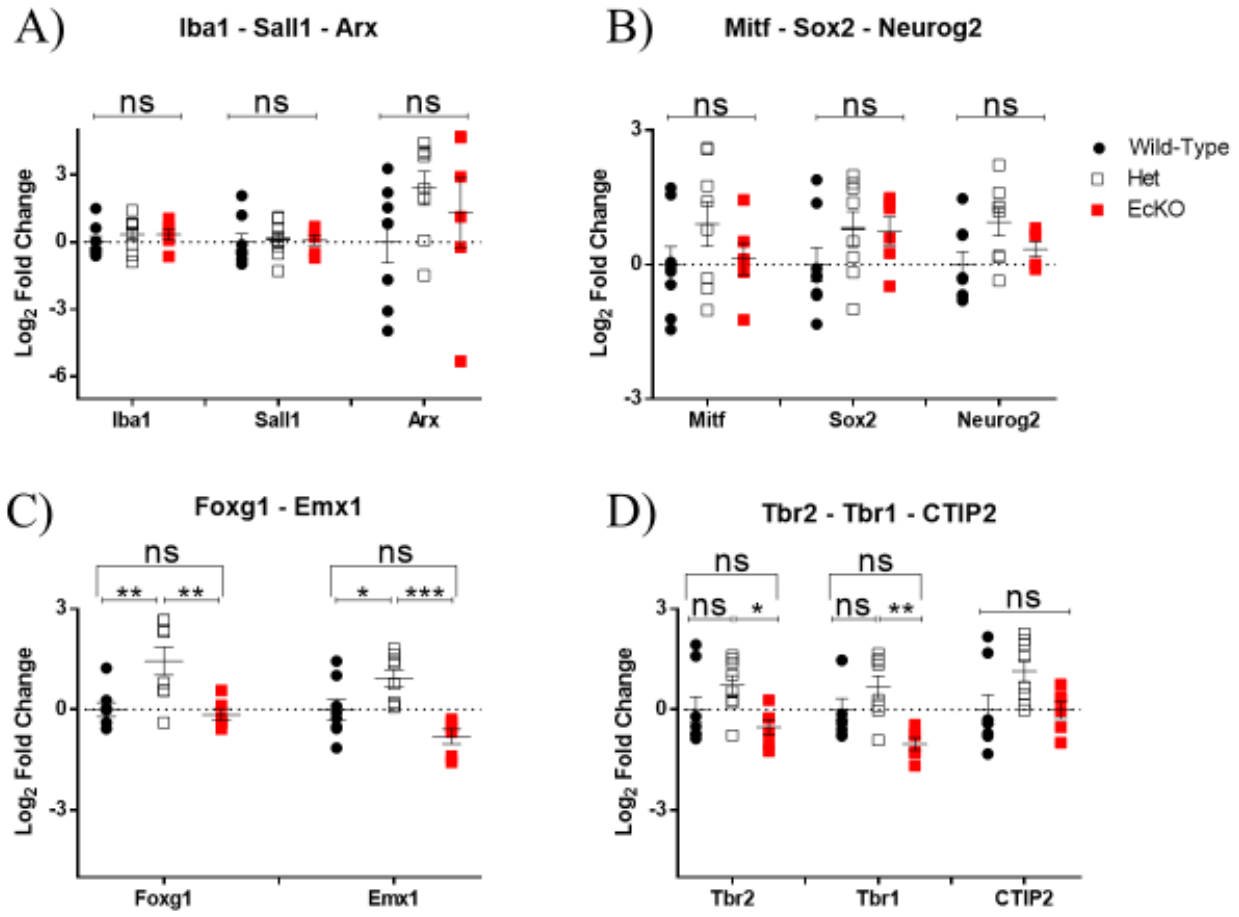

Figure 35 **Set of interesting genes not significantly deregulated through RT-qPCR.**
A) Set of upregulated transcripts in the RNA-seq differential expression analysis out of which, non displaying any significant $\log_2$ fold change (p-val > 0.05). These three genes were part of the immune response GO term mentioned in (Figure 32) B) Separate set of downregulated DEGs, which did not validate the results observed in the differential expression analysis, displaying no significant change between samples (p-val > 0.05) C) *Emx1* is also part of the downregulated DEGs, which is interestingly upregulated in Het but, displaying no change between WT and EcKO. *Foxg1* is a kef TF involved in neurogenesis which was considered to be of importance based on its pro-neural regulatory role (113). The RT-qPCR quantifications do not demonstrate any change between the WT and EcKO but, again note an increase expression in the Het cDNA sample. D) *Tbr1* and *Ctip2* are previously mentioned layer marker proteins which display no significant expressional changes in the cDNA between WT and EcKO (p-val > 0.05). *Tbr2* also mentioned above, is the marker for IPCs which is also not downregulated when comparing WT to EcKO samples (p-val > 0.05). A-D) All are RT-qPCR quantifications from WT, Het and EcKO P0 forebrain specific cDNA, which do not validate previous results, either in IF staining experiments, or in the RNA-seq differential expression analysis. (n = 6, one-way ANOVA, **** = p-val < 0.0001, *** = p-val < 0.001, ** = p-val < 0.01, * = p-val < 0.05, ns = not significant p-val > 0.05).

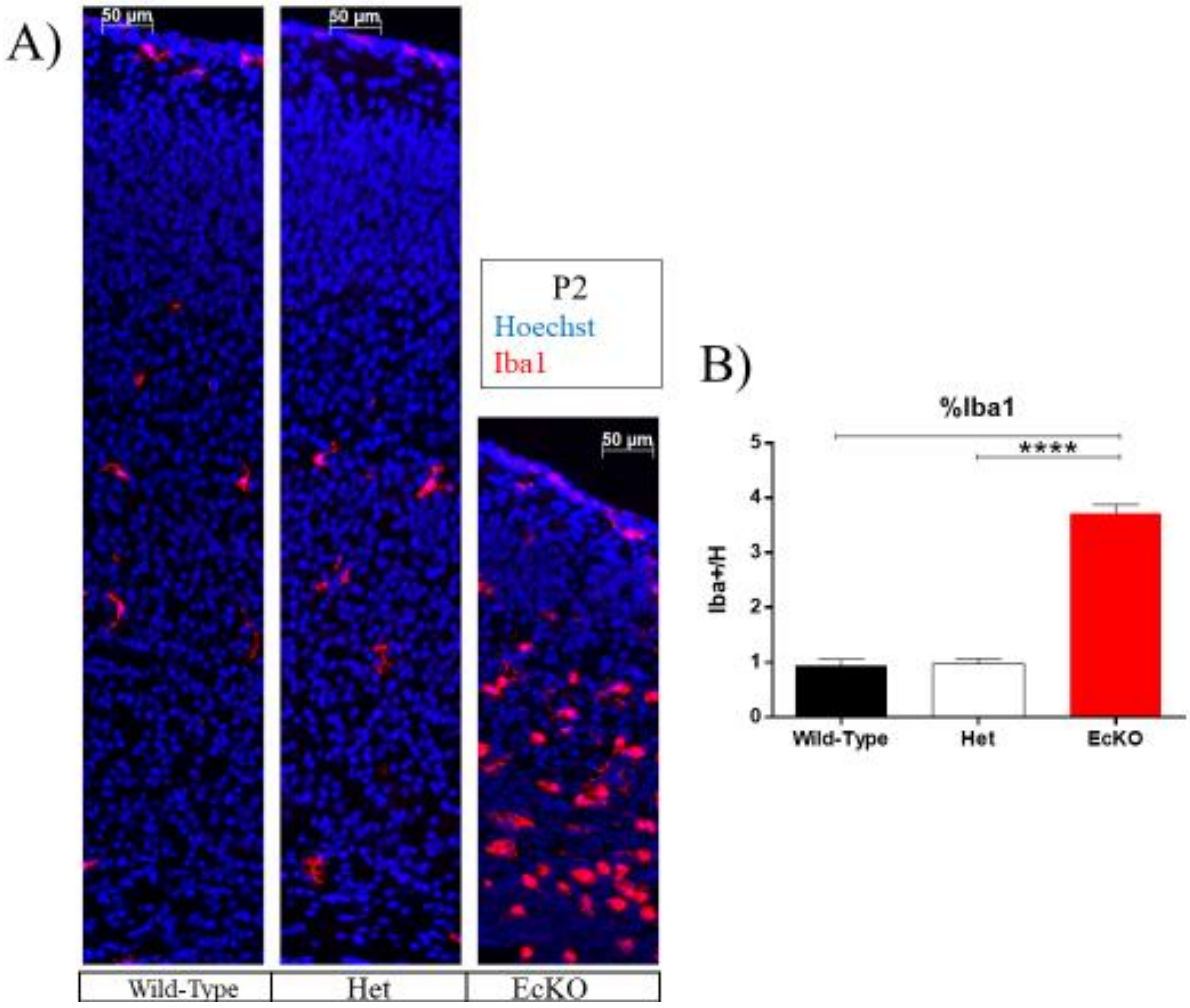

Figure 36 **Dramatic increase in EcKO cortical microglia.**
A) Representative images of cortical sections of P2 WT, Het and EcKO samples (scale = 50 µm), IF stained with Iba1/Aif1 (red) and Hoechst (blue). B) Quantification of the proportions of Iba1 + / Hoechst + stained cells, noticing a significant increase within the EcKO (n = 3, p-val < 0.0001, one-way ANOVA, **** = p-val < 0.0001, *** = p-val < 0.001, ** = p-val < 0.01, * = p-val < 0.05).

On a separate but related note, as mentioned in section 1.1, Foxg1 and Neurog2/Neurogenin2 are key transcription factors demonstrated to be crucial for normal cortical development (1). *Foxg1* is expressed as early as E8.5 and *Neurog2* gene expression begins around E10.5 (14). Considering these genes were not validated to be deregulated either at P0 (Figure 35), we performed IF analysis on these proteins to verify their status in the EcKO cortex. Interestingly, there was no change in the percentage of Foxg1 positively stained cells, Foxg1 + / H +, either in the cortical plate (Figure 37;WT: 19.94%; Het: 20.21%; EcKO: 17.06%; p-val = 0.0558; n = 4; one-way ANOVA) nor in the ventricular zone and intermediate zone (WT: 57.36%; Het: 57.08%; EcKO: 59.66%; p-val = 0.87, n = 4, one-way ANOVA) between any of the mouse groups at E13.5. Similarly, there was also no change in the percentage of Neurog2 positive cells (Figure 38), Neurog2 + / H +, in the entire E13.5 cortex when comparing WT (18.48%), Het (18.09%) and EcKO sections (16.96%; p-val = 0.61; n = 4, one-way ANOVA).

Last, disease ontology (DO), similar to GO, is used to identify human genes which are associated with known human disease (108). In the case of this thesis, we used human gene orthologs to the murine DEGs as a list of genes for the DO analysis. The downregulated DEGs demonstrated that our mice have altered transcripts associated with mental health disorders as well as cognitive and mood disorders resembling the neurodevelopmental and intellectual disabilities affecting the human NEDDFL patients (Figure 39A). On the other hand, the upregulated DEGs were involved in immune system disease and leukemia which is most likely due to the increase in microglia observed from Figure 36 (Figure 39B).

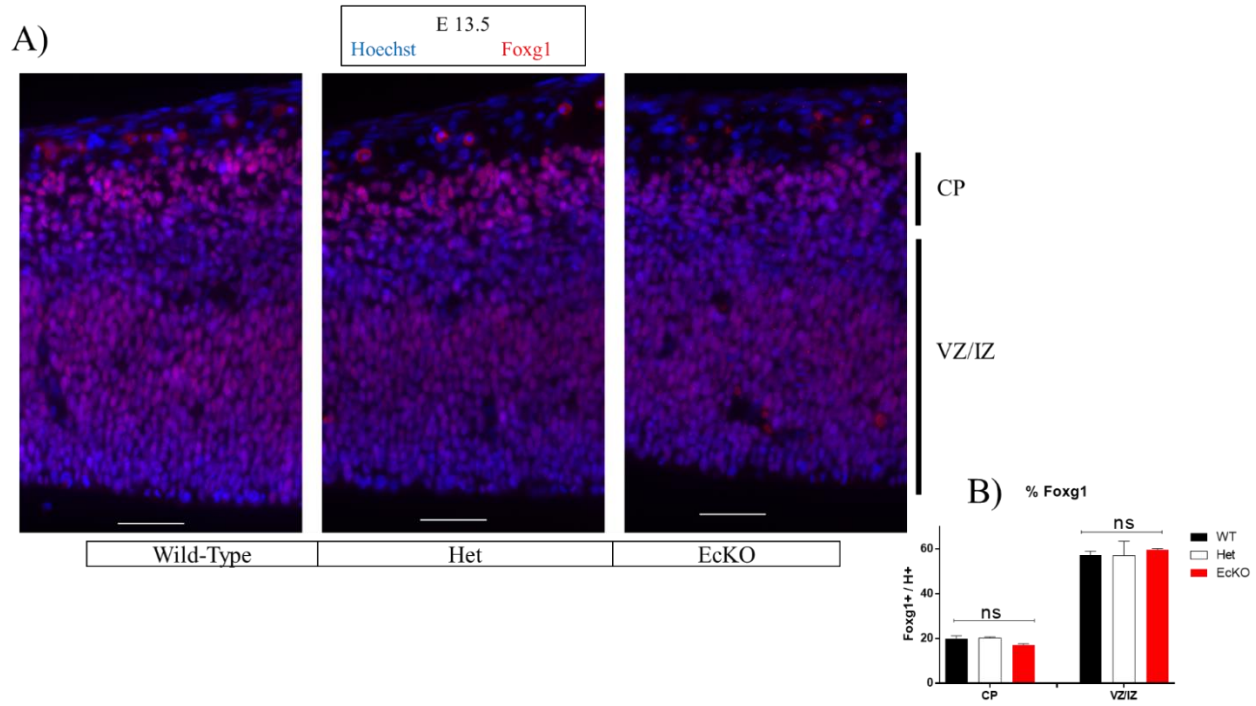

Figure 37 **Unaltered E13.5 Foxg1 protein expression.**
A) Representative images of cortical sections of E13.5 WT, Het and EcKO samples (scale = 50 µm), IF stained with Foxg1 (red) and Hoechst (blue). B) Quantification of the proportions of Foxg1 + / Hoechst + stained cells, with no significant change either in the cortical plate (CP; p-val = 0.0558) nor in the ventricular and intermediate zone (VZ/IZ; p-val = 0.87; n = 4; one-way ANOVA).

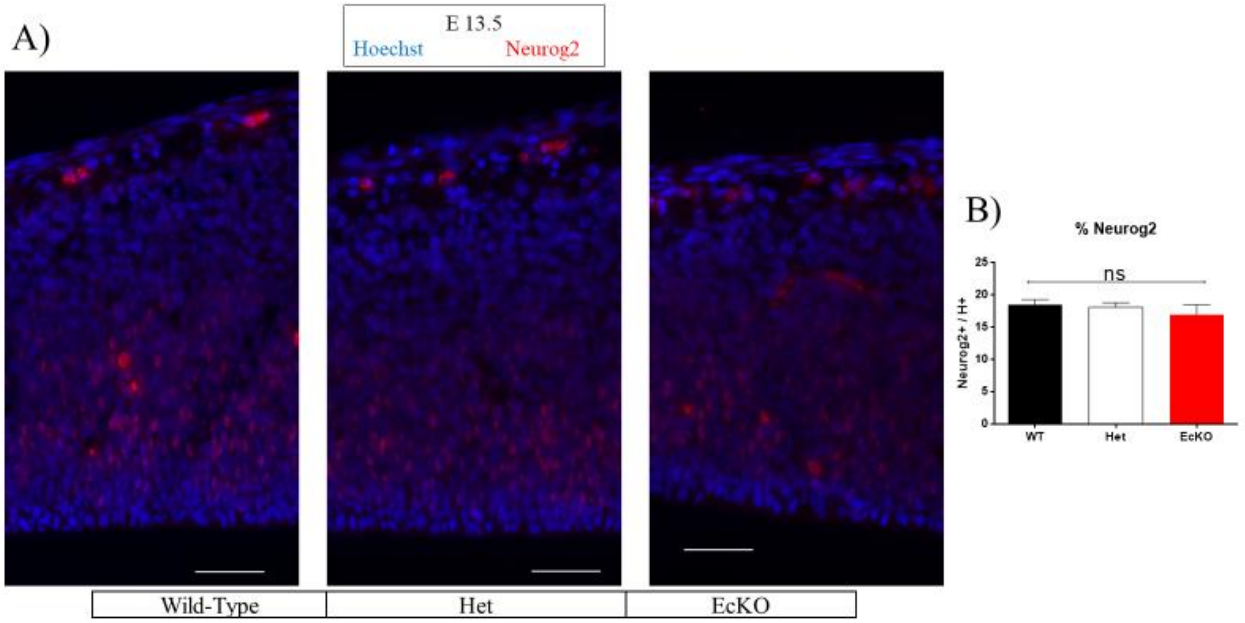

Figure 38 **Unaltered E13.5 Neurog2 protein expression.**
A) Representative images of cortical sections of E13.5 WT, Het and EcKO samples (scale = 50 µm), IF stained with Neurog2 (red) and Hoechst (blue). B) Quantification of the proportions of Neurog2 + / Hoechst + stained cells, with no significant change (n = 4, p-val < 0.612, one-way ANOVA).

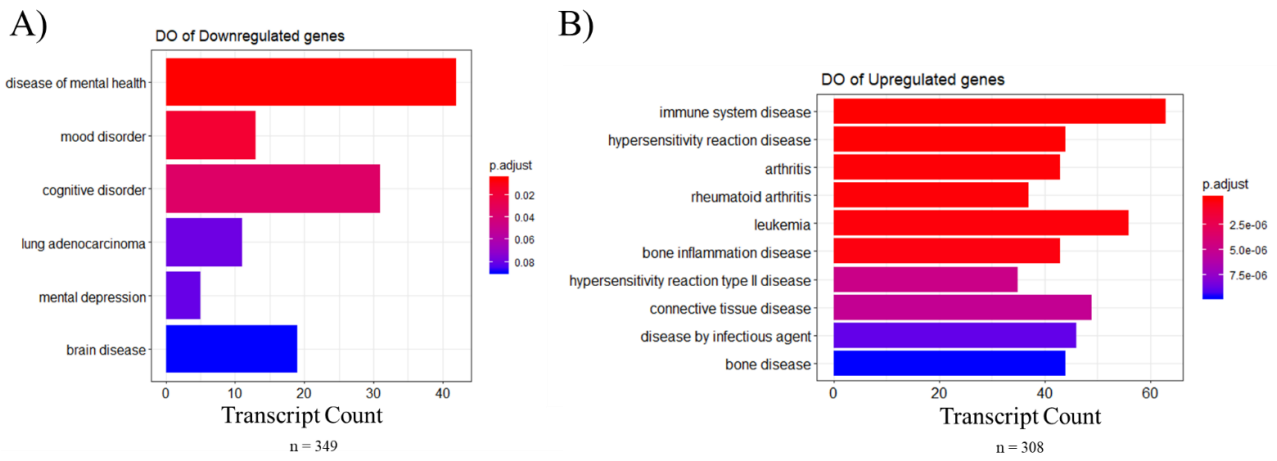

Figure 39 **DO demonstrates DEGs are involved in mental health, mood disorders and immune system disease.**
A) Graph depicting the DO of the downregulated DEGs from (Figure 30), highlighting mainly that these transcripts are associated with disease of mental health and mood disorder. B) Graph depicting the DO of the upregulated DEGs from (Figure 30), highlighting mainly that these transcripts are associated with immune system disease and leukemia.

3.2.6 Increased proportion of cortical cell death increases microglial in EcKO mice

As mentioned in section 3.2.5, there is a significant increase in the percentage of microglia in the cortex of the EcKO mice. To identify the reason for this increase we IF-stained E13.5, E15.5, P2 and P7 cortical sections for Iba1 (microglia) and for cleaved Caspase 3 (αCC3) as a marker of apoptotic cells. These experiments were set-up to create a broad timeline, identifying the extent and reason for microglial presence in the EcKO cortices. No significant proportional change in either Iba1+ microglia (WT: 0.87; Het: 0.87; EcKO: 0.73;p-val = 0.705) nor apoptotic events (WT: 0.53; Het: 0.53; EcKO: 0.6;p-val = 0.965, n = 4, one-way ANOVA) was observed in the E13.5 cortex (Figure 40). However, by E15.5 (Figure 41) there is a 10-fold increase of apoptotic cells (CC3 + / H+) within the cortical plate, from 0.07% and 0.13% in WT and Het, respectively, to 1.94% in the EcKO (p-val < 0.002, n = 3, one-way ANOVA). Yet, at E15.5 the levels of microglia in the cortical plate remain practically unchanged (WT: 0.23%; Het: 0.08%; EcKO: 0.46%; p-val = 0.02; n = 3; one-way ANOVA).

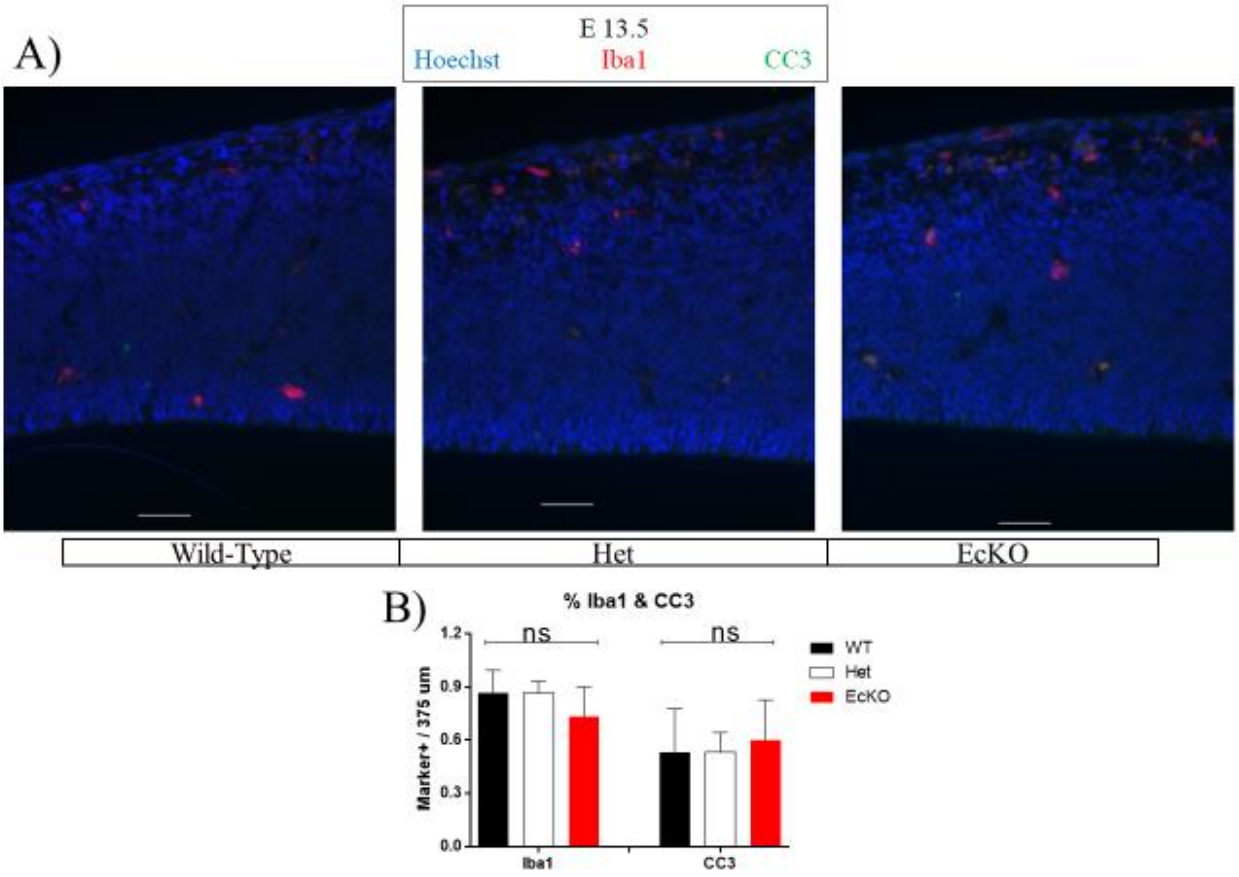

Figure 40 **No change in microglia or cell death at E13.5.**
A) Representative images of cortical sections of E13.5 WT, Het and EcKO samples (scale = 50 µm), IF stained with Iba1/Aif1 (red), Cleaved Caspase 3 (green) and Hoechst (blue). B) Quantification of the proportions of marker + / 375 um, noticing no significant change in either microglia (p-val = 0.705) nor cell death (p-val = 0.965) (n = 4, one-way ANOVA). The positively stained cells were counted in a rectangle 375 um long, and whole cortex wide.

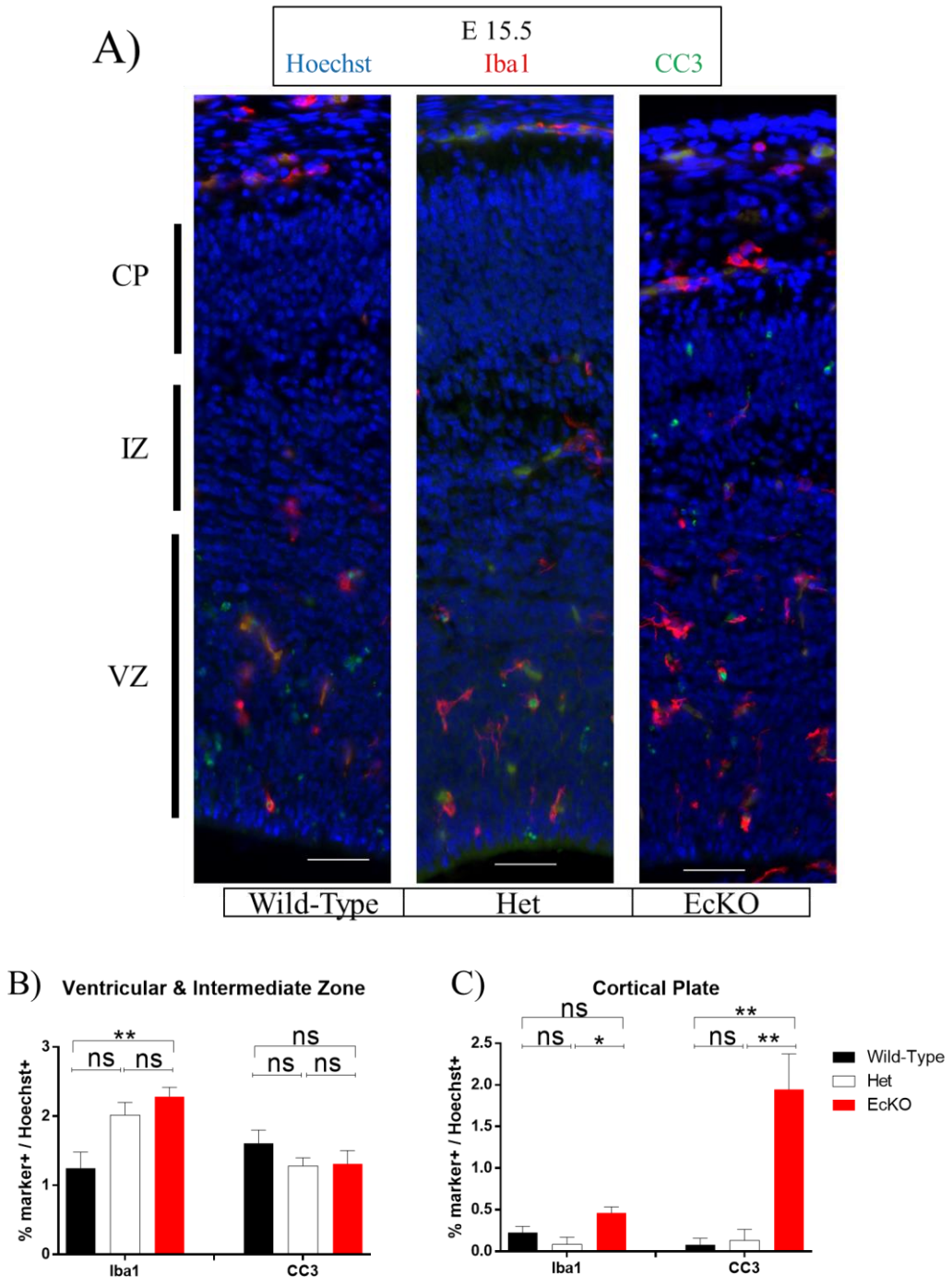

Figure 41 **Increased cell death in the cortical plate of EcKO at E15.5.**
A) Representative images of cortical sections of E15.5 WT, Het and EcKO samples (scale = 50 µm), IF stained with Iba1/Aif1 (red), CC3 (green) and Hoechst (blue). The cortical images were divided into three sections: VZ = ventricular zone, IZ = intermediate zone and CP = cortical pate. Due to ambiguity in separating the VZ and IZ, they were grouped as one. Cell were then counted separately in two groups: VZ & IZ as one and CP as another. B) Quantification of the proportions of marker + (iba1 or CC3) / Hoechst + stained cells in the VZ and IZ of WT, Het and EcKO. Demonstrating an increase in microglia present in the EcKO (p-val < 0.01). C) Quantification of the proportions of marker + (Iba1 or CC3) / Hoechst + stained cells in the CP of WT, Het and EcKO. Demonstrating an increase in cell death only in EcKO CP (p-val < 0.002). B-C) n = 3, one-way ANOVA, **** = p-val < 0.0001, *** = p-val < 0.001, ** = p-val < 0.01, * = p-val < 0.05, ns =not significant.

Later by P2, it becomes evident that the EcKO cortex maintained the percentage of apoptotic events which led to a surge of microglia to engulf the cellular debris (Figure 42). There is maintained increase in the proportion of apoptotic events, from 1.94% in E15.5 cortical plate to a 1.7% at P2, occurring solely in the EcKO cortical sections, not observed in either the WT nor in the Het sections (WT: 0; Het: 0; n = 3; p-val not available). Microglia makes up 0.46% (Iba1 + / H +) in P2 WT cortical sections, while the Het microglia makes up 0.3% of the total number of counted cells, the EcKO cortex however, demonstrates a close to 10-fold increase in microglia (3.4%; p-val < 0.0001; n = 3; one-way ANOVA). Considering the increase in microglia and apoptosis, we determined that 19.7% of microglia are engulfing cellular debris (Iba1 + & CC3 + / Iba1 +), again only detectable in the EcKO cortical sections (WT: 0; Het: 0; n = 3; p-val not available). Last, we analyzed P7 cortical sections as the final checkpoint for the microglia and cell death (Figure 43). The apoptotic events in the EcKO cortex drop from 1.7% at P2 to 0.86% at P7, comparable to the WT and Het littermate proportion (WT: 0.32%; Het: 0.71%; EcKO: 0.86%; n = 4, p-val = 0.0358; one-way ANOVA). Yet, the microglia in the EcKO cortex seem to take longer to stabilize as they remain proportionally higher (5.53%), doubling that of the WT microglia percentage (2.02%) as well as, close to doubling the Het percentage (3.25%; n = 4, p-val = 0.0025; one-way ANOVA).

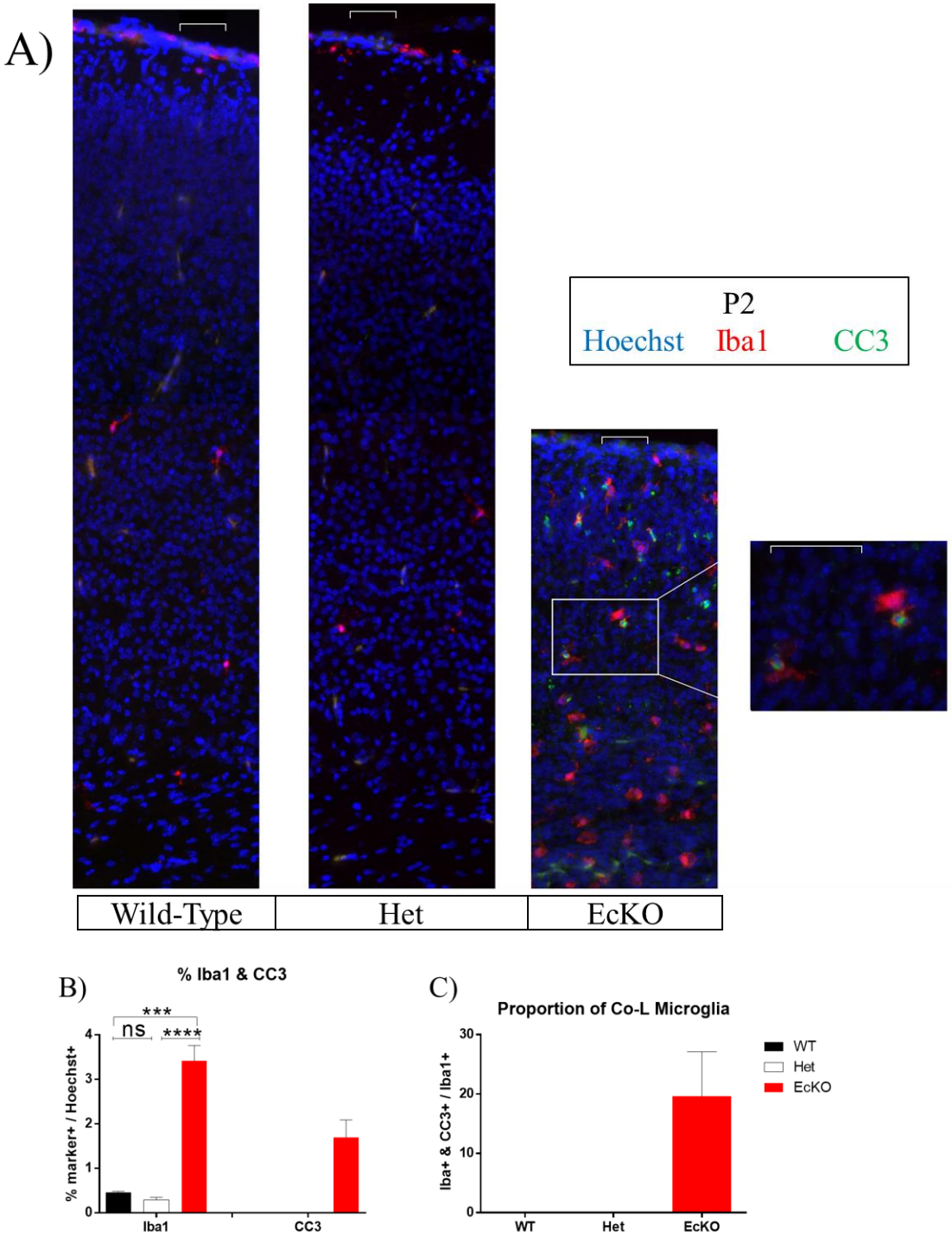

Figure 42 **Increased cortical cell death and microglia presence only on EcKO at P2.**
A) Representative images of cortical sections of P2 WT, Het and EcKO samples (scale = 50 µm), IF stained with Iba1/Aif1 (red), CC3 (green) and Hoechst (blue). B) Quantification of the proportions of marker + (Iba1 or CC3) / Hoechst + stained cells comparing WT, Het and EcKO. Demonstrating a proportional increase in microglia present in the EcKO (p-val < 0.0001), as well as proportional cell death only observed in the EcKO (1.7% +/-.4 SEM). C) Quantification of proportional co-labelled microglia, Iba1 + & CC3 + / Iba1 +. Demonstrating only co-labelled microglia in the EcKO (19.7% +/- 7.4 SEM). B-C) n = 3, one-way ANOVA, **** = p-val < 0.0001, *** = p-val < 0.001, ** = p-val < 0.01, * = p-val < 0.05.

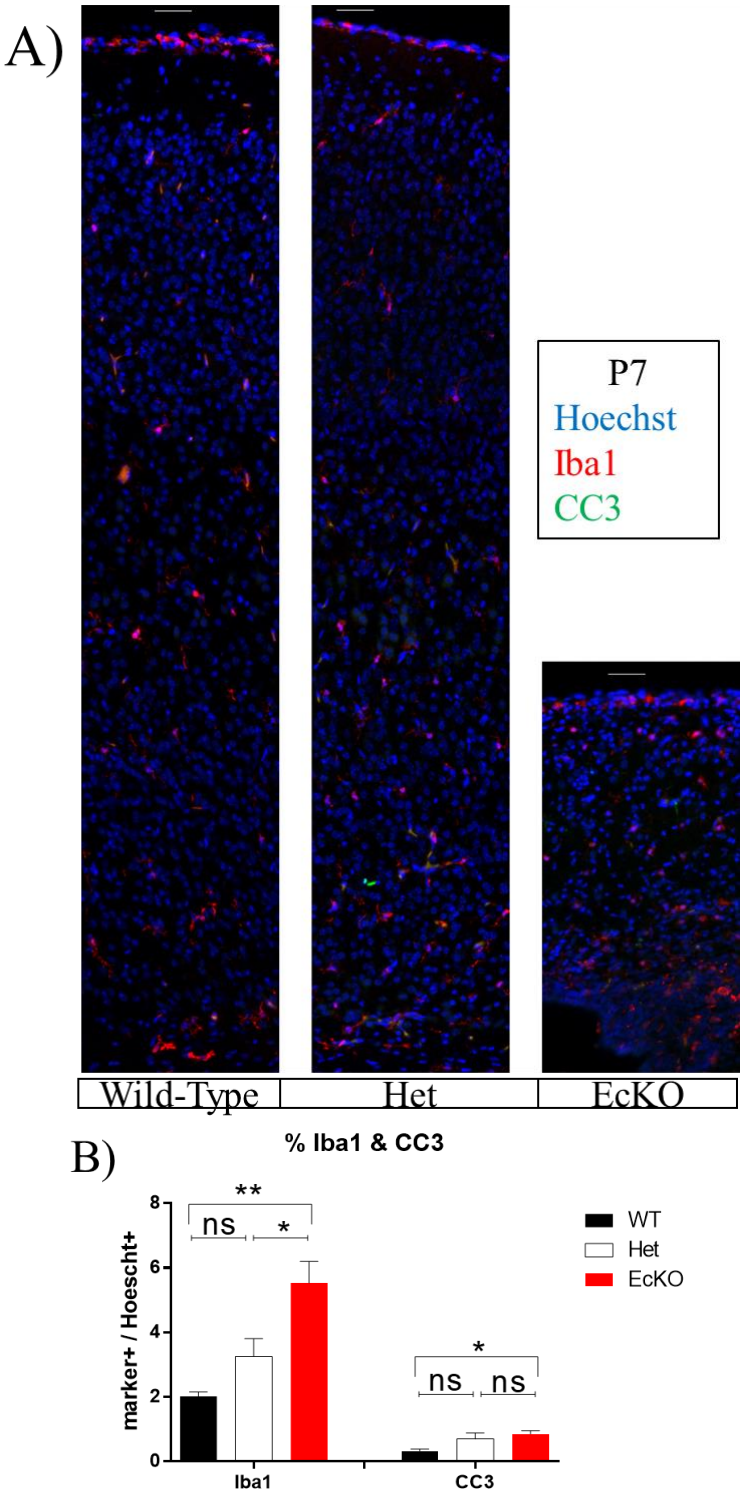

Figure 43 **Maintained microglial presence after decrease in apoptotic events in EcKO P7 cortices.**
A) Representative images of cortical sections of P7 WT, Het and EcKO samples (scale = 50 µm), IF stained with Iba1/Aif1 (red), CC3 (green) and Hoechst (blue). B) Quantification of the proportions of marker + (Iba1 or CC3) / Hoechst + stained cells comparing WT, Het and EcKO. Demonstrating a proportional increase in microglia present in the EcKO (p-val = 0.0025), as well as a very slight increase in proportional cell death only observed in the EcKO (p-val = 0.035); n = 4; one-way ANOVA; **** = p-val < 0.0001; *** = p-val < 0.001; ** = p-val < 0.01; * = p-val < 0.05; ns = p-val > 0.05.

4. Discussion

4.1. *Bptf* is essential for intermediate neuronal progenitor cell proliferation

In this thesis, we have conditionally inactivated *Bptf* in the neocortex of the mouse using *Emx1*-Cre as a driver for its removal. It is the first time Bptf has been removed in the central nervous system, leading to significant cortical hypoplasia yet, the mice have been demonstrated to survive. Furthermore, the reduced cortex also exhibited altered Foxp1 and Ctip2 protein expression patterns specific to neurons in layers IV and V, respectively. The RNA-seq analysis demonstrated that major TFs involved in neurogenesis and nervous system development are dysregulated as well as, highlighted an increase in immune system response. Microglia are close to ten-times more prevalent in the cortex of the EcKO mice, in response to an increase in cell death.

Radial glial cells and intermediate neuronal progenitors together form the progenitor pool of the developing cortex, these cells are in charge of undergoing differentiation and proliferation in order to populate the cortical plate with diverse neuronal sub-types. RGCs are the neural stem cell population that derived from the neuroepithelial cell layer of the neural tube. These cells can expand symmetrically to produce more RGCs or divide asymmetrically to generate an intermediate neuronal progenitor cell (IPCs) or a committed neuron (113). *Bptf* exon 2 excision leads to a 5% reduction of IPCs observed only in the EcKO mice at E15.5 (Figure 21) but, without significantly altering the proportion of IPCs entering S-phase (Tbr2+ & EdU+ / Tbr2+ cells). This suggests Bptf is essential for either the differentiation of RGCs into IPCs, an altered cell-cycle progression leading to the reduced number of IPCs or, an increase in cell death within the progenitor pool. Regardless, the proportion of RGCs and those entering S-phase are similar between the EcKO, Het and WT littermates (Figure 20), indicating that Bptf deletion is not

affecting the proportion of RGCs nor their rate to enter S-phase. Furthermore, neither the basal region nor the apical membrane of the EcKO cortex demonstrated proportional changes in the rate of progenitor cells entering the M-phase (Figure 22), suggesting that the IPCs and RGCs are both able to enter the M-phase in similar proportions. There are then two possibilities; there could be an increase in the proportion of IPCs entering apoptosis or there could be a diminished proliferative trait in the IPC cell cycle progression. As demonstrated in Figure 41, there is no significant change in the proportion of cells in the VZ / IZ of E15.5 mice entering apoptosis, suggesting that the decreased proportion of IPCs is not arising due to an increase in cell death. However, the EdU/Ki67 double staining assay did demonstrate that there is a 10% reduction in the proportion of EcKO progenitor cells exiting cell cycle after 24 hours (EdU+ & Ki67- / EdU+; Figure 23), when compared to WT and Het littermates. Overall, the progenitor cells of the EcKO, Het and WT littermates are entering S-phase and M-phase at similar rates yet, the EcKO progenitor pool demonstrate an inability to complete the cell cycle after 24-hrs. Previous research has also demonstrated that human melanoma cell lines with ablated *BPTF*, display an inability to complete the G1/G0 stage, which led to a delayed cell cycle (94). Separately, the Myc oncogene a master regulator of cellular proliferation, differentiation and apoptosis has been demonstrated to form a complex with Bptf, in order to ensure Myc binding and its interaction with its target promoters (89). Through the use of Myc-estrogen receptor (Myc-ER) cells, for selective activation of Myc, Richart *et al*. (89) demonstrated that without Bptf, Myc-ER cells are significantly delayed in their S-phase progression. Furthermore, Myc has been demonstrated to directly bind to the promoter region of a protein called: cell division control protein a 7 (Cdca7), a protein with its highest expression during G1 and S (114, 115). Both of these major cell cycle regulatory genes are deregulated in our RNA-seq data, *Myc* is downregulated (L2FC = -0.73; s-val = $4.32*10^{-5}$; Appendix Table 10), while *Cdc7a* is upregulated (L2FC = 0.72; s-val = $8.82*10^{-}$

[5]; Appendix Table 9). This suggests that the lack of Bptf and its interaction with Myc, failed to regulate Cdc7a gene expression. This pathway serves as a possible starting point to investigate the origins of the prolonged cell cycle in the progenitor cells of our EcKO mice. Overall, Bptf is essential for progenitor cells to normally progress through their cell cycle as well as, deletion of *Bptf* leads to a decrease proportion of IPCs, contributing to the cortical hypoplasia displayed solely by the EcKO mice.

Future steps are needed to determine what is the specific role of Bptf in progenitor cell cycle kinetics. Is Bptf, with NURF, displacing nucleosomes for chromosome condensation or for the regulation of key genes involved in cell cycle progression? Accurate determination of Bptf specific target genes during embryonic development, around E13.5 – 15.5, should highlight the proteins involved in IPC proliferation and differentiation. *Foxg1* has previously been shown to be a target of ISWI Snf2l and Sn2h proteins as well as essential for normal IPC proliferation (79, 80, 116). Furthermore, Foxg1 has also been associated with the transition of progenitor pool differentiation from layer I neurons to the production of early-born layer VI neurons (7). RT-qPCR from E15.5 forebrain specific tissue demonstrated that there was no significant decrease (L2FC = -3.8; p-val = 0.0636; n = 3; unpaired t-test) in the expression of *Foxg1* between WT and EcKO mice (Appendix Figure 44). Similarly, at E13.5 Foxg1 IF staining demonstrated there is no significant decrease in the CP or VZ/IZ proportions of Foxg1 positively stained neurons (Figure 37). Furthermore, *Foxg1* was also not deregulated in the P0 RNA-seq differential expression analysis, nor was it differentially expressed in the RT-qPCR validation (Figure 35C). Further studies are needed to clarify the direct or indirect interactions occurring between Bptf and Foxg1 during early neurogenesis (E13.5 – E15.5), if any, to provide a link between ISWI subunit and

Bptf regulation of IPCs. Perhaps the ISWI Snf2l and Snf2h subunits are interacting with Foxg1 through a different complex and not through the NURF complex.

4.2. *Bptf* is essential for the production of Foxp1+ and Ctip2+ layer IV and layer V neurons

The murine neocortex can be divided into 6 layers, each layer is then divergent from one another based on patterns of gene expression, cell type, connectivity and developmental timings. Pyramidal neurons are located in layer V and are known to send their projections to the spinal cord, hindbrain and the midbrain (117). Primarily they are characterized by the expression of *Fezf2* and *Ctip2*. Previous mouse KO experiments demonstrated that without *Fezf2* expression, deep-layer neurons are generated but, with an aberrant axonal growth as well as an absent expression of *Ctip2* (117). Conversely, *Ctip2* KO mice develop aberrant axonal growth, demonstrating a lack of axons reaching from layer V to the spinal cord (8). Our analysis of P2 cortical lamination of WT and EcKO mice demonstrated no change in the proportion of late-born Satb2+ neurons (mainly Layers II/III), nor in the proportion of early-born Tbr1+ neurons (layer VI, Figures 24-25). Regardless, by P2 there was significantly (~50%) fewer Ctip2 positive layer V neurons in the EcKO cortex when compared to its WT and Het littermates (Figures 24, 25, 27). Similarly, there is also a significant ~40% reduction of Foxp1+ layer IV neurons (Figure 26). This clearly suggests Bptf is essential for the differentiation and proper TF expression of layers IV and V neurons. As previous experiments demonstrate, *Fezf2* expression is required for normal *Ctip2* expression (117). Interestingly, our P0 EcKO mice also have a reduced *Fezf2* expression (L2FC = -.93, s-val = $2.01*10^{-13}$) in the RNA-seq data (Appendix Table 10) and confirmed by RT-qPCR (L2FC = -2.26, p-val = 0.0002, Figure 33). This suggests that Bptf indirectly or directly regulates the expression of *Fezf2* and with its reduced levels, layer V neurons are unable

to adequately express *Ctip2*. However, we cannot rule out that Bptf can also be directly regulating *Ctip2* expression.

Future steps should verify direct interactions of Bptf with either *Fezf2, Ctip2* and *Foxp1*. Through chromatin immunoprecipitation (ChIP) assays from cortical lysates using a functional αBptf antibody, direct interactions can be stablished onto the promoter regions of the aforementioned genes. Therefore, in order to verify the reason behind the diminished Layer V, Ctip2 positive neurons, the next step should be to generate a functional αBptf antibody and, clarify the link between these transcription factors and Bptf.

NeuroD6 is a basic helix-loop-helix (bHLH) transcription factor, which is downstream of the proneural gene, *Neurog2* (118). *NeuroD6* (also known as Nex) has been demonstrated to be expressed predominantly in the cortex of the mouse (also observed in the hippocampus and cerebellum) since E12.5, with its peak in mRNA expression shortly after birth, from P0 – P5 (119). Similarly, research performed by Bormuth et al. (118) demonstrates that *NeuroD6* expression begins in the SVZ in IPCs committed for the pyramidal neuron lineage. Altogether, considering that *NeuroD6* expression is stronger in post-natal mice and observed to be more predominant in the cortical plate and absent in the VZ, Schwab et al. (119) argue that the role for NeuroD6 is mostly focused on the differentiation of committed post-mitotic neurons rather than the proliferation of progenitor cells. Our RNA-seq expression analysis (L2FC = -1.002 , s-val = $1.69*10^{-10}$, Appendix Table 10) and RT-qPCR validation (L2FC = -1.76, p-val = 0.0047, Figure 33) demonstrated that *NeuroD6* is downregulated in homozygous mutants. This suggests that Bptf is indirectly/directly regulating *NeuroD6* expression. Considering that Neurog2 regulates *NeuroD6* expression and it is a major proneural gene (1), we also checked for its protein expression. The IF analysis demonstrated that at E13.5 there was no change in Neurog2 protein

levels, observed in cortical sections of EcKO. Opposingly, *Neurog2* transcript levels were upregulated at P0 as denoted by the RNA-seq expression analysis (L2FC = 0.77; s-val = 7.14*10-5; Appendix Table 9), yet not validated by RT-qPCR. Therefore, results suggest that Bptf could be regulating *Neurog2* expression later than by E13.5 yet, its effect on NeuroD6 has not been demonstrated. It is possible that Bptf remodels Neurog2 binding sites within regulatory elements of *NeuroD6* or, that *Neurog2* expression is in fact regulated by Bptf but at a later timepoint. Neurog2 is a critical proneural TF which, for now, seems to be loosely associated with Bptf and, its downstream TF target is in fact deregulated by *Bptf* ablation. Considering the relevance of this pathway for neuronal development, this is suggested to be another possible route by which Bptf regulates early forebrain development.

Future steps need to clarify the relationship between Bptf, NeuroD6 and Neurog2 as well as, to verify if Bptf directly or indirectly regulates their expression. ChIP-seq experiments could demonstrate if there are functional interactions between Bptf and the promoter/regulatory regions of either *Neurog2* and/or *NeuroD6*. Once direct interactions have been established, further functional inferences can then be made when backed up by the RNA-seq and RT-qPCR validations.

4.3. Bptf excision leads to increased neuronal cell death triggering the increased presence of cortical microglia

Apoptosis is an extremely complex process that can arise due to a plethora of cell intrinsic and extrinsic mechanisms. During early development, mitotic progenitor and precursor cells as well as post-mitotic differentiated neurons can undergo apoptosis. Programmed cell death is essential to maintain accurate circuitry within neuronal populations, for example there is a need to eliminate neurons which have migrated to erroneous locations as well as, eliminate

overpopulated neuronal sites (120). Regardless, mature post-mitotic neurons need to maintain axonal circuitry and are therefore required to be long-lived cells, which means a reduction in the neuronal cell death in post-development CNS (120). The birthdating experiment (Figure 27), in which EdU was injected into E13.5 mice followed by pup collection at P2, demonstrates that there is a ~50% decrease in the proportion of EdU stained cells in the cortex of the EcKO mice. This suggests that there is either a decrease in the proportion of progenitors in S-phase at E13.5 or, that there is an increase in cell death occurring from E13.5 to P2, after they have incorporated EdU. The 1-hour and 24-hour EdU staining experiments demonstrate that between E14.5 and E15.5 there is no change in the proportion of proliferating (S-phase) cells (Figures 20, 21, 23), suggesting that the ~50% reduction observed at P2 is most likely a result of neuronal cell death. Furthermore, there is an increase in the proportion of apoptotic events within the cortical plate of E15.5 mice. The WT and Het littermates have ~ 0.2% neuronal cell death while the EcKO display ~ 2%, a striking near 10-fold increase (Figure 41). By P2 (figure 42), the EcKO cortex maintains similar proportions of apoptotic events, ~ 1.7%. Last, by P7 the cortical EcKO CC3 signal is reduced to comparable levels to the Het and WT counterparts (Figure 43). The accumulative experiments suggest that the continuous rate of post-mitotic differentiated neuronal cell death occurring in the cortical plate of the EcKO mice is arising due to the removal of *Bptf*. In comparison, previous *Fezf2*$^{-/-}$ mutant mice, demonstrated an increase neuronal cell death occurring at P1 in the developing amygdala (121). *NeuroD6* (NEX)$^{-/-}$ and *NeuroD2*$^{-/-}$ DKO mutant mice also demonstrated increased neuronal cell death in the developing dentate gyrus at P2 (122). Both authors argue that the decrease expression of these TFs (Fezf2 and NeuroD6), both downregulated in our mouse model (Figure 33), lead to an increase cell death of their corresponding committed immature neurons due to the deregulated neuronal gene pathways. Furthermore, conditional removal of the BAF chromatin remodelling complex, by *Emx1* Cre, led

to the increase in cell death observed in RGCs at E14.5 and ultimately led to a practically non-existent cortex in the mutant mice (37). The authors argue that the removal of the BAF chromatin remodelling complex causes global epigenetic changes that restrict normal cellular processes such as replication, cell cycle progression, and neuronal differentiation. Similar to what is observed in our EcKO model, when *Bptf* is removed, we observe an altered cell cycle progression and a deregulation of key TF which prevent for specific cell fate pathways to take place. Although the exact mechanism is not yet defined, our data suggests that the accumulation of deregulated neuronal specific gene pathways prevent committed neurons from accurately differentiating, leading to the increased cell death observed.

The increase in apoptosis is leading to a major rise in microglia observed in the cortical sections of the EcKO mice. At E15.5 there is a significant doubling (from 1% to 2%) in the proportions of microglia observed in the VZ/IZ of the EcKO cortex, when compared solely to the WT littermates. Furthermore, by P2, the EcKO cortex demonstrates a near 10-fold increase in the proportions of microglia (from 0.46% in WT, 0.3% in Hets to 3.4% in EcKO, Figure 42). As demonstrated in Figure 42, the microglia are observed to be engulfing the CC3 marker, and ~20% of the microglia are co-labelled with the apoptotic marker. By P7, the levels of microglia in the EcKO mutant cortex remain higher than that of the Het and WT counterparts (Figure 43). Furthermore, it is mentioned in the literature that microglia change their structure based on the function they are performing (16). In Figure 42, the structure of the microglia is different when comparing that of the EcKO cortex against the WT and Het littermates. The EcKO cortical microglia are more round, “full” and less ramified; this structure is mentioned to be of an activated microglia towards a macrophage phenotype (16). Furthermore, in the WT and Het cortical sections, the microglia have a sparse arborization-like structure, argued to be a ramified

state in which the microglia are monitoring the microenvironment of a healthy brain (16). Microglia originate from hematopoietic progenitors and are observed entering the brain by E 9.5 (15). They do not arise from neuronal progenitors like neurons, astrocytes or oligodendrocytes and therefore are not expected to express *Emx1*. Consequently, *Bptf* is expected, yet not verified, to be expressed in normal levels in hematopoietic progenitors, removing the possibility for the increase in microglia to be a direct effect of *Bptf* loss. It is therefore suggested that the increase in apoptosis in the cortical plate at E15.5 is leading to the localization, activation and surge of microglia observed in the P2 mice and maintained in the P7 EcKO mutant cortices.

4.4. ISWI Snf2l and Snf2h and the NURF complex

As mentioned in the introductory section (ISWI proteins), Snf2l and Snf2h are the ATPase subunits of the ISWI sub-family of chromatin remodelers. More specifically, Snf2l (*Smarca1*) has been demonstrated to interact with Bptf and pRbap46/48 to form the NURF complex in order to displace nucleosomes mainly in the promoter region of target genes, modulating TF accessibility (63, 71, 73–75). Previous studies have demonstrated that in the cerebellum of the mice, when *Smarca5* is conditionally removed, *Smarca1* compensates for the loss and becomes upregulated (123). Regardless, in our EcKO model, there was no measurable distinction in gene expression levels of either *Smarca1* or *Smarca5* (encoding Snf2l or Snf2h, respectively) at the RNA level, either at E15.5 (p-val = 0.15 and p-val = 0.054, respectively, Appendix Figure 45) or at P0 (Figure 34). Similarly, neither of the ISWI subunits was discovered to be deregulated in the RNA-seq expression data. This suggests that the ISWI ATPase expression levels are not affected by the removal of *Bptf* in the cortex.

Conditional inactivation of *Smarca1* in the cortex of the mouse, yielded macrocephalic animals due to an increase in progenitor cell proliferation (79). Opposingly, conditional removal

of *Smarca5* in the cortex of a separate mouse model, led to significant cortical hypoplasia within the *Smarca5::Emx1* cKO animals due to a decrease proportion of IPCs in the developing cortex (Appendix Figure 46, (80)). From simple observation, the cortical hypoplasia displayed by the *Smarca5* cKO is not nearly as drastic as the hypoplasia displayed here, by the *Bptf* EcKO mice (Figure 12). How is it possible that the removal of each interchangeable ATPase subunit leads to an opposing outcome? Similarly, how can the deletion of *Bptf* further exacerbate the phenotype observed only when *Smarca5* is removed and, not the phenotype observed by the removal of *Smarca1*? Based on the protein similarities between the two ISWI homologs it is possible to consider that both ATPase subunits can interchange between complexes, as argued by an in-vitro study demonstrating exactly the interchange of both subunits with all regulatory ISWI proteins (Bptf included, [66]). By removing *Bptf*, we have prevented both Snf2l and Snf2h from interacting with the global target promoter regions of NURF, ensuring neither of these proteins will compensate for the lose of the other. In that regard, the data does back the notion that the conditional removal of *Bptf* leads to a more aggravated phenotype than the one observed by the conditional removal of either *Smarca5* or *Smarca1* alone.

ISWI mammalian complexes (CHRAC, ACF, WHICH, RSF, NoRC, NURF and CERF) have all been demonstrated to be expressed during cortical neurogenesis (35, 44). If the ISWI ATPase subunits can in fact interchange between complexes as described by Oppikofer et al. (66), hypothetically, it is then possible for ISWI complexes to compensate for the loss of NURF, due to shared gene target overlap. Future work performed by the Picketts' group will characterize the simultaneous removal of both *Smarca5* and *Smarca1* in the developing cortex. It is believed that the removal of both ATPase subunits should aggravate or at least assimilate the phenotype observed by the removal of *Bptf*. Future steps will be aimed to clearly differentiate between the

removal of the complex, and the removal of the ATPase subunits. This should help to clarify if there are any ISWI complex compensation as well as, clarify the role of the ATPase subunits apart from the NURF complex and vice versa.

4.5. Assessing the *Bptf* Emx1 cKO mice as a models of the NEDDFL syndrome

The *Nestin* gene codes for an intermediate filament present in neuroepithelial precursor cells and it is a common marker for neural stem cells present in the development of the CNS (97). Therefore, it can be speculated that the NcKO animals are lacking normal expression of the *Bptf* gene in the entire developing CNS. Our initial viability assessment suggests that there are no NcKO animals that can survive past birth. Eight out of the ten NcKO genotyped mice were born dead while the remaining two died shortly after collection (Table 4, Figure 7). Four separate litters were observed, all of which did not contain a single viable NcKO mutant (data not shown). Separately, Snf2h a binding partner of Bptf and a possible ATPase subunit of the NURF complex was also conditionally inactivated with *Nestin* Cre by Alvarez-Saavedra et al. (123). These mice demonstrated *Nestin* expression in the entire CNS from the entire brain, until the end of the spinal cord. Here, we speculate that the NcKO mice are also experiencing such alterations, in which the functional Bptf protein is absent in the entire CNS, causing the pups to die prematurely. Furthermore, Nissl stained sagittal brain sections of embryonic (E18.5) WT and NcKO littermates (Figure 8) demonstrate the hypoplastic brain of the NcKO animals. The NcKO mice were bred in parallel with the EcKO mouse model, considering the premature death and lack of viable NcKO mice alongside the drastic cortical hypoplasia of the EcKO mice; it was decided to, for the purpose of this thesis, focus on the EcKO mouse model. There is still a need to characterize the heterozygote *Nestin* cre mice. It is possible these mice will carry more subtle

differences compared to WT littermates, similar to those from the NEDDFL human patients. Future work should be aimed at characterizing the *Nestin* Het mice, using the EcKO model presented here, as a base in which to compare cortical differences. Taking into consideration that it is possible for no changes to occur within the *Nestin* Het mice, as demonstrated by Landry et al. (88), global *Bptf* KO embryos die post implantation at day ~E8.5, while the global Het mice survive. Perhaps the mice do not suffer from haploinsufficiency deficits as humans do.

The *Emx1* gene codes for a transcription factor expressed in the progenitor cells and the postmitotic neurons of the developing murine telencephalon (99). *Bptf* exon 2 is successfully excised in the neocortex of the EcKO brain (Figure 16, 18 – 19), while the remainder of the brain does express *Bptf* similarly to WT and Het littermates (Figure 17). As mentioned by Landry et al. (88), the conditional removal of exon 2 leads to out of frame transcripts behaving as null alleles. It can then be assumed that the EcKO animals have two null *Bptf* alleles solely in the neocortex, while the Het littermates have only one null *Bptf* allele (Figure 16). By P0, the EcKO brain is significantly smaller than the WT counterparts and, by P2 the body weight of the EcKO mice decreases (from ~1.67 in WT to ~1.4 grams in the EcKO, Figure 10D), which highlights possible lack of feeding capabilities or rejection by the mother. As seen in comparative Nissl stained coronal sections (Figures 13 – 15) and in normal representative brain comparison (Figure 12), solely the neocortex of the EcKO is reduced in size. Regardless, the EcKO mice are born at normal mendelian ratios (Table 6) and were observed to survive until 9 months of age (Figure 9).

One major caveat is that the majority of the human NEDDFL patients are haploinsufficient for BPTF, while the $Bptf^{f/+}$ :: $Emx1Cre^{+/-}$ Het mice do not seem to demonstrate any physiological changes, or obvious changes in cortical size (Figures 13 – 15). The RGCs and IPCs were not proportionally altered (Figures 20 – 21), the layer markers were not significantly

different (Figures 24 – 25) and the RT-qPCR did not demonstrate similar expression patterns to the validated deregulated genes of the EcKO littermates. Regardless, behavioural analyses are required to define if there are any changes arising due to the homozygous or Het conditional removal of *Bptf* exon 2. For example, the Morris water maze can be used to test spatial learning and memory while the open field and the elevated plus-maze can be used to test behavioural anxiety (124, 125). These future experiments will demonstrate any distorted behaviour arising due to the significantly reduced cortex in the EcKO mice and will also highlight if there are any more subtle changes in the *Emx1* Het mice that were not identified by the characterization within this thesis. To this battery of behavioural tests, the *Nestin* Het mice can also be added, in order to determine possible behavioural differences that may replicate some of the behavioural alterations displayed by the human NEDFFL patients, taking into consideration that the *Nestin* Het mice represent a closer model to the human patients. Second, there is still a crucial need to create antibodies specific to the Bptf protein. Using a newly designed αBptf antibody and simple western blot analysis, we will be able to demonstrate and quantify the amounts of protein removed in the EcKO cortex comparing them to Het and WT levels.

Overall, the *Bptf* Emx1 cKO mice represent a good model to understand the role of Bptf in the developing murine neocortex, and to replicate some of the characteristics displayed by the human NEDDFL patients. Most importantly, almost all the eleven human NEDDFL patients described in the introduction section 1.6, displayed microcephalic features, also observed by the extremely hypoplastic neocortex of the EcKO mice. The distal limb and facial anomalies cannot be assessed by the EcKO model, since *Bptf* is only conditionally removed in the neocortex. Furthermore, behavioral tests will demonstrate if the mouse model will recapitulate some of the intellectual disabilities and anxiety-like behaviours of the NEDDFL patients. Regardless, the DO

analysis shines a positive light in this regard, considering the majority of the downregulated genes were associated with human mental health disease, mood disorder and cognitive disorder (Figure 39). Separately, *Nr4a2*, encoding a cortical TF, was one of the downregulated genes in the RNA-seq expression data (L2FC = -1.01, s-val = $9.49*10^{-9}$, Appendix Table 10) and also validated to be downregulated through RT-qPCR (L2FC = -1.82, p-val = 0.005, Figure 33). According to Levy et al. (110) human haploinsufficiency of *Nr4a2* leads to a neurodevelopmental disorder and autism spectrum disorder. Furthermore, *Nr4a2* has been shown to be expressed in hippocampal neurons as well as in the cortex and it was demonstrated in the mouse to be essential for long-term memory as well as, object location and recognition (126), further supporting the effect of *Bptf* removal in NDD and IDD. These results further support the possibility for mutant mice to demonstrate behavioural differences and strengthen the reasoning to expand future research.

Bptf has been demonstrated to be essential for IPC progenitor expansion, cortical Layer V neuronal formation, prevention of early neuronal cell death and, when conditionally removed by *Emx1* Cre, recapitulates one of the major characteristics of the human NEDDFL patients, namely microcephaly.

5. References

1. Adnani L, Han S, Li S, Mattar P, Schuurmans C. 2018. Mechanisms of Cortical Differentiation, p. 223–320. *In* International Review of Cell and Molecular Biology. Elsevier.
2. Copp AJ, Greene NDE, Murdoch JN. 2003. The genetic basis of mammalian neurulation. Nat Rev Genet 4:784–793.
3. Rossant J, Tam PPL. 2004. Emerging Asymmetry and Embryonic Patterning in Early Mouse Development. Developmental Cell 7:155–164.
4. Cecchi C, Boncinelli E. 2000. Emx homeogenes and mouse brain development. Trends in Neurosciences 23:347–352.
5. Wilkinson G, Dennis D, Schuurmans C. 2013. Proneural genes in neocortical development. Neuroscience 253:256–273.
6. Seo S, Lim J-W, Yellajoshyula D, Chang L-W, Kroll KL. 2007. Neurogenin and NeuroD direct transcriptional targets and their regulatory enhancers. EMBO J 26:5093–5108.
7. Cargnin F, Kwon J-S, Katzman S, Chen B, Lee JW, Lee S-K. 2018. FOXG1 Orchestrates Neocortical Organization and Cortico-Cortical Connections. Neuron 100:1083-1096.e5.
8. Chen B, Wang SS, Hattox AM, Rayburn H, Nelson SB, McConnell SK. 2008. The Fezf2-Ctip2 genetic pathway regulates the fate choice of subcortical projection neurons in the developing cerebral cortex. Proceedings of the National Academy of Sciences 105:11382–11387.
9. Krishna-K K, Hertel N, Redies C. 2011. Cadherin expression in the somatosensory cortex: evidence for a combinatorial molecular code at the single-cell level. Neuroscience 175:37–48.
10. Agmon A, Yang L, O'Dowd D, Jones E. 1993. Organized growth of thalamocortical axons from the deep tier of terminations into layer IV of developing mouse barrel cortex. J Neurosci 13:5365–5382.
11. Li X, Xiao J, Fröhlich H, Tu X, Li L, Xu Y, Cao H, Qu J, Rappold GA, Chen J-G. 2015. Foxp1 Regulates Cortical Radial Migration and Neuronal Morphogenesis in Developing Cerebral Cortex. PLoS ONE 10:e0127671.
12. Fame RM, MacDonald JL, Macklis JD. 2011. Development, specification, and diversity of callosal projection neurons. Trends in Neurosciences 34:41–50.
13. Cubelos B, Briz CG, Esteban-Ortega GM, Nieto M. 2015. Cux1 and Cux2 selectively target basal and apical dendritic compartments of layer II-III cortical neurons. Developmental Neurobiology 75:163–172.
14. Dennis DJ, Wilkinson G, Li S, Dixit R, Adnani L, Balakrishnan A, Han S, Kovach C, Gruenig N, Kurrasch DM, Dyck RH, Schuurmans C. 2017. *Neurog2* and *Ascl1* together regulate a postmitotic derepression circuit to govern laminar fate specification in the murine neocortex. Proc Natl Acad Sci USA 114:E4934–E4943.
15. Tong CK, Vidyadaran S. 2016. Role of microglia in embryonic neurogenesis. Exp Biol Med (Maywood) 241:1669–1675.
16. Xiong X-Y, Liu L, Yang Q-W. 2016. Functions and mechanisms of microglia/macrophages in neuroinflammation and neurogenesis after stroke. Progress in Neurobiology 142:23–44.
17. Gabriele M, Lopez Tobon A, D'Agostino G, Testa G. 2018. The chromatin basis of neurodevelopmental disorders: Rethinking dysfunction along the molecular and temporal axes. Progress in Neuro-Psychopharmacology and Biological Psychiatry 84:306–327.

18. Cobb SR, Davies CH. 2013. Neurodevelopmental disorders. Neuropharmacology 68:1.
19. Kochinke K, Zweier C, Nijhof B, Fenckova M, Cizek P, Honti F, Keerthikumar S, Oortveld MAW, Kleefstra T, Kramer JM, Webber C, Huynen MA, Schenck A. 2016. Systematic Phenomics Analysis Deconvolutes Genes Mutated in Intellectual Disability into Biologically Coherent Modules. The American Journal of Human Genetics 98:149–164.
20. LaSalle JM. 2013. Autism genes keep turning up chromatin. OA Autism 1:14.
21. Piovesan A, Pelleri MC, Antonaros F, Strippoli P, Caracausi M, Vitale L. 2019. On the length, weight and GC content of the human genome. BMC Res Notes 12:106.
22. Venkatesh S, Workman JL. 2015. Histone exchange, chromatin structure and the regulation of transcription. Nat Rev Mol Cell Biol 16:178–189.
23. Tyagi M, Imam N, Verma K, Patel AK. 2016. Chromatin remodelers: We are the drivers!! Nucleus 7:388–404.
24. 2018. Molecular Motors: Methods and Protocols. Springer New York, New York, NY.
25. Fyodorov DV, Zhou B-R, Skoultchi AI, Bai Y. 2018. Emerging roles of linker histones in regulating chromatin structure and function. Nat Rev Mol Cell Biol 19:192–206.
26. Haberland M, Montgomery RL, Olson EN. 2009. The many roles of histone deacetylases in development and physiology: implications for disease and therapy. Nat Rev Genet 10:32–42.
27. Tessarz P, Kouzarides T. 2014. Histone core modifications regulating nucleosome structure and dynamics. Nat Rev Mol Cell Biol 15:703–708.
28. Hyun K, Jeon J, Park K, Kim J. 2017. Writing, erasing and reading histone lysine methylations. Exp Mol Med 49:e324–e324.
29. Santos-Rosa H, Schneider R, Bannister AJ, Sherriff J, Bernstein BE, Emre NCT, Schreiber SL, Mellor J, Kouzarides T. 2002. Active genes are tri-methylated at K4 of histone H3. Nature 419:407–411.
30. Talbert PB, Henikoff S. 2017. Histone variants on the move: substrates for chromatin dynamics. Nat Rev Mol Cell Biol 18:115–126.
31. Bjornsson HT. 2015. The Mendelian disorders of the epigenetic machinery. Genome Res 25:1473–1481.
32. Zhang P, Torres K, Liu X, Liu C, Pollock RE. 2016. An Overview of Chromatin-Regulating Proteins in Cells. Curr Protein Pept Sci 17:401–410.
33. Hota SK, Bruneau BG. 2016. ATP-dependent chromatin remodeling during mammalian development. Development 143:2882–2897.
34. Lai WKM, Pugh BF. 2017. Understanding nucleosome dynamics and their links to gene expression and DNA replication. Nat Rev Mol Cell Biol 18:548–562.
35. Goodwin LR, Picketts DJ. 2018. The role of ISWI chromatin remodeling complexes in brain development and neurodevelopmental disorders. Molecular and Cellular Neuroscience 87:55–64.
36. Dechassa ML, Zhang B, Horowitz-Scherer R, Persinger J, Woodcock CL, Peterson CL, Bartholomew B. 2008. Architecture of the SWI/SNF-Nucleosome Complex. Molecular and Cellular Biology 28:6010–6021.
37. Narayanan R, Pirouz M, Kerimoglu C, Pham L, Wagener RJ, Kiszka KA, Rosenbusch J, Seong RH, Kessel M, Fischer A, Stoykova A, Staiger JF, Tuoc T. 2015. Loss of BAF (mSWI/SNF) Complexes Causes Global Transcriptional and Chromatin State Changes in Forebrain Development. Cell Reports 13:1842–1854.

38. Nguyen H, Kerimoglu C, Pirouz M, Pham L, Kiszka KA, Sokpor G, Sakib MS, Rosenbusch J, Teichmann U, Seong RH, Stoykova A, Fischer A, Staiger JF, Tuoc T. 2018. Epigenetic Regulation by BAF Complexes Limits Neural Stem Cell Proliferation by Suppressing Wnt Signaling in Late Embryonic Development. Stem Cell Reports 10:1734–1750.

39. Tsurusaki Y, Okamoto N, Ohashi H, Kosho T, Imai Y, Hibi-Ko Y, Kaname T, Naritomi K, Kawame H, Wakui K, Fukushima Y, Homma T, Kato M, Hiraki Y, Yamagata T, Yano S, Mizuno S, Sakazume S, Ishii T, Nagai T, Shiina M, Ogata K, Ohta T, Niikawa N, Miyatake S, Okada I, Mizuguchi T, Doi H, Saitsu H, Miyake N, Matsumoto N. 2012. Mutations affecting components of the SWI/SNF complex cause Coffin-Siris syndrome. Nat Genet 44:376–378.

40. Neale BM, Kou Y, Liu L, Ma'ayan A, Samocha KE, Sabo A, Lin C-F, Stevens C, Wang L-S, Makarov V, Polak P, Yoon S, Maguire J, Crawford EL, Campbell NG, Geller ET, Valladares O, Schafer C, Liu H, Zhao T, Cai G, Lihm J, Dannenfelser R, Jabado O, Peralta Z, Nagaswamy U, Muzny D, Reid JG, Newsham I, Wu Y, Lewis L, Han Y, Voight BF, Lim E, Rossin E, Kirby A, Flannick J, Fromer M, Shakir K, Fennell T, Garimella K, Banks E, Poplin R, Gabriel S, DePristo M, Wimbish JR, Boone BE, Levy SE, Betancur C, Sunyaev S, Boerwinkle E, Buxbaum JD, Cook Jr EH, Devlin B, Gibbs RA, Roeder K, Schellenberg GD, Sutcliffe JS, Daly MJ. 2012. Patterns and rates of exonic de novo mutations in autism spectrum disorders. Nature 485:242–245.

41. Bultman S, Gebuhr T, Yee D, La Mantia C, Nicholson J, Gilliam A, Randazzo F, Metzger D, Chambon P, Crabtree G, Magnuson T. 2000. A Brg1 Null Mutation in the Mouse Reveals Functional Differences among Mammalian SWI/SNF Complexes. Molecular Cell 6:1287–1295.

42. Wolff D, Endele S, Azzarello-Burri S, Hoyer J, Zweier M, Schanze I, Schmitt B, Rauch A, Reis A, Zweier C. 2012. In-Frame Deletion and Missense Mutations of the C-Terminal Helicase Domain of SMARCA2 in Three Patients with Nicolaides-Baraitser Syndrome. Molecular Syndromology.

43. Koga M, Ishiguro H, Yazaki S, Horiuchi Y, Arai M, Niizato K, Iritani S, Itokawa M, Inada T, Iwata N, Ozaki N, Ujike H, Kunugi H, Sasaki T, Takahashi M, Watanabe Y, Someya T, Kakita A, Takahashi H, Nawa H, Muchardt C, Yaniv M, Arinami T. 2009. Involvement of SMARCA2/BRM in the SWI/SNF chromatin-remodeling complex in schizophrenia. Human Molecular Genetics 18:2483–2494.

44. Sokpor G, Castro-Hernandez R, Rosenbusch J, Staiger JF, Tuoc T. 2018. ATP-Dependent Chromatin Remodeling During Cortical Neurogenesis. Front Neurosci 12:226.

45. McKnight JN, Jenkins KR, Nodelman IM, Escobar T, Bowman GD. 2011. Extranucleosomal DNA Binding Directs Nucleosome Sliding by Chd1. Molecular and Cellular Biology 31:4746–4759.

46. Nitarska J, Smith JG, Sherlock WT, Hillege MMG, Nott A, Barshop WD, Vashisht AA, Wohlschlegel JA, Mitter R, Riccio A. 2016. A Functional Switch of NuRD Chromatin Remodeling Complex Subunits Regulates Mouse Cortical Development. Cell Reports 17:1683–1698.

47. O'Roak BJ, Vives L, Girirajan S, Karakoc E, Krumm N, Coe BP, Levy R, Ko A, Lee C, Smith JD, Turner EH, Stanaway IB, Vernot B, Malig M, Baker C, Reilly B, Akey JM, Borenstein E, Rieder MJ, Nickerson DA, Bernier R, Shendure J, Eichler EE. 2012. Sporadic autism exomes reveal a highly interconnected protein network of de novo mutations. Nature 485:246–250.

48. Disruptive CHD8 Mutations Define a Subtype of Autism Early in Development | Elsevier Enhanced Reader.

49. Sanlaville D. 2005. Phenotypic spectrum of CHARGE syndrome in fetuses with CHD7 truncating mutations correlates with expression during human development. Journal of Medical Genetics 43:211–317.

50. Cao L, Ding J, Dong L, Zhao J, Su J, Wang L, Sui Y, Zhao T, Wang F, Jin J, Cai Y. 2015. Negative Regulation of p21Waf1/Cip1 by Human INO80 Chromatin Remodeling Complex Is Implicated in Cell Cycle Phase G2/M Arrest and Abnormal Chromosome Stability. PLoS ONE 10:e0137411.

51. Poli J, Gasser SM, Papamichos-Chronakis M. 2017. The INO80 remodeller in transcription, replication and repair. Phil Trans R Soc B 372:20160290.

52. Wang L, Du Y, Ward JM, Shimbo T, Lackford B, Zheng X, Miao Y, Zhou B, Han L, Fargo DC, Jothi R, Williams CJ, Wade PA, Hu G. 2014. INO80 Facilitates Pluripotency Gene Activation in Embryonic Stem Cell Self-Renewal, Reprogramming, and Blastocyst Development. Cell Stem Cell 14:575–591.

53. Alazami AM, Patel N, Shamseldin HE, Anazi S, Al-Dosari MS, Alzahrani F, Hijazi H, Alshammari M, Aldahmesh MA, Salih MA, Faqeih E, Alhashem A, Bashiri FA, Al-Owain M, Kentab AY, Sogaty S, Al Tala S, Temsah M-H, Tulbah M, Aljelaify RF, Alshahwan SA, Seidahmed MZ, Alhadid AA, Aldhalaan H, AlQallaf F, Kurdi W, Alfadhel M, Babay Z, Alsogheer M, Kaya N, Al-Hassnan ZN, Abdel-Salam GMH, Al-Sannaa N, Al Mutairi F, El Khashab HY, Bohlega S, Jia X, Nguyen HC, Hammami R, Adly N, Mohamed JY, Abdulwahab F, Ibrahim N, Naim EA, Al-Younes B, Meyer BF, Hashem M, Shaheen R, Xiong Y, Abouelhoda M, Aldeeri AA, Monies DM, Alkuraya FS. 2015. Accelerating Novel Candidate Gene Discovery in Neurogenetic Disorders via Whole-Exome Sequencing of Prescreened Multiplex Consanguineous Families. Cell Reports 10:148–161.

54. Guo D, Duan X-Y, Regalado ES, Mellor-Crummey L, Kwartler CS, Kim D, Lieberman K, de Vries BBA, Pfundt R, Schinzel A, Kotzot D, Shen X, Yang M-L, Bamshad MJ, Nickerson DA, Gornik HL, Ganesh SK, Braverman AC, Grange DK, Milewicz DM. 2017. Loss-of-Function Mutations in YY1AP1 Lead to Grange Syndrome and a Fibromuscular Dysplasia-Like Vascular Disease. The American Journal of Human Genetics 100:21–30.

55. Hood RL, Lines MA, Nikkel SM, Schwartzentruber J, Beaulieu C, Nowaczyk MJM, Allanson J, Kim CA, Wieczorek D, Moilanen JS, Lacombe D, Gillessen-Kaesbach G, Whiteford ML, Quaio CRDC, Gomy I, Bertola DR, Albrecht B, Platzer K, McGillivray G, Zou R, McLeod DR, Chudley AE, Chodirker BN, Marcadier J, Majewski J, Bulman DE, White SM, Boycott KM. 2012. Mutations in SRCAP, Encoding SNF2-Related CREBBP Activator Protein, Cause Floating-Harbor Syndrome. The American Journal of Human Genetics 90:308–313.

56. Sailau ZK, Bogolyubov DS, Bogolyubova IO. 2017. Nuclear distribution of the chromatin-remodeling protein ATRX in mouse early embryogenesis. Acta Histochemica 119:18–25.

57. Gibbons RJ, Picketts DJ, Villard L. Mutations in a Putative Global Transcriptional Regulator Cause X-Linked Mental Retardation with a-Thalassemia (ATR-X Syndrome) 9.

58. Mitson M, Kelley LA, Sternberg MJE, Higgs DR, Gibbons RJ. 2011. Functional significance of mutations in the Snf2 domain of ATRX. Human Molecular Genetics 20:2603–2610.

59. Drane P, Ouararhni K, Depaux A, Shuaib M, Hamiche A. 2010. The death-associated protein DAXX is a novel histone chaperone involved in the replication-independent deposition of H3.3. Genes & Development 24:1253–1265.

60. Ryan DP, Owen-Hughes T. 2011. Snf2-family proteins: chromatin remodellers for any occasion. Current Opinion in Chemical Biology 15:649–656.

61. Lazzaro MA, Picketts DJ. 2001. Cloning and characterization of the murine Imitation Switch (ISWI) genes: differential expression patterns suggest distinct developmental roles for Snf2h and Snf2l. Journal of Neurochemistry 77:1145–1156.

62. Bartholomew B. 2014. ISWI chromatin remodeling: one primary actor or a coordinated effort? Current Opinion in Structural Biology 24:150–155.

63. Barisic D, Stadler MB, Iurlaro M, Schübeler D. 2019. Mammalian ISWI and SWI/SNF selectively mediate binding of distinct transcription factors. Nature 569:136–140.

64. Varga-Weisz PD, Wilm M, Bonte E, Dumas K, Mann M, Becker PB. 1997. Chromatin-remodelling factor CHRAC contains the ATPases ISWI and topoisomerase II. Nature 388:598–602.

65. Hakimi M-A, Bochar DA, Schmiesing JA, Dong Y, Barak OG, Speicher DW, Yokomori K, Shiekhattar R. 2002. A chromatin remodelling complex that loads cohesin onto human chromosomes. Nature 418:994–998.

66. Oppikofer M, Bai T, Gan Y, Haley B, Liu P, Sandoval W, Ciferri C, Cochran AG. 2017. Expansion of the ISWI chromatin remodeler family with new active complexes. EMBO Rep 18:1697–1706.

67. Längst G, Bonte EJ, Corona DFV, Becker PB. 1999. Nucleosome Movement by CHRAC and ISWI without Disruption or trans-Displacement of the Histone Octamer. Cell 97:843–852.

68. Längst G, Becker PB. Nucleosome remodeling by ISWI-containing factors 8.

69. Lopes F, Barbosa M, Ameur A, Soares G, de Sá J, Dias AI, Oliveira G, Cabral P, Temudo T, Calado E, Cruz IF, Vieira JP, Oliveira R, Esteves S, Sauer S, Jonasson I, Syvänen A-C, Gyllensten U, Pinto D, Maciel P. 2016. Identification of novel genetic causes of Rett syndrome- *like* phenotypes. J Med Genet 53:190–199.

70. Karaca E, Harel T, Pehlivan D, Jhangiani SN, Gambin T, Coban Akdemir Z, Gonzaga-Jauregui C, Erdin S, Bayram Y, Campbell IM, Hunter JV, Atik MM, Van Esch H, Yuan B, Wiszniewski W, Isikay S, Yesil G, Yuregir OO, Tug Bozdogan S, Aslan H, Aydin H, Tos T, Aksoy A, De Vivo DC, Jain P, Geckinli BB, Sezer O, Gul D, Durmaz B, Cogulu O, Ozkinay F, Topcu V, Candan S, Cebi AH, Ikbal M, Yilmaz Gulec E, Gezdirici A, Koparir E, Ekici F, Coskun S, Cicek S, Karaer K, Koparir A, Duz MB, Kirat E, Fenercioglu E, Ulucan H, Seven M, Guran T, Elcioglu N, Yildirim MS, Aktas D, Alikaşifoğlu M, Ture M, Yakut T, Overton JD, Yuksel A, Ozen M, Muzny DM, Adams DR, Boerwinkle E, Chung WK, Gibbs RA, Lupski JR. 2015. Genes that Affect Brain Structure and Function Identified by Rare Variant Analyses of Mendelian Neurologic Disease. Neuron 88:499–513.

71. Barak O, Lazzaro MA, Lane WS, Speicher DW, Picketts DJ, Shiekhattar R. 2003. Isolation of human NURF: a regulator of Engrailed gene expression. The EMBO Journal 22:6089–6100.

72. Schwanbeck R, Xiao H, Wu C. 2004. Spatial Contacts and Nucleosome Step Movements Induced by the NURF Chromatin Remodeling Complex. J Biol Chem 279:39933–39941.

73. Alkhatib SG, Landry JW. 2011. The Nucleosome Remodeling Factor. FEBS Letters 585:3197–3207.

74. Goldman JA, Garlick JD, Kingston RE. 2010. Chromatin Remodeling by Imitation Switch (ISWI) Class ATP-dependent Remodelers Is Stimulated by Histone Variant H2A.Z. J Biol Chem 285:4645–4651.

75. Fu Y, Sinha M, Peterson CL, Weng Z. 2008. The Insulator Binding Protein CTCF Positions 20 Nucleosomes around Its Binding Sites across the Human Genome. PLoS Genet 4:e1000138.

76. Qiu Z, Song C, Malakouti N, Murray D, Hariz A, Zimmerman M, Gygax D, Alhazmi A, Landry JW. 2015. Functional Interactions between NURF and Ctcf Regulate Gene Expression. Molecular and Cellular Biology 35:224–237.

77. Wiechens N, Singh V, Gkikopoulos T, Schofield P, Rocha S, Owen-Hughes T. 2016. The Chromatin Remodelling Enzymes SNF2H and SNF2L Position Nucleosomes adjacent to CTCF and Other Transcription Factors. PLoS Genet 12:e1005940.

78. Ohlsson R, Renkawitz R, Lobanenkov V. 2001. CTCF is a uniquely versatile transcription regulator linked to epigenetics and disease. Trends in Genetics 17:520–527.

79. Yip DJ, Corcoran CP, Alvarez-Saavedra M, DeMaria A, Rennick S, Mears AJ, Rudnicki MA, Messier C, Picketts DJ. 2012. Snf2l Regulates Foxg1-Dependent Progenitor Cell Expansion in the Developing Brain. Developmental Cell 22:871–878.

80. Alvarez-Saavedra M, Yan K, De Repentigny Y, Hashem LE, Chaudary N, Sarwar S, Yang D, Ioshikhes I, Kothary R, Hirayama T, Yagi T, Picketts DJ. 2019. Snf2h Drives Chromatin Remodeling to Prime Upper Layer Cortical Neuron Development. Front Mol Neurosci 12:243.

81. Xiao H, Sandaltzopoulos R, Wang H-M, Hamiche A, Ranallo R, Lee K-M, Fu D, Wu C. 2001. Dual Functions of Largest NURF Subunit NURF301 in Nucleosome Sliding and Transcription Factor Interactions. Molecular Cell 8:531–543.

82. Doerks T, Copley R, Bork P. 2001. DDT – a novel domain in different transcription and chromosome remodeling factors. Trends in Biochemical Sciences 26:145–146.

83. Li H, Ilin S, Wang W, Duncan EM, Wysocka J, Allis CD, Patel DJ. 2006. Molecular basis for site-specific read-out of histone H3K4me3 by the BPTF PHD finger of NURF. Nature 442:91–95.

84. Mujtaba S, Zeng L, Zhou M-M. 2007. Structure and acetyl-lysine recognition of the bromodomain. Oncogene 26:5521–5527.

85. Bowser R, Giambrone A, Davies P. 1995. FAC1, a Novel Gene Identified with the Monoclonal Antibody Alz50, Is Developmentally Regulated in Human Brain (Part 1 of 2). DNE 17:20–29.

86. Jordan-Sciutto KL, Dragich JM, Rhodes JL, Bowser R. 1999. Fetal Alz-50 Clone 1, a Novel Zinc Finger Protein, Binds a Specific DNA Sequence and Acts as a Transcriptional Regulator. J Biol Chem 274:35262–35268.

87. Badenhorst P, Voas M, Rebay I, Wu C. 2002. Biological functions of the ISWI chromatin remodeling complex NURF. Genes Dev 16:3186–3198.

88. Landry J, Sharov AA, Piao Y, Sharova LV, Xiao H, Southon E, Matta J, Tessarollo L, Zhang YE, Ko MSH, Kuehn MR, Yamaguchi TP, Wu C. 2008. Essential Role of Chromatin Remodeling Protein Bptf in Early Mouse Embryos and Embryonic Stem Cells. PLoS Genetics 4:e1000241.

89. Richart L, Carrillo-de Santa Pau E, Río-Machín A, de Andrés MP, Cigudosa JC, Lobo VJS-A, Real FX. 2016. BPTF is required for c-MYC transcriptional activity and in vivo tumorigenesis. Nature Communications 7:10153.

90. Wu B, Wang Y, Wang C, Wang GG, Wu J, Wan YY. 2016. BPTF Is Essential for T Cell Homeostasis and Function. The Journal of Immunology 197:4325–4333.

91. Frey WD, Chaudhry A, Slepicka PF, Ouellette AM, Kirberger SE, Pomerantz WCK, Hannon GJ, dos Santos CO. 2017. BPTF Maintains Chromatin Accessibility and the Self-Renewal Capacity of Mammary Gland Stem Cells. Stem Cell Reports 9:23–31.

92. Xu B, Cai L, Butler JM, Chen D, Lu X, Allison DF, Lu R, Rafii S, Parker JS, Zheng D, Wang GG. 2018. The Chromatin Remodeler BPTF Activates a Stemness Gene-Expression Program Essential for the Maintenance of Adult Hematopoietic Stem Cells. Stem Cell Reports 10:675–683.

93. Koludrovic D, Laurette P, Strub T, Keime C, Le Coz M, Coassolo S, Mengus G, Larue L, Davidson I. 2015. Chromatin-Remodelling Complex NURF Is Essential for Differentiation of Adult Melanocyte Stem Cells. PLoS Genet 11:e1005555.

94. Dar AA, Nosrati M, Bezrookove V, de Semir D, Majid S, Thummala S, Sun V, Tong S, Leong SPL, Minor D, Billings PR, Soroceanu L, Debs R, Miller JR, Sagebiel RW, Kashani-Sabet M. 2015. The Role of BPTF in Melanoma Progression and in Response to BRAF-Targeted Therapy. JNCI: Journal of the National Cancer Institute 107.

95. Stankiewicz P, Khan TN, Szafranski P, Slattery L, Streff H, Vetrini F, Bernstein JA, Brown CW, Rosenfeld JA, Rednam S, Scollon S, Bergstrom KL, Parsons DW, Plon SE, Vieira MW, Quaio CRDC, Baratela WAR, Acosta Guio JC, Armstrong R, Mehta SG, Rump P, Pfundt R, Lewandowski R, Fernandes EM, Shinde DN, Tang S, Hoyer J, Zweier C, Reis A, Bacino CA, Xiao R, Breman AM, Smith JL, Katsanis N, Bostwick B, Popp B, Davis EE, Yang Y. 2017. Haploinsufficiency of the Chromatin Remodeler BPTF Causes Syndromic Developmental and Speech Delay, Postnatal Microcephaly, and Dysmorphic Features. The American Journal of Human Genetics 101:503–515.

96. Midro AT, Tommerup N, Borys J, Panasiuk B, Kosztyła-Hojna B, Zalewska R, Konstantynowicz J, Łebkowska U, Cooper L, Scherer SE, Mehrjouy MM, Liu Q, Skowroński R, Stankiewicz P. 2019. Neurodevelopmental disorder with dysmorphic facies and distal limb anomalies syndrome due to disruption of *BPTF* in a 35-year-old man initially diagnosed with Silver-Russell syndrome. Clinical Genetics.

97. Dubois NC, Hofmann D, Kaloulis K, Bishop JM, Trumpp A. 2006. Nestin-Cre transgenic mouse line Nes-Cre1 mediates highly efficient Cre/loxP mediated recombination in the nervous system, kidney, and somite-derived tissues. genesis 44:355–360.

98. Tronche F, Kellendonk C, Kretz O, Gass P, Anlag K, Orban PC, Bock R, Klein R, Schütz G. 1999. Disruption of the glucocorticoid receptor gene in the nervous system results in reduced anxiety. Nat Genet 23:99–103.

99. Gorski JA, Talley T, Qiu M, Puelles L, Rubenstein JLR, Jones KR. 2002. Cortical Excitatory Neurons and Glia, But Not GABAergic Neurons, Are Produced in the Emx1-Expressing Lineage. The Journal of Neuroscience 22:6309–6314.

100. Jensen AM, Wallace VA. Expression of Sonic hedgehog and its putative role as a precursor cell mitogen in the developing mouse retina 9.

101. Wingett SW, Andrews S. 2018. FastQ Screen: A tool for multi-genome mapping and quality control. F1000Res 7.

102. Bolger AM, Lohse M, Usadel B. 2014. Trimmomatic: a flexible trimmer for Illumina sequence data. Bioinformatics 30:2114–2120.

103. Kim D, Langmead B, Salzberg SL. 2015. HISAT: a fast spliced aligner with low memory requirements. Nature Methods 12:357–360.

104. Bray NL, Pimentel H, Melsted P, Pachter L. 2016. Near-optimal probabilistic RNA-seq quantification. Nature Biotechnology 34:525–527.

105. Love MI, Huber W, Anders S. 2014. Moderated estimation of fold change and dispersion for RNA-seq data with DESeq2. preprint, Bioinformatics.

106. Stephens M. 2016. False discovery rates: a new deal. Biostat kxw041.

107. Raudvere U, Kolberg L, Kuzmin I, Arak T, Adler P, Peterson H, Vilo J. 2019. g:Profiler: a web server for functional enrichment analysis and conversions of gene lists (2019 update). Nucleic Acids Research 47:W191–W198.
108. Yu G, Wang L-G, Yan G-R, He Q-Y. 2015. DOSE: an R/Bioconductor package for disease ontology semantic and enrichment analysis. Bioinformatics 31:608–609.
109. Prigent C. 2003. Phosphorylation of serine 10 in histone H3, what for? Journal of Cell Science 116:3677–3685.
110. Lévy J, Grotto S, Mignot C, Maruani A, Delahaye-Duriez A, Benzacken B, Keren B, Haye D, Xavier J, Heulin M, Charles E, Verloes A, Dupont C, Pipiras E, Tabet A-C. 2018. NR4A2 haploinsufficiency is associated with intellectual disability and autism spectrum disorder. Clinical Genetics 94:264–268.
111. Buttgereit A, Lelios I, Yu X, Vrohlings M, Krakoski NR, Gautier EL, Nishinakamura R, Becher B, Greter M. 2016. Sall1 is a transcriptional regulator defining microglia identity and function. Nat Immunol 17:1397–1406.
112. Colombo E, Galli R, Cossu G, Gécz J, Broccoli V. 2004. Mouse orthologue of ARX, a gene mutated in several X-linked forms of mental retardation and epilepsy, is a marker of adult neural stem cells and forebrain GABAergic neurons. Developmental Dynamics 231:631–639.
113. Götz M, Barde Y-A. 2005. Radial Glial Cells. Neuron 46:369–372.
114. Wang H, Ye L, Xing Z, Li H, Lv T, Liu H, Zhang F, Song Y. 2019. CDCA7 promotes lung adenocarcinoma proliferation via regulating the cell cycle. Pathology - Research and Practice 215:152559.
115. Gill RM, Gabor TV, Couzens AL, Scheid MP. 2013. The MYC-Associated Protein CDCA7 Is Phosphorylated by AKT To Regulate MYC-Dependent Apoptosis and Transformation. Mol Cell Biol 33:498–513.
116. Siegenthaler JA, Tremper-Wells BA, Miller MW. 2008. Foxg1 Haploinsufficiency Reduces the Population of Cortical Intermediate Progenitor Cells: Effect of Increased p21 Expression. Cerebral Cortex 18:1865–1875.
117. Chen B, Schaevitz LR, McConnell SK. 2005. Fezl regulates the differentiation and axon targeting of layer 5 subcortical projection neurons in cerebral cortex. Proceedings of the National Academy of Sciences 102:17184–17189.
118. Bormuth I, Yan K, Yonemasu T, Gummert M, Zhang M, Wichert S, Grishina O, Pieper A, Zhang W, Goebbels S, Tarabykin V, Nave K-A, Schwab MH. 2013. Neuronal Basic Helix-Loop-Helix Proteins Neurod2/6 Regulate Cortical Commissure Formation before Midline Interactions. Journal of Neuroscience 33:641–651.
119. Schwab MH, Druffel-Augustin S, Gass P, Jung M, Klugmann M, Bartholomae A, Rossner MJ, Nave K-A. 1998. Neuronal Basic Helix-Loop-Helix Proteins (NEX, neuroD, NDRF): Spatiotemporal Expression and Targeted Disruption of the NEX Gene in Transgenic Mice. J Neurosci 18:1408–1418.
120. Fricker M, Tolkovsky AM, Borutaite V, Coleman M, Brown GC. 2018. Neuronal Cell Death. Physiol Rev 98:68.
121. Hirata-Fukae C, Hirata T. 2014. The zinc finger gene Fezf2 is required for the development of excitatory neurons in the basolateral complex of the amygdala. Developmental Dynamics 243:1030–1036.

122. Schwab MH, Bartholomae A, Heimrich B, Feldmeyer D, Druffel-Augustin S, Goebbels S, Naya FJ, Zhao S, Frotscher M, Tsai M-J, Nave K-A. 2000. Neuronal Basic Helix-Loop-Helix Proteins (NEX and BETA2/Neuro D) Regulate Terminal Granule Cell Differentiation in the Hippocampus. J Neurosci 20:3714–3724.

123. Alvarez-Saavedra M, De Repentigny Y, Lagali PS, Raghu Ram EVS, Yan K, Hashem E, Ivanochko D, Huh MS, Yang D, Mears AJ, Todd MAM, Corcoran CP, Bassett EA, Tokarew NJA, Kokavec J, Majumder R, Ioshikhes I, Wallace VA, Kothary R, Meshorer E, Stopka T, Skoultchi AI, Picketts DJ. 2014. Snf2h-mediated chromatin organization and histone H1 dynamics govern cerebellar morphogenesis and neural maturation. Nature Communications 5.

124. Vorhees CV, Williams MT. 2006. Morris water maze: procedures for assessing spatial and related forms of learning and memory. Nat Protoc 1:848–858.

125. Carola V, D'Olimpio F, Brunamonti E, Mangia F, Renzi P. 2002. Evaluation of the elevated plus-maze and open-field tests for the assessment of anxiety-related behaviour in inbred mice. Behavioural Brain Research 134:49–57.

126. McNulty SE, Barrett RM, Vogel-Ciernia A, Malvaez M, Hernandez N, Davatolhagh MF, Matheos DP, Schiffman A, Wood MA. 2012. Differential roles for Nr4a1 and Nr4a2 in object location vs. object recognition long-term memory. Learn Mem 19:588–592.

127. Aihara, T et al. "Cloning and mapping of SMARCA5 encoding hSNF2H, a novel human homologue of Drosophila ISWI." *Cytogenetics and cell genetics* vol. 81,3-4 (1998): 191-3. doi:10.1159/000015027

128. Tanner RM, Stanford WL, Perkins TJ (2020). *ExCluster: ExCluster robustly detects differentially expressed exons between two conditions of RNA-seq data, requiring at least two independent biological replicates per condition*. R package version 1.6.0.

129. Tsukiyama, T, and C Wu. "Purification and properties of an ATP-dependent nucleosome remodeling factor." Cell vol. 83,6 (1995): 1011-20. doi:10.1016/0092-8674(95)90216-3.

130. Suzuki, S., Nozawa, Y., Tsukamoto, S., Kaneko, T., Manabe, I., Imai, H., and Minami, N. (2015). CHD1 acts via the Hmgpi pathway to regulate mouse early embryogenesis. Development 142, 2375–2384.

131. O'Shaughnessy-Kirwan, A., Signolet, J., Costello, I., Gharbi, S., and Hendrich, B. (2015). Constraint of gene expression by the chromatin remodelling protein CHD4 facilitates lineage specification. Development 142, 2586–2597.

6. Appendix

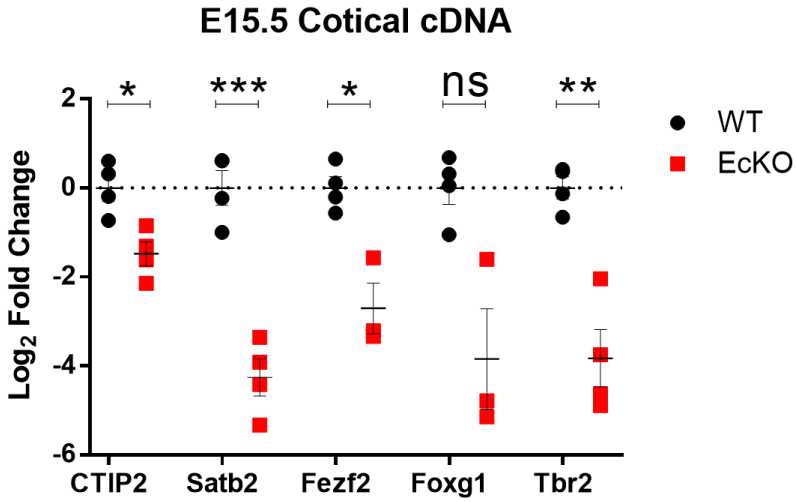

Figure 44 **E15.5 cortical RT-qPCR.**
Quantification of L2FC between WT and EcKO cortical cDNA samples, comparing *Ctip2*, *Satb2* and *Tbr2* (n = 4) as well as *Fezf2* and *Foxg1* (n = 3) transcripts expression. unpaired t-test, *** = p-val < 0.005, ** = pval < 0.01, * = p-val < 0.05, ns = not significant.

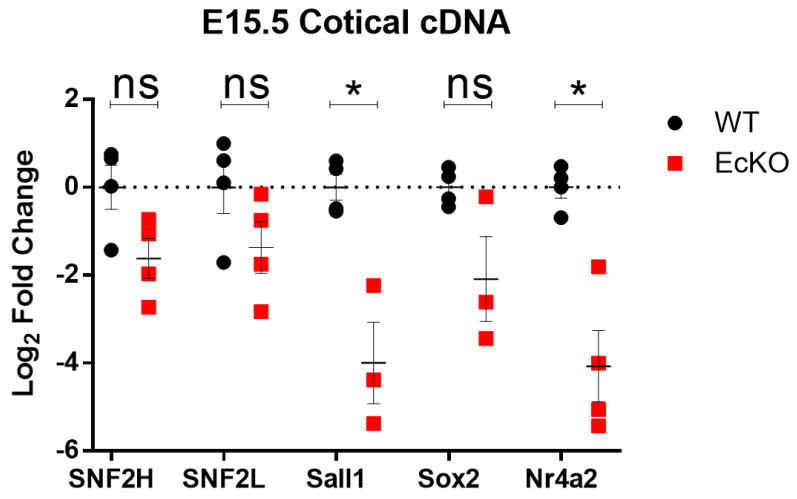

Figure 45 **E15.5 cortical RT-qPCR.**
Quantification of L2FC between WT and EcKO cortical cDNA samples, comparing *Snf2l*, *Snf2h* and *Nr4a2* (n = 4) as well as *Sall1* and *Sox2* (n = 3) transcripts expression. unpaired t-test, * = p-val < 0.05, ns = not significant.

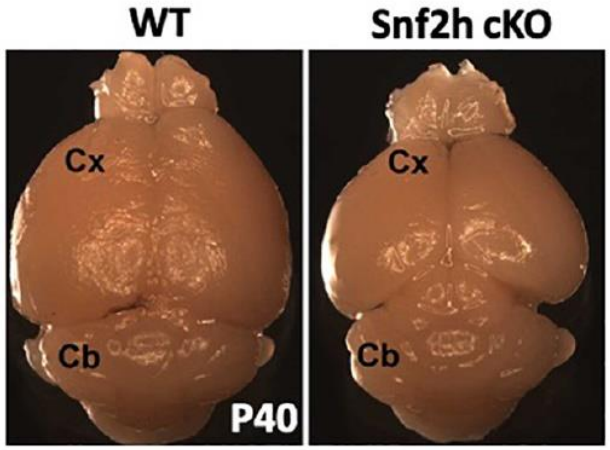

Figure 46 ***Snf2h* Emx1 cKO performed by Alvarez-Saavedra et al. (80).**
P40 brain size comparison of WT and snf2h Emx1 cKO. This resembles (Figure 12), noting that Bptf's conditional removal is considerably more severe, leading to a more hypoplastic neocortex.

Table 7 **Entire list of primers used.**
Genotyping, In-situ Hybridization, RT-PCR and RT-qPCR primers used in the thesis, in the 5' – 3' orientation for each given gene.

Genotyping

Gene name	5' - 3' sequence
Bptf flox - F	GGCACTTGCATGATCTGTTGTCACCCG
Bptf flox - R	TTCTACATGGCCAGCCATGTCCAGGCC
Pax6 Cre - F	ATGCTTCTGTCCGTTTGCCG
Pax6 Cre - R	CCTGTTTTGCACGTTCACCG
SRY-sexing - F	TTGTCTAGAGAGCATGGAGGGCCATGTCAA
SRY-sexing - R	CCACTCCTCTGTGACACTTTAGCCCTCCGA
FABP2(con)-sexing - F	TGGACAGGACTGGACCTCTGCTTTCCTAGA
FABP2(con)-sexing - R	TAGAGCTTTGCCACATCACAGGTCATTCAG

In-situ Hybridization

Gene name	5' - 3' sequence
BPTF-Insitu-F1	AGGAATTCTCCCACCCCTTGAATTTCCG
BPTF-Insitu-R1	AGGGATCCTCAGCGACACAGTCAGTCAC

RT-PCR

Gene name	5' - 3' sequence
Bptf E1 - F	AGCAGCTTCAGGAGCCATAG
Bptf E3 - R	GCTAACTGGACCTTTGTGCTG
β-actin - F	ATGTGGATCAGCAAGCAGGA
β-actin - R	GTGTAAAACGCAGCTCAGTAACA

RT-qPCR

Gene name	5' - 3' sequence
Arx - F	CCGGAGTGCAAGAGTAAATC
Arx - R	TGCATGGCTTTTTCCTGGTC
Ctip2 - F	GACAAGAGCAGTCCACCTCC
Ctip2 - R	GGGAAACAGGGTGGGAGAAC
Emx1 - F	GAAGAATCACTACGTGGTGGG
Emx1 - R	CCGTTTGTATTTTGTCCTCCG
Fezf2 - F	GTCACCGGCCACTTCTAAAAC
Fezf2 - R	GTCTGCCTCTAACGCAGCA
Foxg1 - F	GCTGGACATGGGAGATAGGA
Foxg1 - R	GGTGGTGATGATGATGGTGA
Iba1 - F	TCAACAAGCAATTCCTCGATG
Iba1 - R	CAGCATTCGCTTCAAGGAC
m18S - F	AGTCCCTGCCCTTTGTACAC
m18S - R	GATCCGAGGGCCTCACTAAAC
Mitf - F	AATGGCAAATACGTTACCCG
Mitf - R	CCCTTTTTATGTTGGGAAGG
NeuroD6 - F	AACACTACCGTTTGACGAG
NeuroD6 - R	TGTTTTGGAAAGCTCTCTGG
Neurog2 - F	AACTCCACGTCCCCATACAG
Neurog2 - R	GAGGCGCATAACGATGCTTCT
Nr4a2 - F	CCTGTCAGCACTACGGTGTTC
Nr4a2 - R	TAAACTGTCCGTGCGAACC
Sall1 - F	CTCAACATTTCCAATCCGAC
Sall1 - R	GGCATCCTTGCTCTTAGTGG
Satb2 - F	TGTGACAGACGCCCCTGAT
Satb2 - R	CTCCGCAGGCAAGTCTTCC
Snf2h - F	GACACCGAGATGGAGGAAGTA
Snf2h - R	CGAACAGCTCTGTCTGCTTTA
Snf2l - F	TGCTACAAATGATCCGTCATGG
Snf2l - R	GCGTTCTCGTTTAGGAGGTTCA
Sox2 - F	CGGAGTGGAAACTTTTGTCC
Sox2 - R	CGGGAAGCGTGTACTTATCC
Tbr1 - F	GCAGCAGCTACCCACATTC
Tbr1 - R	GTCCTTGGAGTCAGGAAAATTGT
Tbr2 - F	GCGCATGTTTCCTTTCTTGAG
Tbr2 - R	GGTCGGCCAGAACCACTTC

Table 8 **Entire list of primary antibodies used.**
Immunofluorescence (IF) and western blot (WB) primary antibodies used, with the origin (either company or donated), catalog number and dilution used.

IF - Antibodies

Target	Host	Dilution	Company/Origin	Catalog #
Pax6	Rabbit	1:500	BioLegend	PRB-278P-100
Tbr2	Rabbit	1:300	Abcam	Ab23345
pH3	Rabbit	1:300	Millipore	06-570
Ki67	Mouse	1:100	Bd Pharmigen	550609
Satb2	Mouse	1:100	Abcam	ab51502
Foxp1	Rabbit	1:200	Abcam	Ab216645
Ctip2	Rat	1:500	Abcam	Ab18465
Tbr1	Rabbit	1:100	Abcam	Ab3194
CC3	Rabbit	1:300	Cell Signaling	9579S
Iba1	Goat	1:400	Novus	NB100-1028
Foxg1	Rabbit	1:300	Abcam	Ab18259
Neurog2	Rabbit	1:300	Cell Signaling	13144S

WB - Antibodies

mBPTF	Mouse	1:10000	Wysocka J. et al 2006	-
hBPTF	chicken	1:1000	Xingguo Li et al. 2011	-
Bptf	Rabbit	1:1000	Thermo Fisher	ABE24
Bptf	Rabbit	1:500	Cedarlane	A300-973A-M
Bptf	Rabbit	1:500	Cedarlane	bs-11641R

Table 9 **List of major upregulated genes.**
Transcripts with both Ensembl and common gene names, organized from largest log_2 fold change to smallest, displaying L2FC standard error, significance s-value and base mean expression. Displaying a total of 48 DEGs out of 308 upregulated. Number (first column) describes the list location of each DEG within the 308 total.

Upregulated DEGs

	Ensembl name	Common name	baseMean	Log2 FoldChange	lfcSE	svalue
1	ENSMUSG00000113061	Gm11361	650.4526023	8.218547	2.106966	8.46E-06
2	ENSMUSG00000069117	Gm10260	1276.672252	7.523841	1.406251	2.09E-08
3	ENSMUSG00000113263	Gm4811	31.6732209	4.792824	0.773383	6.95E-10
4	ENSMUSG00000019301	Hsd17b1	38.5031582	4.700429	0.50576	1.57E-18
5	ENSMUSG00000113600	Gm7868	6.53316949	4.633423	1.627403	0.00064091
6	ENSMUSG00000057657	Rps18-ps3	54.93699461	4.546508	1.566749	0.000515922
7	ENSMUSG00000032715	Trib3	231.6113978	3.807155	0.17782	5.02E-79
8	ENSMUSG00000029816	Gpnmb	569.4133926	3.584032	0.209251	4.94E-51
9	ENSMUSG00000038539	Atf5	8904.266835	3.331452	0.08921	7.43E-223
10	ENSMUSG00000031026	Trim66	1561.727205	3.331052	0.117924	3.76E-129
11	ENSMUSG00000078503	Zfp990	16.2388196	3.047291	0.666984	5.31E-06
12	ENSMUSG00000004707	Ly9	33.60730182	2.966308	0.421163	1.55E-10
13	ENSMUSG00000030789	Itgax	105.0739324	2.888416	0.233519	2.23E-26
14	ENSMUSG00000079491	H2-T10	168.0720722	2.880923	0.971711	0.000844541
15	ENSMUSG00000027071	P2rx3	132.1844616	2.875961	0.237675	2.55E-25
16	ENSMUSG00000079293	Clec7a	75.14096503	2.816565	0.28206	3.04E-18
17	ENSMUSG00000018927	Ccl6	133.0222644	2.752706	0.237875	5.12E-23
18	ENSMUSG00000031297	Slc7a3	1865.258226	2.747504	0.268192	8.77E-19
19	ENSMUSG00000069607	Cd300ld3	6.187108262	2.701189	0.936945	0.001072736
20	ENSMUSG00000089929	Bcl2a1b	55.45675433	2.690969	0.287324	6.83E-16
21	ENSMUSG00000050526	4933406M09Rik	9.892372506	2.680555	0.719212	0.000116514
22	ENSMUSG00000035273	Hpse	121.3755684	2.537612	0.192355	3.52E-28
23	ENSMUSG00000014609	Chrne	35.08275392	2.535852	0.338646	4.78E-11
24	ENSMUSG00000079049	Serpinb1c	9.656669001	2.46941	0.791875	0.00072545
25	ENSMUSG00000027313	Chac1	317.2079453	2.382101	0.159449	4.61E-34
27	ENSMUSG00000059089	Fcgr4	23.19828248	2.311606	0.515064	1.44E-05
28	ENSMUSG00000040564	Apoc1	47.34734869	2.310608	0.308716	1.41E-10

29	ENSMUSG00000068129	Cst7	10.2519665	2.297895	0.633909	0.000215436
30	ENSMUSG00000069516	Lyz2	601.6235186	2.263026	0.131149	4.46E-43
31	ENSMUSG00000028893	Sesn2	1544.869276	2.257425	0.08497	7.74E-97
55	ENSMUSG00000024397	Aif1	166.4258849	1.754343	0.246378	1.20E-08
67	ENSMUSG00000020053	Igf1	1050.03608	1.618886	0.072268	6.32E-56
115	ENSMUSG00000052912	Smarca5-ps	60.35713415	1.333818	0.27217	0.000106283
176	ENSMUSG00000043289	Mei4	94.37853449	1.043664	0.202146	0.000369154
224	ENSMUSG00000035158	Mitf	191.9616254	0.890162	0.149611	0.000462851
235	ENSMUSG00000039103	Nexn	1167.129986	0.838901	0.169271	0.002937581
251	ENSMUSG00000047407	Tgif1	456.1402652	0.796242	0.140336	0.002023187
252	ENSMUSG00000020932	Gfap	2208.580275	0.796056	0.137561	0.001737637
262	ENSMUSG00000027967	Neurog2	478.5629274	0.777087	0.088379	7.14E-05
263	ENSMUSG00000032446	Eomes/Tbr2	1521.488172	0.775868	0.072135	5.12E-06
268	ENSMUSG00000017146	Brca1	410.4582312	0.766394	0.125084	0.001891172
276	ENSMUSG00000055612	Cdca7	1433.002384	0.726881	0.073045	8.82E-05
286	ENSMUSG00000031665	Sall1	1620.342063	0.713321	0.093059	0.001178394
295	ENSMUSG00000035277	Arx	7638.464446	0.685366	0.047445	3.47E-06
298	ENSMUSG00000074637	Sox2	5751.683579	0.67009	0.06994	0.000870014
303	ENSMUSG00000041235	Chd7	3504.739456	0.654646	0.0737	0.002131808
304	ENSMUSG00000037851	Iars	6074.594531	0.653546	0.08009	0.003600978
307	ENSMUSG00000096014	Sox1	4756.783544	0.63489	0.060809	0.001418236

Table 10 **List of major downregulated genes.**
Transcripts with both Ensembl and common gene names, organized from largest log_2 fold change to smallest, displaying L2FC standard error, significance s-value and base mean expression. Displaying a total of 48 DEGs out of 349 downregulates. Number (first column) describes the list location of each DEG within the 349 total.

Downregulated DEGs

	Ensembl name	Common name	baseMean	Log2 FoldChange	lfcSE	svalue
1	ENSMUSG00000059898	Dsc3	253.7375668	-3.042021867	0.200704	0
2	ENSMUSG00000059899	Ccl2	17.65510304	-2.781350608	0.959688	0.000980299
3	ENSMUSG00000059900	Pla2g4d	13.90472577	-2.633237474	0.579996	7.77E-06
4	ENSMUSG00000025469	Msx3	102.2491031	-2.628992815	0.276412	2.25E-16
5	ENSMUSG00000026065	Slc9a4	15.62773671	-2.573483572	0.668543	9.25E-05
6	ENSMUSG00000020905	Usp43	1594.530981	-2.319852608	0.094217	0
7	ENSMUSG00000032128	Robo3	184.7541298	-2.270929754	0.241528	4.79E-15
8	ENSMUSG00000039714	Cplx3	65.94303819	-2.253394306	0.285956	3.25E-11
9	ENSMUSG00000051456	Hspb3	118.0982339	-2.148023974	0.19246	0
10	ENSMUSG00000090061	Nwd2	2930.416956	-2.110240998	0.105059	0
11	ENSMUSG00000115928	Gm18930	7.797295864	-2.103074614	0.74733	0.001762923
12	ENSMUSG00000020067	Mypn	72.41973239	-1.980238334	0.259051	3.53E-10
13	ENSMUSG00000020123	Avpr1a	91.77150061	-1.888901896	0.293647	9.05E-08
14	ENSMUSG00000030905	Crym	2389.721948	-1.843498051	0.211229	5.90E-12
15	ENSMUSG00000059456	Ptk2b	2458.862492	-1.755259394	0.057508	0
16	ENSMUSG00000019890	Nts	1852.659191	-1.751873672	0.242994	6.52E-09
17	ENSMUSG00000046321	Hs3st2	1135.53216	-1.671640581	0.099989	0
18	ENSMUSG00000034209	Rasl10a	82.51405701	-1.625231975	0.198382	4.28E-10
19	ENSMUSG00000023159	Psg29	26.4368702	-1.59827616	0.397761	0.000280299
20	ENSMUSG00000049107	Ntf3	188.5479162	-1.581059453	0.155817	8.58E-14
21	ENSMUSG00000041828	Abca8a	503.7766837	-1.548557154	0.104821	0
22	ENSMUSG00000070570	Slc17a7	4312.707957	-1.526131433	0.07677	0
23	ENSMUSG00000024517	Grp	577.6971532	-1.524540714	0.115621	0
24	ENSMUSG00000037737	Actrt3	17.0463064	-1.49759639	0.536637	0.004645072
25	ENSMUSG00000046318	Ccbe1	2165.219494	-1.493322216	0.106984	0
76	ENSMUSG00000033060	Lmo7	5046.832568	-1.142807264	0.067304	0
77	ENSMUSG00000021765	Fst	594.8048991	-1.141586604	0.118649	1.55E-09
96	ENSMUSG00000039982	Dtx4	8139.791166	-1.054654753	0.064245	0.00E+00

99	ENSMUSG00000028341	Nr4a3	3418.787373	-1.046210247	0.086189	6.76E-12
105	ENSMUSG00000053310	Nrgn	8973.524641	-1.030440762	0.119809	3.97E-07
112	ENSMUSG00000026826	Nr4a2	4494.147178	-1.010347002	0.099794	9.49E-09
113	ENSMUSG00000009376	Met	1664.310249	-1.008898566	0.107562	8.59E-08
114	ENSMUSG00000041959	S100a10	1194.53332	-1.007468792	0.120784	1.06E-06
115	ENSMUSG00000022382	Wnt7b	8300.895473	-1.006588379	0.060657	0
116	ENSMUSG00000033726	Emx1	1651.324192	-1.006179086	0.06904	5.93E-15
117	ENSMUSG00000037984	Neurod6	18330.97323	-1.001256527	0.085604	1.69E-10
129	ENSMUSG00000022372	Sla	10055.75305	-0.963061136	0.056585	4.52E-18
132	ENSMUSG00000040536	Necab1	4103.236205	-0.959444451	0.07361	1.30427E-11
138	ENSMUSG00000005583	Mef2c	40788.73818	-0.948223556	0.080112	5.45E-10
149	ENSMUSG00000021743	Fezf2	3216.886654	-0.925131668	0.062277	2.01E-13
153	ENSMUSG00000038331	Satb2	13504.74107	-0.911155112	0.100236	1.60E-06
163	ENSMUSG00000006457	Actn3	151.9033566	-0.892038951	0.186491	2.10E-03
215	ENSMUSG00000058070	Eml1	5524.646035	-0.792819695	0.088037	3.85072E-05
234	ENSMUSG00000022054	Nefm	5527.608124	-0.764148858	0.090146	1.51E-04
237	ENSMUSG00000041540	Sox5	6223.190773	-0.758968414	0.092496	0.000241171
260	ENSMUSG00000022346	Myc	2276.978834	-0.730831962	0.069903	4.32E-05
287	ENSMUSG00000022055	Nefl	4929.703708	-0.707244775	0.080116	5.07E-04
308	ENSMUSG00000051359	Ncald	10012.53972	-0.673261934	0.069869	0.000748475

CV

Gerardo Zapata

Education

Master of Science | 2018 - 2020 | University of Ottawa

- Masters in Biochemistry with a specialization in Bioinformatics
    - Performed thesis under Dr. David Picketts' supervision in the Ottawa Hospital Research Institute. My thesis focused on characterizing the role of a chromatin remodelling protein, called BPTF, during murine brain development. Mainly, understanding pathways controlled by chromatin remodelers during brain development to understand human disease for advancing future treatment.
    - Simultaneously, completed a bioinformatics specialization. Taking courses focusing on Omics-data analysis, bioinformatics and gene expression to successfully carry out NGS based research

Bachelor of Science | 2012 - 2017 | Dalhousie University

- Major in Marine Biology + Certification in Genetics + Minor in Biochemistry & Molecular Biology
    - Performed an independent research project under the supervision of Dr Herbinger. Using genotypic microsatellites, I created a family pedigree of a guppy population, to further understand the evolutionary and reproductive forces shaping guppy populations in Trinidad.

Work Experience

Bioinformatics Consultant | Dr. Picketts' Lab | Ottawa Hospital Research Institute | October 2020 – Currently

· Currently performing Next Generation Sequencing data analysis to further substantiate research articles for the Picketts' lab. I am completing RNA-seq, ChIP-seq and ATAC-seq analysis using Linux bash commands as well as, R-based analysis.

Summer student | Dr. Picketts' Lab | Ottawa Hospital Research Institute | April – Sept. 2018

· I performed routine laboratory experiments and maintained several mouse lines. I learned to execute multiple protein, genomic and, RNA based experiments in preparation for graduate studies. Using a mouse model and basic cell culture techniques.

Tiger Patrol Representative | Dalhousie University | Sept. 2016 – April 2017

· Tiger Patrol served as a university's "arrive home safe" program. My team and I oversaw the transportation of students to and from university's campuses in a respectful and reliable environment.

Skills & Abilities

Communication

· Bilingual – Fluent in Spanish and English
· Positive interpersonal skills developed as an Official Canvasser for the Canadian Red Cross.

Volunteer | Discovery Centre | Halifax, NS | Nov. – Dec. 2017

· Assisted the STEAM facilitators, by welcoming all visitors to the science centre. My role entailed explaining the scientific exhibits to all the children and their guardians as well as to encourage them to participate and learn from the exercises provided by the Discover Centre.

Volunteer | Arxelon | Geek NGO | May – August 2015

· Arxelon presented me with the opportunity to participate in a rare program in which, our team was responsible for physically capturing, tagging, taking skin samples for genomic research and, returning the turtles safely to the bay. Allowing for the exact catalog and development of the *Caretta caretta* migration patterns.

Certifications

· Canadian Council of Animal Care certified | September 2015 – September 2016
· Open water diver certification by FMAS